The optics and applications of graphene oxide

A thesis submitted for the degree of
Doctor of Philosophy

by

Xiaorui Zheng

Centre for Micro-Photonics
Faculty of Science, Engineering and Technology
Swinburne University of Technology
Melbourne, Australia

Principle supervisor: Associate Professor Baohua Jia
Coordinating supervisor: Professor Min Gu
2016

Abstract

Civilisations, or our technologies in general, are advanced by both incremental developments, such as optimisation and miniaturisation, and quantum leaps such as the Industrial Revolution. Undoubtedly, the semiconductor industry has revolutionised almost all aspects of our technologies and daily life during the past century. Silicon, as the principal material for semiconductor devices, has not only dominated the research in material science, but also shaped the engineering counterparts in terms of manufacturing and processing. Recently, photonics have attracted considerable attentions due to the ultrawide bandwidth, fast operation speed and less power consuming over the silicon-based electronics, showing promising potentials towards the next quantum leap. However, the use of silicon in photonics has been greatly restricted, resulting from its large footprint, opaqueness in the visible range, and complex and time-consuming manufacturing. As a result, new materials specifically designed for photonics are highly demanded but yet to be demonstrated.

Carbon, the basis of all organic chemistry, shows an unlimited number of chemical structures due to the flexibility of its bonding. Graphene, a monolayer of sp^2-bonded carbon atoms tightly packed into a honeycomb lattice, has attracted unprecedented enthusiasm during the past decade due to its exceptional mechanical, thermal, optical, and electrical properties, making it a promising candidate for a wide range of applications, including field-effect transistors, field emitters, biosensors, optical polarisers, and transparent conducting electrodes. Despite its extraordinary properties and huge potential

applications, it remains challenging of its mass production with large lateral size and cost-effective manufacturing for industrial applications.

Alternatively, chemically derived graphene oxide, traditionally served as the precursor for graphene, becomes an attractive material itself due to a unique set of characteristics arising from the oxygen functional groups that are introduced during the chemical exfoliation of graphite. From the chemical structure point of view, graphene oxide can be seen as the graphene sheet covalently decorated with various oxygen functional groups either on the basal plane or at the edge. As a result, the hybridisation of sp^2 and sp^3 carbon atoms happens in graphene oxide, which is the origin of its unique physical and chemical properties. Moreover, the optoelectronic properties of graphene oxide can be tailored by manipulating the size, shape and relative fraction of the sp^2-hybridised domains of graphene oxide during its reduction process. It has been reported that the insulating as-synthesised graphene oxide becomes both optically transparent and electrically conducting after the controlled deoxidation treatment, enabling numerous electronic and optoelectronic applications including transparent conductors, field-effect transistors, thin film transistors, field emitters, photovoltaic devices, light-emitting devices, flexible electronic materials and electrical sensors.

Compared with the extensively investigated electronic and optoelectronic properties of graphene oxide, the optical properties of graphene oxide are less explored. For example, the current optical studies of graphene oxide are largely limited within the phenomenal observations and demonstrations, such as fluorescence and fluorescence quenching, optical spectrum measurements, and Raman spectrum characterisations. Few optical functional devices or components have been realised on graphene oxide, in particular adapting its tunable optical properties, simultaneously patterning capability during reduction, and the mechanical robustness for flexible or bendable devices. The main challenge is the limited understanding of the fundamental optical properties as well as the physical mechanisms of both graphene oxide and reduced graphene oxide due to their chemical structural complexities. Their optical activities are highly sensitive to the presence of the oxygen functional groups including the type, the fraction, and their distributions on the basal plane.

The main objective of this thesis is to thoroughly investigate the fundamental optical properties as well as the underlying physical mechanisms of both graphene oxide and reduced graphene oxide. Based on the characterisations and understanding of their optical activities, various optical functional components have been designed and realised both experimentally and theoretically. The major achievements can be summarised as follows:

1. Few results have been reported on the linear dispersion relations of reduced graphene oxide, in particularly through the laser-induced reduction process. Compared with the largely applied thermal or chemical reduction, laser-induced reduction has the advantages of flexible manufacturing and localised property modifications. Moreover, the linear dispersion relations of laser-induced reduction of graphene oxide is believed to be different with that of thermal or chemical reduction of graphene oxide due to the varied reduction mechanisms. It is of both fundamental and practical interest to investigate the linear dispersion relations of laser-induced reduction of graphene oxide at various reduction extents. As a result, in this thesis the linear dispersion relations of graphene oxide and reduced graphene oxide thin films at various reduction extents have been investigated by using the focused beam spectroscope ellipsometry technique from the ultraviolet (200 nm) to the near-infrared (1.7 μm) range. The Kramers-Kronig consistent has been maintained by fitting ellipsometry data using the B-Spline followed by Gen-Osc models. The linear dispersion relations can be tuned depending on the reduction parameters (laser powers in our case), and the changing of both refractive index and extinction coefficient are attributed to the removal of interlamellar water and the oxygen functional groups, respectively.

2. The linear dispersion relations of graphene oxide or reduced graphene oxide in the infrared range are still missing, which are critical for not only the understanding of their dispersion theory, but also the potential infrared applications including infrared photodetectors, infrared light emitters, biomedical

imaging and sensing, and plasmonics. As a result, in this thesis the Kramers-Kronig relations have been used to determine the linear dispersion relations of graphene oxide and reduced graphene oxide films over the broadband range from the ultraviolet (200 nm) to the mid-infrared range (up to 20 μm). The missing information especially in the infrared range has been obtained, which is inaccessible to the traditional spectroscope ellipsometry method. Moreover, the bandgap tuning of graphene oxide after the laser reduction has been revealed by fitting its conductivity with the Lorentz model.

3. The third-order nonlinearity, in particular the nonlinear refraction (Kerr effect), is crucial for high performance integrated photonic applications including all-optical switching, signal regeneration and fast optical communications. However, the research on nonlinearities of graphene oxide are largely limited to the nonlinear absorption such as optical limiting or saturable absorption, whereas the Kerr nonlinearity has only been conducted in graphene oxide solutions or composites, which are challenging to be used for solid state integrated photonic devices. Moreover, tunable nonlinearities of graphene oxide remain unexplored, which are expected due to the gradual removal of the oxygen functional groups during its reduction process. As a result, in this thesis rich and giant nonlinear activities of the graphene oxide thin film during its entire laser-induced reduction process are unveiled by using the Z-scan measurement. The nonlinear absorption is observed to transit from saturable absorption to optical limiting, whereas the nonlinear refraction is found to transit from self-focusing to self-defocusing. Four distinguished stages with unique nonlinear activities have been demonstrated within the entire laser reduction process of the graphene oxide thin film.

4. For nonlinear functional devices, the required interaction length of light with high nonlinearity media, for instance graphene oxide, can be significantly reduced. However, the presence of considerable linear loss has largely degraded the signal to noise ratio due to the insufficient signal transmission through the devices. As a result, in this thesis the enhanced nonlinearities of the hybrid graphene oxide with gold nanoparticle films have been demonstrated. The effective functionalisation of graphene oxide with gold nanoparticles has been

realised by the filtration process and revealed by both the ultraviolet-visible and fourier transform infrared spectra. The enhanced nonlinear light-matter interactions of the hybrid films can be attributed to the efficient energy and/or charge (electron) transfer upon photoexcitation, and the synergistic coupling effects between gold nanoparticles and graphene oxide.

5. Although numerous ultrathin flat lenses have been demonstrated including Fresnel lens, plasmonic lens, metalens, and super oscillation lens, it remains challenging to achieve micro optical lenses with three-dimensional subwavelength focusing resolution, high focusing efficiency, broadband operation, ultrathin thickness, low-cost manufacturing and flexible integration capability. As a result, in this thesis a graphene oxide ultrathin flat lens has been demonstrated. Based on the unique and giant refractive index and absorption modulations of the graphene oxide thin film during its laser-induced reduction process, the performance of the graphene oxide lens has been optimised both theoretically and experimentally. The far-field three-dimensional subwavelength focusing ($\lambda^3/5$) with an absolute focusing efficiency >32% for a broad wavelength range from 400 nm to 1500 nm has been achieved. In addition, the mechanical robustness of our graphene oxide lens and the wavefront shaping capability of the graphene oxide thin film have also been presented.

6. The polarisation control of light is one of the key issues in the modern miniaturised photonic systems. Although various ultrathin polarisers have been extensively studied both theoretically and experimentally including metamaterials, metasurfaces, wire-grid polarisers and guided resonance-based polarisers, it is still challenging to realise ultrathin polarisers in the infrared range with high extinction ratio, high transmission efficiency, flexible and integratable capabilities and cost-effective manufacturing methods. In this thesis, an ultrathin graphene oxide micro-polariser has been proposed theoretically based on the out of plane guided resonances of two-dimensional photonic crystals. The extinction ratio as high as 3600 can be achieved by largely breaking the rotational symmetry of the structures. Moreover, the working wavelength can be tuned over a broadband range from visible to near-infrared

due to the dispersionless nature of graphene oxide. Finally, the tolerance of the incident angle has been investigated and the excellent polariser performance can be maintained for a wide range of incident angle as large as 30°.

In summary, this thesis presents innovative research on the optics and applications of graphene oxide and reduced graphene oxide by using the direct laser printing method. Unique properties of graphene oxide have been demonstrated experimentally including the tunable dispersion relations, patterning capability, surface functionalisation possibility, wavefront shaping ability, and the mechanical robustness and stress, which are indispensable for the next generation highly efficient, integratable, ultralight weight, and flexible optical systems towards various multidisciplinary applications.

Acknowledgment

I came to Australia for the Ph.D in June 2012 and have spent three and a half years in Swinburne University of Technology. And luckily I am able to survive and move towards the completion of my Ph.D now. I have never been alone or lonely during the three and a half years' journey. Surely I wouldn't get to this point without the help from all the following kind persons in my life.

First of all, I would like to give my special thanks to my principle supervisor, Associate Professor Baohua Jia (who was actually promoted after my arrival). I was having a hard time when I was doing my Master's degree. And she offered me a great opportunity as a Ph.D candidate in Australia (although I got another offer in United States), which has now been proved as an unbelievable decision all through my life (and her life as well). Within such a short Ph.D period (long enough for me), we had a wonderful time and achieved fruitful outcomes. Baohua is always supportive to all her students. We had 546 individual discussions, which means talking for more than one month without stopping, not saying the numerous group meetings (twice a week). Moreover, she gave me a few lists of tasks and always trusts me in all the research projects (although only 10% has been completed so far), which forces me to be more confident (and independent). Also she always respects all the decisions I made and offers all she could to help me towards my goals. To many to be listed here, but my life has been totally changed because of her.

I would like to give my profound gratitude to my coordinating supervisor Professor Min Gu. Professor Gu built an empire in the field of Nanophotonics, the Centre for Micro-Photonics (CMP), offering invaluable opportunities and

outstanding resources for young students and researchers all over the world to realise their dreams. As a leading scientist, Min's time is never sufficient for his scientific commitments. However, students are always his first priorities. Every week he spends two entire days meeting his students. Through the enjoyable Ph.D research experience in CMP, he brought me into much broader research fields not only on photonics but also on plasmonics, physics and nanotechnology. More importantly, I learnt the invaluable lessons from him on the way of critical thinking, the deep insights into the essence of the problems, and always having confidence on myself. As the distinguished professor, he is an easygoing person and always willing to help his students in every aspects. My wife and me are very grateful to Min for his support in Australia and his suggestions to our family. Whatever I do and wherever I am in future, these will certainly benefit me a lot.

I would like to thank Dr. Qiming Zhang who has not only provided me a great accommodation, but also helped me to build up my first laser characterisation system. Thank Dr. Mark Turner and Dr. Muntasir Hossain for their help at the beginning of my Ph.D. Thank Dr. Benjamin Cumming for his help in direct laser writing using his Ultrabright system. Thank Dr. Ye Chen for helping me the N-STORM super-resolution system. Thank Dr. Han Lin for his indispensable contributions to my Ph.D project. Many thanks to my friends Dr. Yinan Zhang, Dr. Boyuan Cai and Dr. Shouyi Xie at Swinburne who got the degrees before me. We had a wonderful time together. Also I would like to thank Mr. Fabio Turella, Ms. Sahar Tabrizi, Ms. Martina Barbiero, Ms. Elena Goi, Mr. Haoran Ren, Mr. Haitao Luan, Ms. Shuo Li, Mr. Xuewen Wang, Mr. Yunyi Yang, Mr. Scott Fraser, Mr. Gaolei Xue, Mr. Jingyang Peng, Ms. Jun Ren and Mr. Tieshan Yang, who are still on the journey. Good luck all and take care!

I would like to thank our collaborators Professor Dan Li and Dr. Ling Qiu from Monash University, and Professor Minghui Hong and Mr. Lianwei Chen from National University of Singapore, who continually provide me the high quality samples. Many thanks go to Dr. Bing Xu from Institute of Physics, Chinese Academy of Sciences for his help in FTIR characterisations.

I should not forget the CMP lab manager Dr. Dru Morrish. He is always the first person I thought of when anything in the lab went wrong or I would like to try some unusual experiments. I would like to thank Dr. Xiaohan Yang, who is always giving me helpful suggestions. My thanks also go to Mr. Mark Kivinen. Without his help, I would have not obtained the desired experiment results. I would like to give my deep thanks to Ms. Pierrette Michaux and Dr. Xijun Li for their professional technical support in the nanofabrication lab. Thanks to the administrative staffs Ms. Barbara Gillespie, Ms. Jia Lou and Ms. Johanna Lamborn for kindly assisting me with all the paperwork. I would like to thank everyone in the CMP for sharing your knowledge and always being there to offer help. Many thanks to my dear friends, too many to name them all. They made my life so colourful.

I would like to thank my parents for their support during my endless schooling time.

Finally, the most special thanks go to my wife, who has been supporting me all through my Ph.D, including cooking 3,832 meals, working for 6,370 hours, 182 house cleaning, 364 clothes washing and few arguments. Her love and care gave me endless strength, without which I would not have had all the achievements.

Xiaorui Zheng

Melbourne, Australia, 24^{th} December, 2015

Declaration of Authorship

I, Xiaorui ZHENG, declare that this thesis entitled:

"***The optics and applications of graphene oxide***"

is my own work and has not been submitted previously, in whole or in part, in respect of any other academic award.

Xiaorui ZHENG

Centre for Micro-Photonics
Faculty of Science, Engineering and Technology
Swinburne University of Technology
Melbourne, Australia

March 2016

Contents

List of abbreviations

2D	two-dimensional
3D	three-dimensional
AAO	anodic aluminum oxide
AuNP	gold nanoparticle
CCD	charge-coupled device
CVD	chemical vapor deposition
DLW	direct laser writing
DMF	N-Dimethylformamide
EBL	electron-beam lithography
EDX	energy-dispersive X-ray spectroscopic
EM	electromagnetic
ESA	excited state absorption
FIB	focused ion beam
FIR	far-infrared
FL	focal length
FOM	figure of merit
FTIR	fourier transform infrared spectroscopy
FWHM	full width at the half maximum
GO	graphene oxide
IR	infrared
ITO	indium tin oxide
KK	Kramers-Kronig

LC	liquid crystal
MD	modulation depth
MIR	mid-infrared
NA	numerical aperture
NIR	near-infrared
NLR	nonlinear refraction
NS	nonlinear scattering
OL	optical limiting
PC	photonic crystal
PMMA	poly(methyl methacrylate)
rGO	reduced graphene oxide
RIE	reactive-ion etching
RSA	reverse saturable absorption
SA	saturable absorption
SE	spectroscopic ellipsometer
SEM	scanning electron microscope
THz	terahertz
TPA	two-photon absorption
UV	ultraviolet
UV-Vis	ultraviolet-visible
VIS-NIR	visible to near-infrared
XPS	X-ray photoelectron spectroscopy

List of symbols

$\vec{r}$	complex reflection coefficient
r_s	reflection coefficients of s polarization
r_p	reflection coefficients of p polarization
Δ	phase difference between r_s and r_p
$\vec{\varepsilon}$	complex permeability
ε_1	real part of the complex permeability
ε_2	imaginary part of the complex permeability
$\vec{\sigma}$	complex conductivity
σ_1	real part of the complex conductivity
σ_2	imaginary part of the complex conductivity
$\vec{N}_c$	complex refractive index
n	refractive index
κ	extinction coefficient
E_g	optical bandgap
ω	frequency of incident light
ω_0	fundamental frequency of the material
ω_p	plasma frequency
T	linear transimssion
t_f	transmittance of the film
F_{in}	input fluence
F_{out}	output fluence
n_2	nonlinear refractive index

β	nonlinear absorption coefficient
a_m	the radius of the mth rGO zone
f	focal length of the GO flat lens
$\Delta\varphi$	phase modulation between GO and rGO zones
N	total rGO zone number
l	fabrication linewidth
λ	wavelength
E	electric field
α	absorption coefficient
Φ_{film}	phase modulations provided by the film
Φ_{air}	phase modulations provided by the air
t	film thickness
M	Gaussian modulation function
k	wave vector
θ_m	diffraction angle between the wave vector and the optical axis
a	periodicity of the 2D C-shape array
r	radius of the C-shape
ρ	C-shape opening angle
η	extinction ratio of the GO polarizer
γ	C-shape rotation angle
V	polarization degree
θ	colatitude angle

Chapter 1

Introduction

1.1 Background

1.1.1 Graphene oxide and reduced graphene oxide

The discovery of graphitic carbon monolayers by chemists and surface scientists can be tracked back to the 1960s and 1970s[1–3], which has later on been referred as graphene in 1986 by Boehm *et al.*[4]. However, the preparation of individual graphene sheet remained challenging until 2004, when monolayer graphene, an atomically thin layer of sp^2-hybridised carbon atoms arranged in a honeycomb lattice, has been transferred to a silicon dioxide substrate by Geim and Novoselov using the simple Scotch tape method[5,6]. Graphene has quickly become the subject of intense research across virtually all scientific disciplines[7] due to the subsequent discoveries of a range of unusual phenomena arising from its giant carrier mobility[8–10] and the linear dispersion relations[6,11–17], such as the extraordinary mechanical[18], thermal[19], chemical[20], and optical[21] properties in various disciplines beyond condensed matter physics. By exploiting the combination of its unique optical and electronic properties, the rise of graphene in both photonics and optoelectronics has been demonstrated by subsequent discoveries, ranging from light-emitting devices[22] and solar cells[23] to touch screens[24], photodetectors[25,26] and utrafast lasers[27]. Various synthesis strategies of graphene have been reported including the mechanical exfoliation techniques[5], the chemical vapor deposition (CVD)[28–30], the solid state carbon source deposition[31–34], the solution exfoliation[35], and the nanotube splitting and unzipping[36,37]. However, its cost-effective mass production, bandgap tailoring, solubility and processability, and the manufacturing capability for device fabrication are huge obstacles toward graphene-based applications. Alternatively, the chemically derived graphene shows promising potentials to produce and manipulate graphene, which usually involves the chemical synthesis of graphite oxide, followed by its exfoliation into individual graphene oxide sheets, and their subsequent reduction. More importantly, a fascinating field of graphene oxide has emerged recently not only because of its analogous to graphene, but also its low-cost mass production, solubility in a variety of solvents, flexible manufacturing, mechanical robustness and stability, tunable properties, and interaction with a wide range of organic and inorganic materials. As a result, the scope of the thesis is investigating the optical properties and applications of graphene oxide (GO) and reduced graphene oxide (rGO) by using the direct laser writing (DLW) method.

The precise chemical structure of GO has been the subject of a longstanding debate over the years due to the complexity of the material, and no unambiguous model has been demonstrated even to this day. However, it is well recognised that the monolayer GO sheet can be viewed as graphene decorated with the oxygen functional groups on both sides of the basel plane and around the edges[38,40]. Therefore, the electronic structure of GO has been modified due to the presence of the oxygen functional groups compared with that of graphene, and can be chemically, thermally, or electrochemically engineered by manipulating the type, the fraction and the distribution of the oxygen functional groups during its reduction process. As described by Lerf *et al.*[38,40](Figure 1.1a), hydroxyls and epoxies are the main functional groups on the basal plane, whereas the carboxyl groups are primary present at the edges, isolating the ordered small sp^2 clusters within the sp^3 C-O matrix. As a result, the disrupted

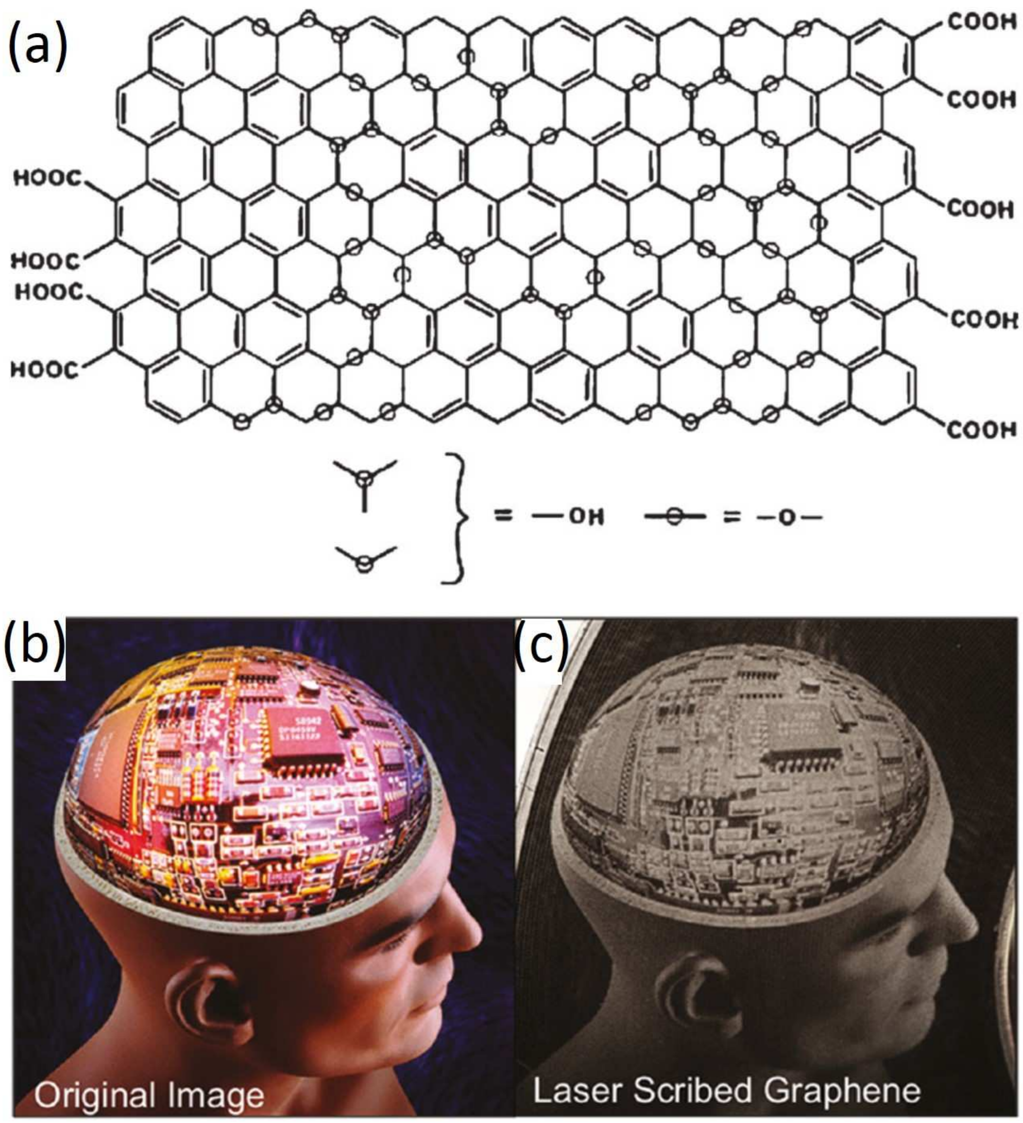

FIGURE 1.1: (a) The chemical structure model of GO[38]. The oxygen functional groups, indicated by circles, are attached on both sides of the graphene sheet. (b) A standard complex colored image of a man's head filled with circuits. (c) The same image reproduced by reducing GO at various levels, which corresponds to a change in electrical properties[39].

sp^2 bonding networks make GO an electrically insulating material, which has significantly restricted its applications, especially for electronics. However, GO can be made into a semiconducting or semimetallic material by the restoration of the sp^2 conjugated graphene network using various reduction strategies including chemical, thermal, electrochemical and photo reduction methods. The effectiveness and efficiency of the reduction process are largely dependent on the reduction methods as well as the used parameters. For thermal reduction, vacancies or defects can be created on the basal plane due to the evolution of carbon in the form of carbon monoxide or carbon dioxide[41]. Also chemical reduction using hydrazine monohydrate is an attractive option for reducing aqueous dispersion of GO due to the less side reactions with solvents. However, heteroatomic impurities can be introduced in the chemical reduction process using hydrazine in particular. Electrochemical reduction offers another promising reduction method by applying sweep voltage, and the conductivity as large as 8500 $S \cdot m^{-1}$ has been achieved[42]. Recently, the photoreduction of GO has been extensively developed including photothermal, photochemical and laser reduction. More importantly, the photoreduction permits flexible patterning, controllable tuning of the film conductivity, residual oxygen contents, porosity, and surface wettability, which results in various functionalities unaccessible for traditional reduction methods (Figure 1.1b,c).

1.1.2 Optical and electrical properties

From the structure-property point of view, the properties of GO and rGO thin films are heavily dependent on their chemical or atomic structures. By appropriately varying the film thickness, chemical composition, average flake size, film morphology and reduction parameters, the GO and rGO films can be modified as insulating, semiconducting, or semimetallic materials. However, compared with the effects devoted to understanding the electronic structure of graphene[43], the equivalent information on GO or rGO remains largely unexplored due to the structural disorder. It is demonstrated the tuning of the optical transmittance of GO and rGO can be achieved by varying the film thickness, the concentration of solution or the extent of reduction. The typical optical absorption of GO can be observed between 225 and 275 nm, which is attributed to the π-π^* transitions[44]. Figure 1.2 shows the ultraviolet-visible (UV-Vis) absorption spectra of GO solutions in water as a function of elapsed time during chemical reduction by hydrazine. The intrinsic absorption of GO can be characterised by the π-π^* plasmon peak near 230 nm and a broad absorption shoulder around 300 nm, which is due to n-π^* transitions of ketonic species

(C=O)[45,46]. Upon chemical reduction of GO, the absorption increases with the redshift of the peak to 270 nm, corresponding to the increased π-electron concentration and structural ordering including the restoration of sp^2 carbon and possible rearrangement of atoms[47].

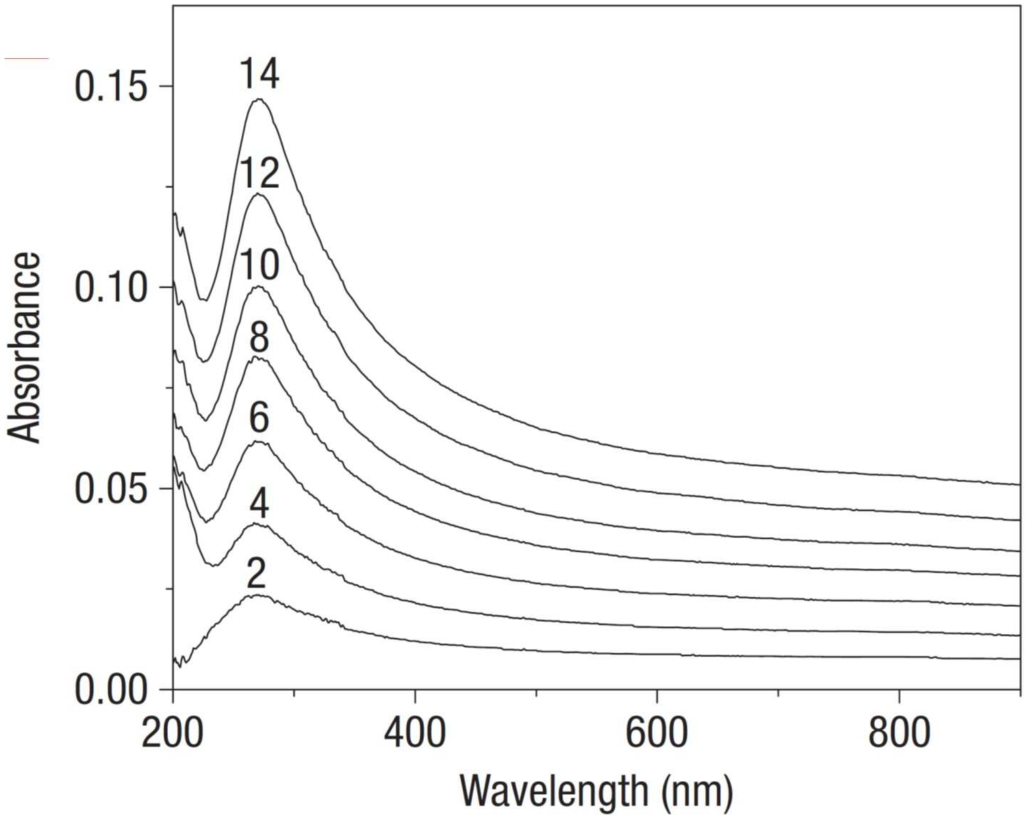

Figure 1.2: The UV-Vis absorption spectra of GO solutions in water as a function of elapsed time, increasing from 2 minutes to 14 minutes with a step of 2 minutes, during the chemical reduction by hydrazine[47].

The sheet resistance of $\sim 10^{12}$ $\Omega\cdot\text{sq}^{-1}$ or higher has been reported for the as-synthesised GO films, which is attributed to the absence of percolating pathways among sp^2 carbon clusters to allow classical carrier transportation[49]. By carefully minimising the oxidation level of rGO, the sheet resistance can be decreased by several orders of magnitude[50,51]. However, the sheet resistance as large as 0.34 M$\Omega\cdot\text{sq}^{-1}$, two orders of magnitude higher than that of ideal dopant-free graphene[7], was demonstrated even in well-reduced GO samples (annealed at 1000°C in hydrogen)[52]. We can gain further insight into the electrical conduction mechanisms of GO and rGO. Carriers traveling across the GO/rGO thin films are usually trapped by the sp^3 carbon domain due to the

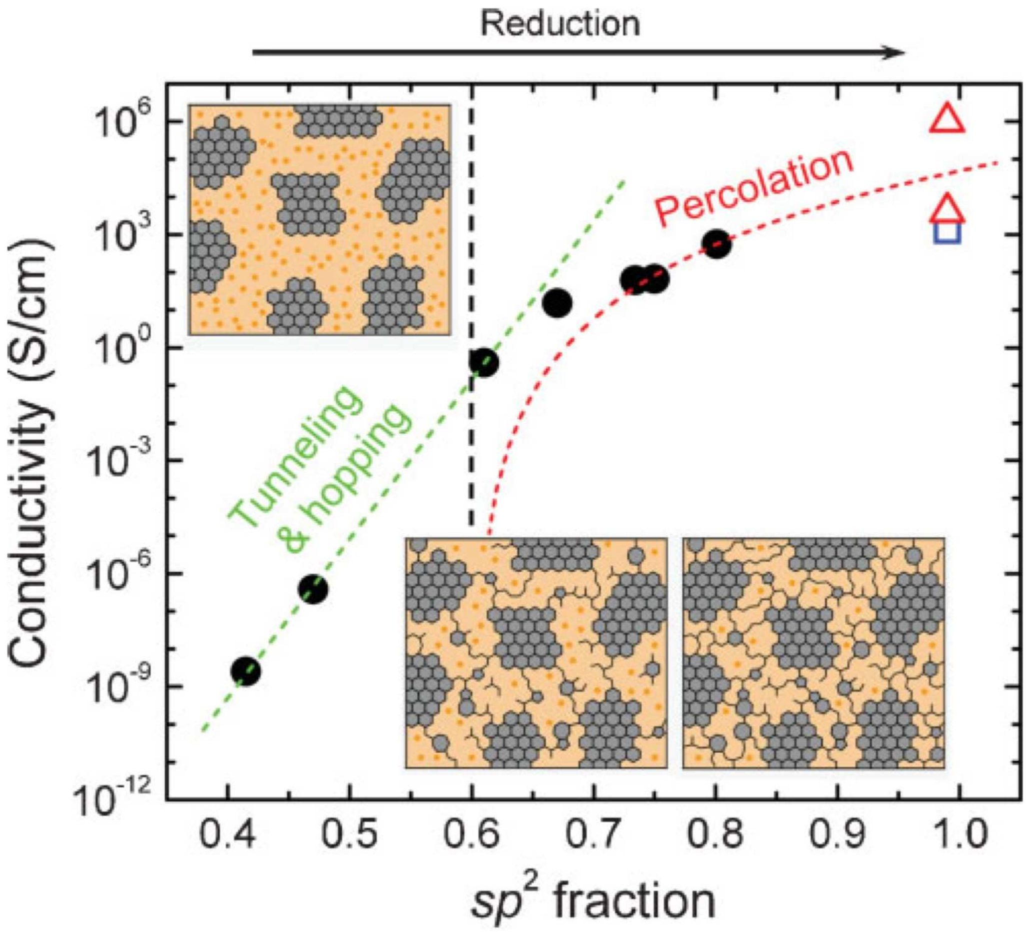

FIGURE 1.3: The conductivity of thermally reduced GO as a function of sp^2 carbon fraction measured by X-ray photoelectron spectroscopy (XPS)[48]. The percolation threshold is found to be 0.6 of sp^2 fraction, indicated by the dashed line. Two different electrical transportation regimes have been revealed, which are the tunneling and/or hopping below 0.6 and the percolation above the percolation threshold. The triangles are the conductivity values for 100% sp^2 carbon materials, polycrystalline graphite and graphene, as a reference. Inset: The structural model of GO at different stages of reduction with the gray regions representing sp^2 carbon clusters and the lighter regions represent an sp^3-carbon-rich phase. The interconnectivity of the sp^2 clusters improves as the reduction of GO (from left to right).

presence of defects, sheet junctions, and structural imperfections and impurities. To elucidate the limited electronic transport of rGO films, the role of residual oxygen and sp^2 carbon fraction on the electrical conductivity has been investigated[48]. And the conductivity of thermally reduced GO as a function of sp^2 carbon fraction has been plotted with the conductivity of 100% sp^2 bonded materials (graphene and polycrystalline grapite) for comparison, as shown in Figure 1.3. The inset shows the proposed structural model of rGO through the different stages of reduction, providing the essential features of the carrier transportation. Firstly, the sp^2 clusters are isolated by oxygen atoms in GO film before reduction, rendering GO insulating. Upon reduction, the sp^2 carbon restores in GO and the barrier between clusters narrows, permitting the tunneling and/or hopping of a small fraction of carriers among sp^2 sites. Moreover, new, smaller sp^2 clusters have been formed at further reduction, resulting in a greater connectivity among the original sp^2 sites. As a result, percolation among the sp^2 clusters can be predicted at higher sp^2 fractions. By exponential fitting the conductivity in Figure 1.3, the percolation threshold of 0.6, which is in reasonable agreement with the theoretical threshold values for conduction among two-dimensional (2D) disks[53], has been demonstrated, differentiating the two regimes for electrical transportation.

1.1.3 Applications

Transparent and conducting electrodes are indispensable components for optoelectronic devices such as solar cells, light-emitting diodes and displays. Given its extraordinary conductivity and atomic thickness, graphene is believed to be a potential candidate for transparent conductor applications as a replacement for indium tin oxide (ITO), and offers several advantages over traditional metal oxide films particularly in the flexible, stretchable, foldable electronics due to its mechanical robustness[7]. Compared to graphene or ITO, GO and rGO have the advantages in cost and processability as the transparent and conducting electrodes. By optimising the film thickness and reduction extent, rGO thin films can be made transparent and conducting. A range of transmittance and sheet resistance values have been reported by employing various oxidation, exfoliation, dispersion, deposition, and reduction procedures, as shown in Figure 1.4. It can be seen clearly that the transmittance decreases with the reduction and the increased overall film thickness, whereas the smaller sheet resistance can be achieved simultaneously. Similar trends are observed in all reports as indicated by the bold arrows in Figure 1.4. As a result, efficient

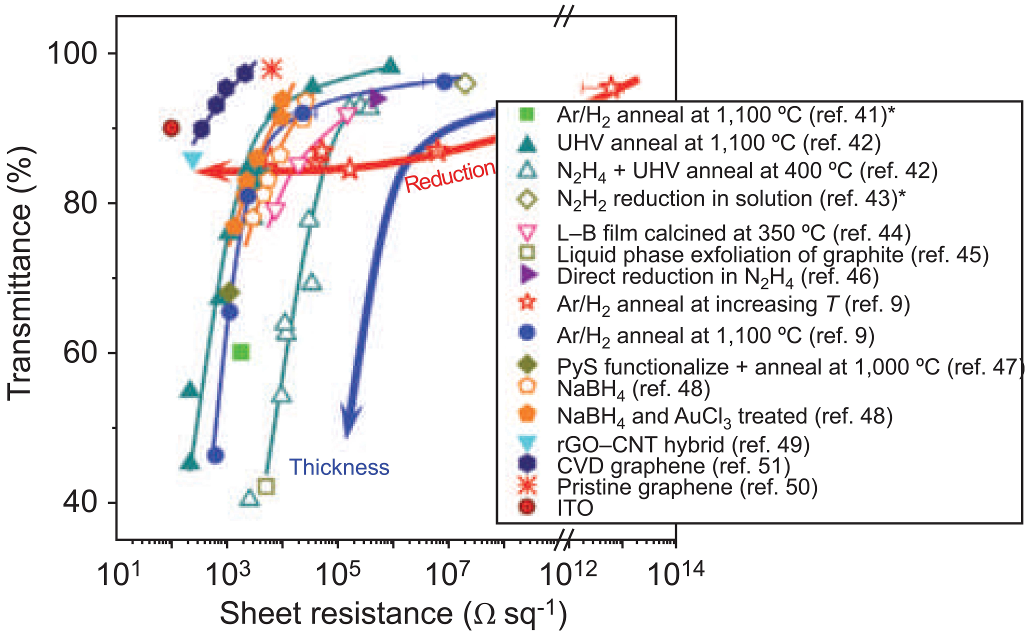

FIGURE 1.4: The transmittance at 550 nm as a function of sheet resistance of rGO films studied by varios groups in the literature[48].

reduction is the key to achieve highly conductive films, while the ability to controllably deposit films with nanometer thickness allows the high optical transparencies. Currently, the highest degree of reduction is achieved via pyrolysis at 1100 °C, yielding rGO films with the best performance[54]. And the sheet resistance as low as 1 kΩ·sq^{-1} of rGO at a transmittance of 80% has been reported, surpassing the performance of ITO and CVD graphene[54]. Such sheet resistance values are approximately one order of magnitude higher than those achieved with single-walled carbon nanotube thin films[55]. However, high-temperature thermal reduction should be avoided in order for rGO films to be competitive with other solution-processed alternatives to ITO and metal nanowire thin films that can be deposited at room temperature and used on plastic platforms[56]. Direct exfoliation and reduction of GO in hydrazine is a room-temperature route for producing highly reduced GO but yields films with moderate optoelectronic properties[57]. Therefore numerous efforts have been devoted in achieving efficient reduction of GO via less hazardous routes at the room temperature and doping, providing promising prospects[58–60].

Flexible electronics are emerging and promising technologies for next-generation, high-performance portable electronic devices[61], which demand the development of thin, lightweight, and flexible electrode materials. The deposition of rGO thin films with uniform and controllable thickness ranging from one to several layers has been reported on a solution-based method[62], enabling the use of rGO thin films as flexible electronic materials (shown in Figure 1.5a). Moreover, the mechanically flexible, macroporous three-dimensional (3D) carbon films with tunable porous morphologies have been demonstrated by integrating GO platelets using the self-assembling method, and the electrical properties of the GO films can be significantly enhanced through the pyrolysis or nitrogen doping process[63]. The surface resistance can be reduced to 13.4 Ω during the pyrolysis process followed by the nitrogen doping, corresponding to an electrical conductivity of 649 S/cm with the film thickness of 1.15 μm. In addition, various all-GO-based flexible electronic devices have been demonstrated recently including the all-rGO thin film flexible transistors (Figure 1.5b)[64], the all-rGO memory device[65] and the all-organic flexible gas sensor (Figure 1.5c,d) for the detection of nitrogen dioxide[39].

The optical devices and applications have also been investigated recently. The near-infrared (NIR), visible and ultraviolet (UV) fluorescence of GO and rGO have been observed as a consequence of their heterogeneous atomic and electronic structures[66–72]. The intrinsic and tunable fluorescence from GO and rGO, combined with their chemical versatility, tunability and solution processability, could open up exciting and previously unforeseen optical applications for graphene-based materials and make them attractive for numerous applications. The bio-imaging of live cells has been demonstrated by using the fluorescence from nanosized GO functionalised with polyethylene glycol[66,67]. The strong optical absorbance of GO in the NIR region has also been applied in vivo photothermal therapy, achieving ultra-efficient tumour ablation after intravenous administration and low-power NIR laser irradiation[73]. In addition, the fluorescence quenching with GO has been reported and a technique called fluorescence quenching microscopy has been developed, where GO or rGO provide dark contrast compared with the surrounding fluorescent

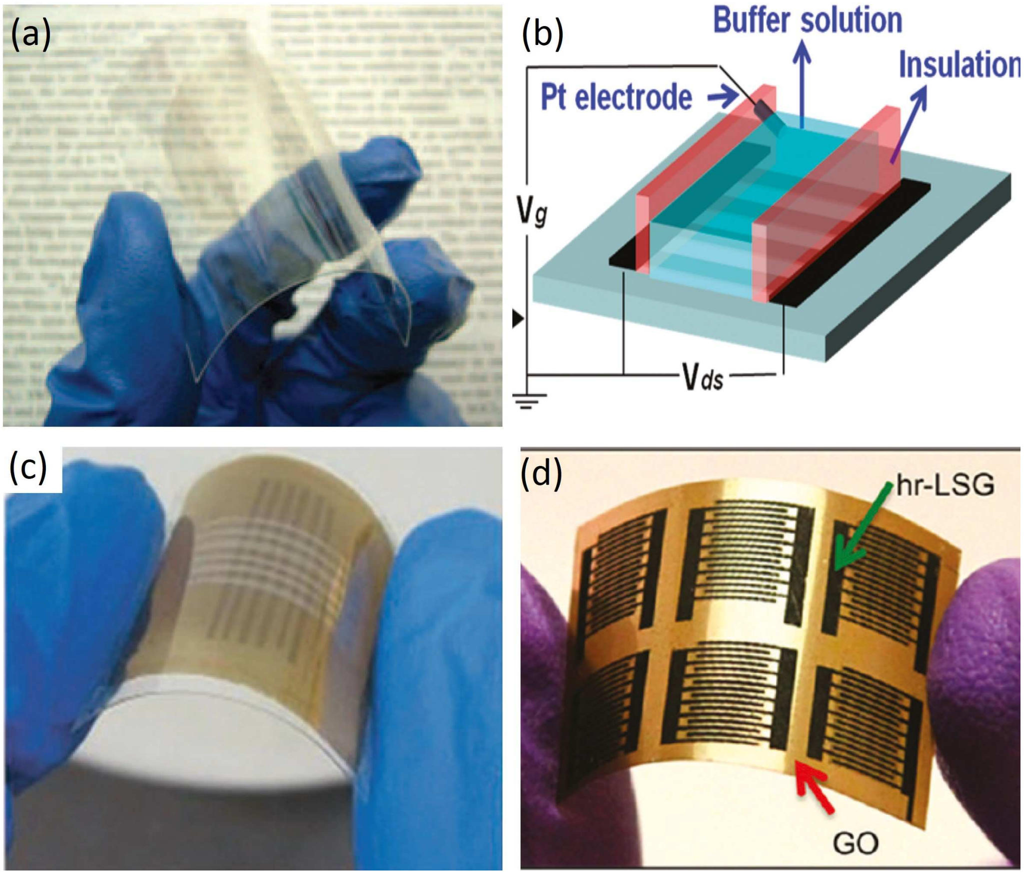

Figure 1.5: (a) Photograph of transparent GO thin films on plastic substrates[62]. (b)Schematic illustration of all-rGO thin film transistors[64]. (c) Photograph of the flexible memory device[65]. (d) All-organic flexible set of interdigitiated electrodes generated from highly reduced laser scribed graphene[39].

medium[74,75]. Moreover, the fluorescence quenching has been used as the basis of GO optical sensors for sensing single-stranded DNA and biomolecules[76–78], which is based on the fluorescence quenching of the dye-labelled DNA on binding with GO.

Although GO is often referred to as a disordered material due to the presence of the oxygen functional groups and the sp^2 and sp^3 bonds, great opportunities have been provided simultaneously for tailoring its chemical functionality and hence its physical properties. A variety of methods have been reported to achieve solution-based deposition of GO and GO-based composite thin films for electrical and optoelectronic applications including transparent conductors, thin film transistors, sensors, field emitters, photovoltaics, and flexible memory devices without extensive lithographic processing. GO provides an exciting platform for scientific research on engineering, physics, chemistry and 2D materials, and offers a unique route towards low-cost mass production, tunable optoelectronic properties and all carbon-based thin-film industry and technology. However, compared with the extensively demonstrated electronic and optoelectronic properties and devices, the tunable optical properties and photonic components of GO and rGO are less studied so far. In addition, the optical properties in the mid-infrared (MIR) is far less developed than that at shorter wavelengths due to the limited availability of suitable characterisation methods. Moreover, there is significantly more to be explored in understanding the structure, processing, and properties of GO and rGO given their highly chemical versatility. As a result, further cross-discipline efforts should be devoted to uncover the potential of GO and rGO in on-chip electronics, optoelectronics and, in particular, photonics.

1.2 Outline of thesis

The objective of this thesis is to investigate the fundamental optical properties of GO and laser-induced rGO with different laser reduction extents, to understand the underlying physical mechanisms responsible for their optical responses, and to realise functional optical components by using the DLW method for on-chip photonic applications. The outline of the thesis is summarised as follows:

Chapter 2 reviews the state-of-the-art optical properties as well as applications of GO and rGO. Firstly, the characterisation of the linear dispersion relations of GO and rGO has been discussed. Both the experimental approaches and the physical understanding have been reviewed and compared. We then review the nonlinear optical properties of GO and rGO including both the nonlinear absorption and refraction, demonstrating their optical responses under high intensity illuminations such as ultra fast lasers. Ultrathin flat lens is the first proposed optical component to be demonstrated on GO and rGO. As a result, a throughout review on the current ultrathin flat lenses has been provided with respect to the working principle, the lens performance and the manufacturing capabilities. Moreover, the ultrathin planar polariser has been reviewed as the second proposed optical component on GO. It should be emphasised that challenges and opportunities have been summarised particularly following all of the review sections respectively, raising the scientific questions to be addressed in the following chapters.

Chapter 3 focuses on the study of the linear optical properties of the GO and laser-induced rGO films. Firstly, the linear dispersion relations in the UV-Vis range (190 nm - 1.5 μm) have been investigated by using the spectroscope ellipsometer. Laser-induced rGO thin films at different reduction extents have been prepared and characterised. By fitting the measured ellipsometer data, both the linear refractive index and the extinction coefficient have been deduced. Then the linear dispersion relations in the infrared (IR) range up to 20 μm has been successfully characterised by using the Kramers-Kronig (KK) relations and the data in the visible range matches the ellipsometry measurement. Both the reflection KK method and the transmission KK method have been employed for the GO and laser-induced rGO films depending on the transmittance of the samples. Finally, the physical mechanisms of their conductivities have been discussed.

Chapter 4 investigates the nonlinear optical properties of the GO and laser-induced rGO films by using the Z-scan technique. Both the tunable nonlinear absorption and the nonlinear refraction (NLR) have been observed during the laser-induced reduction process. By fitting the Z-scan data, the nonlinear coefficients of the GO and laser-induced rGO films have been deduced. In addition, the hybrid GO and gold nanoparticle (AuNP) composite has been developed and its enhanced nonlinearity has been observed.

Chapter 5 realises an ultrathin GO flat lens by using the mask-free DLW technique on ultrathin GO films. Theoretical understanding and calculation of the lens have been carried out, and the experimental verifications show excellent consistence. The focusing resolution of the GO lens has been optimised based on the working principle. Moreover, the tuning ability as well as the broadband focusing have also been demonstrated. In addition, the flexible and bendable GO lens has been realised. Finally, the wavefront engineering capability of the ultrathin GO film has been discussed and additional diffractive optical elements have been demonstrated.

Chapter 6 proposes an ultrathin GO polariser in simulations based on the guided resonances in the 2D photonic crystal (PC) slabs by using the Finite-difference time-domain method. The extinction ratio of the polariser has been firstly optimised by modifying the structures of the 2D periodic array. Also the broadband operations have been studied based on the dispersionless nature of GO. Moreover, the performance of the GO polariser as a function of the incident angle has been investigated, showing the tolerance to the incident beam with a finite cross-section.

Chapter 7 summarises the research outcomes in this thesis. The perspectives and outlooks of this field have also been discussed.

Chapter 2

Literature review

2.1 Introduction

The responses of materials to external electromagnetic (EM) fields are the fundamental information for designing various optical components for different optical applications. Recently, GO and rGO have attracted a great deal of attention due to their unique physical and chemical properties, and a number of optoelectronic applications have been demonstrated. Compared with the extensively investigated electrical properties, the optical properties of GO or rGO are less explored. Also the optical properties of GO and rGO are highly sensitive to the oxygen functional groups, which make them challenging to characterise. However, the dispersion relations are the key parameters of GO and rGO towards their on-chip photonic applications.

In this chapter, the characterisations of the optical properties of GO and rGO have been reviewed firstly. Specifically, the linear dispersion relations of GO and rGO in both UV-Vis and IR ranges have been reviewed. Moreover, the nonlinear optical properties including nonlinear absorption and refraction have also been reviewed, revealing the optical responses of the materials under high intensity illuminations. Based on the linear and nonlinear optical properties, two potential applications on GO and rGO have been reviewed, which are the ultrathin flat lenses and the ultrathin planar polarisers. Finally, challenges and opportunities have been summarised following each of the literature review section respectively, raising the scientific questions that will be addressed in this thesis.

2.2 Linear optical properties

2.2.1 Review

The complex refractive index as a function of wavelength (dispersion relation) is the fundamental optical parameter to identify the responses of materials to an external EM field. Although the electrical properties of graphene-based materials have been extensively studied including field effect[5], anomalous quantum hall effect[6,11] and tunable electric conductivity[79], the optical studies, in particular the dispersion relations, have lagged due to the difficulties in film formation, ultrathin film thickness control (sub-nanometer), dielectric anisotropy, small lateral sample size, sparse distribution of the GO flakes on the substrate, and the limited optical characterisation methods available. Most importantly, the laser-induced reduction of GO films, as the main strategy in this thesis, is believed to generate complicated impacts on the GO film, and therefore lead to different dispersion relations of rGO films due to the diverse reduction mechanisms comparing to the thermal or chemical reductions. As a result, limited results on the optical properties of the GO and laser-induced rGO films have been reported so far. The traditional optical techniques have to be particularly tailored to determine their unsettled linear dispersion relations.

A straightforward approach to rapidly characterise the linear optical response of the GO and rGO films is the optical microscopy. The contrast between light reflected from the thin sheet and the substrate can be greatly enhanced by using a properly designed substrate under monochromatic illuminations. Based on the Fresnel's equations, a quantitative determination of the complex refractive index of the thin sheet can be calculated. Jung *et al.*[80] obtained the effective refractive index (n) and optical absorption coefficient (k) of GO films and thermally reduced rGO films by using the standard confocal microscopy. A single layer of GO can readily be identified with optical microscopy and the complex refractive index are obtained by comparing the measured contrasts. Moreover, as a consequence of the thermal reduction, the complex refractive index of rGO increases compared to that of GO. However, it should be pointed out that the complex refractive index can only be characterised at a few discrete wavelengths without knowing the overall dispersion relations.

Yang *et al.*[81] used a different spectroscopy method to obtain the refractive index of GO sheets. By comparing the reflection spectrum of GO with the background spectrum of SiO_2/Si, a contrast spectrum can be generated and analysed by using the Fresnel's equations. Hong *et al.*[82] performed time-domain terahertz (THz) spectroscopy on thermally reduced rGO and measured its refractive index in THz range with respect to the Drude free-electron model, which is characterised by a large scattering rate. Furthermore, they demonstrated that the refractive index of rGO can be manipulated by controlling the reduction process, which correlates well with the direct current conductivity above the percolation limit.

Among the various types of characterisation methods, spectroscopic ellipsometry is widely used to determine the complex refractive index as well as the thickness of thin films in a nondestructive manner. Jung *et al.*[83] measured the refractive index and the extinction coefficient of single- and multi-layer GO and thermally reduced rGO by imaging spectroscopic ellipsometry in the wavelength range of 350-1000 nm. Their measurements also demonstrated an increase in the effective values of n and k of GO after thermal treatment, as shown in Figure 2.1a,b. Moreover, the effect of thermal treatment of GO is believed to remove interlamellar water layers and reduce the oxygen content, which renders the material electrically conductive. Shen *et al.*[84] characterised the optical responses of GO and chemically reduced GO with the standard spectroscopic ellipsometry. By fitting the ellipsometric parameters with the Lorentz oscillator model, the bandgap tuning through the reduction process of GO is investigated in details. As shown schematically in

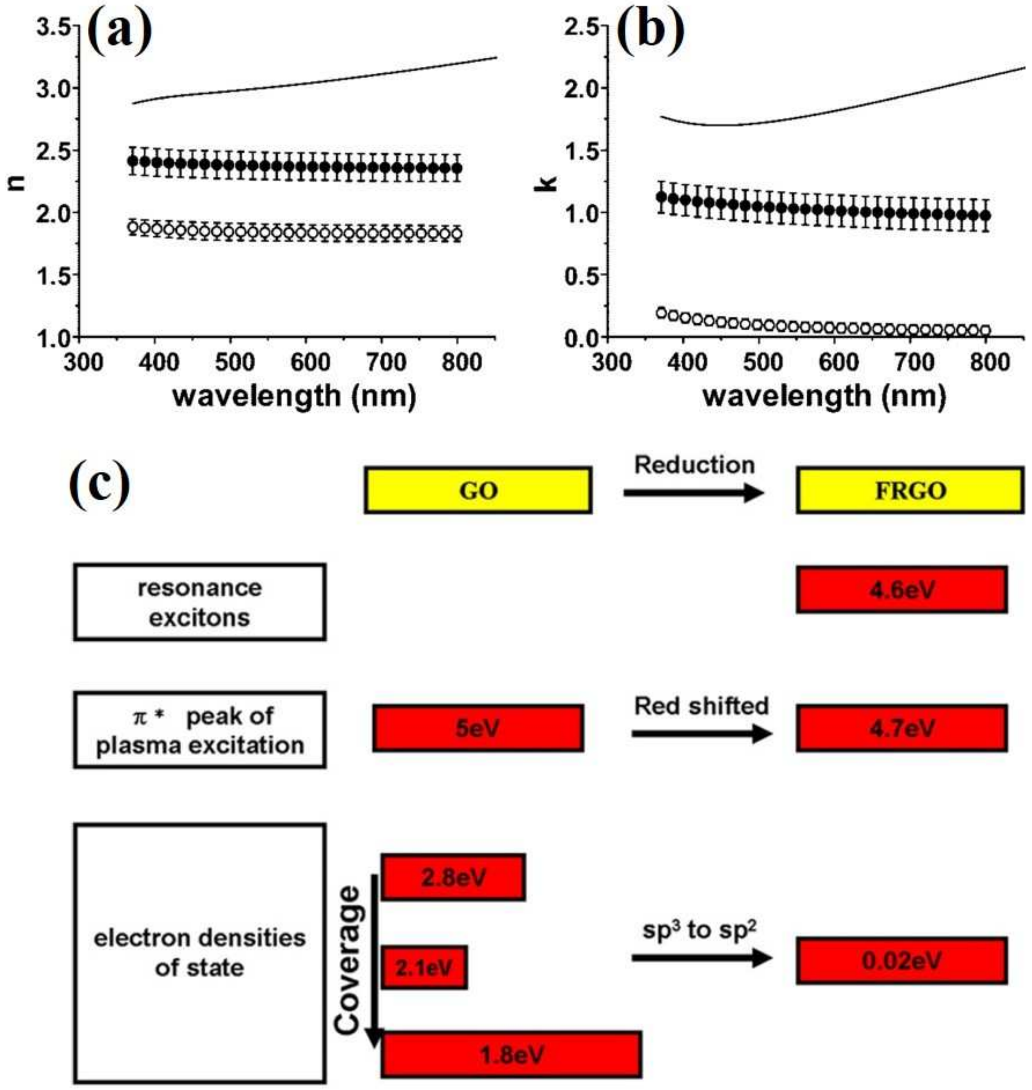

FIGURE 2.1: (a, b) Complex refractive index of GO before (○) and after (●) thermal treatment and of highly oriented pyrolytic graphite pieces (-)[83]. (c) Schematic diagram of the transitions of bandgap through the reducing process from GO to rGO[84].

Figure 2.1c, the bandgap of GO decreases from 2.8 eV, 1.8 eV to 0.02 eV during the reduction process with the functional groups removed gradually. The conductivity of rGO was also found to increase with the transition from sp^3 to sp^2 hybridisation of carbon atoms.

Table 2.1 summarises the research on the linear optical properties of GO and rGO based on materials, reduction method (if applicable), methodology, wavelength range, and the measured n and k values. It should be pointed out that more results on the linear refractive index characterisation of graphene have been reported and the methodologies are potentially applicable for all graphene-based materials. Therefore for completeness, the results on graphene have also been included in Table 2.1.

Table 2.1: Linear dispersion relations of graphene/GO/rGO (all experimental results)

Materials	Methodology	Wavelength Range	n, k value
rGO(Thermal)[80]	Microscopy	488, 532, 633 nm	2.1-0.55i at 633 nm
GO[80]	Microscopy	488, 532, 633 nm	2.0-0.3i at 633 nm
GO[81]	Spectroscopy	White light	1.2-0.24i
rGO(Thermal)[82]	Spectroscopy	1 THz	24
GO/rGO(Thermal)[83]	Ellipsometry	350-1000 nm	Dispersion
GO/rGO(Chemical)[84]	Ellipsometry	275-826 nm	Dispersion
GO/rGO(Chemical)[85]	Ellipsometry	260-800 nm	Dispersion
Graphene[80]	Microscopy	488, 532, 633 nm	2.5-1.3i at 633 nm
Graphene[86]	Microscopy	White light	2.0-1.1i
Graphene[87]	Microscopy	Dispersionless	2.6-1.3i
Graphene[88]	Picometrology	488, 532, 633 nm	3.0-1.4i at 633 nm
Graphene[89]	Spectroscopy	190-1000 nm	Dispersion
Graphene[90]	Ellipsometry	245-1700 nm	Dispersion
Graphene[91]	Ellipsometry	210-1000 nm	Dispersion
Graphene[92]	Ellipsometry	360-1000 nm	Dispersion
Graphene[93]	Ellipsometry	200-1000 nm	Dispersion

2.2.2 Challenges and opportunities

Although researchers have been investigating the linear optical responses of GO and rGO since 2007, a few topics are still unclear, but critical for GO photonics.

Firstly, few results on the linear dispersion relations of laser-induced rGO films have been reported so far. Compared with the thermal or chemical reduction, laser reduction is preferred for flexible manufacturing and localised modifications of rGO properties. However, linear refractive index of the laser-induced rGO is believed to be different with that of thermal or chemical rGO due to the reduction mechanisms. Also laser reduction of GO has the advantage to precisely tune the reduction extent and hence control the linear refractive index of rGO at will. As a result, it is of both fundamental and practical interest to investigate the linear dispersion relations of the laser-induced rGO films at various reduction extents.

The main challenge is the small transverse size of the laser-induced rGO films (usually hundreds of μm limited by the scanning stage), which is not possible to apply standard ellipsometry techniques (usually requires mm size samples).

Secondly, the dispersion relations of GO or rGO have not been modeled theoretically. During the ellisopmetry fitting process, different physical models can be used to match the measured dispersion relations of the material, which may provide fundamental insight into the theoretical dispersion relations. However, the dispersion relations of GO or rGO have been characterised by various fitting models including Cauthy, Drude and B-spline even without KK consistency[94]. And no conclusion has been reached on the dispersion theories of GO or rGO. In comparison, the optical conductivity of graphene has been successfully expressed as the Kubo formular[79]. Therefore, the dispersion theory of GO or rGO remains unclear.

Thirdly, the linear dispersion relations of GO or rGO in MIR or far-infrared (FIR) range are still missing. As summarised in Table 2.1, the measured refractive indices are mainly restricted in the visible to NIR range (up to 1.7 μm) due to the attainable wavelength range of ellipsometry. However, the dispersion relations in MIR and FIR are critical for not only the understanding of the dispersion theory of GO or rGO, but also the potential IR applications including photodetectors[95], biomedical imaging and sensing, and plasmonics[96]. As a result, new approaches need to be developed for measuring the dispersion relations of GO and rGO in the IR range.

2.3 Nonlinear optical properties

2.3.1 Review

Materials with large optical nonlinearities are indispensable for many potential applications including fast optical communications, all-optical switching, optical limiters and saturable absorbers[97]. Recently, surprising results have been reported on the nonlinear optical properties of graphene-based materials[54]. Liu *et al.*[98] investigated the different nonlinear mechanisms of GO solutions in nanosecond and picosecond regimes. They find that two-photon absorption (TPA) dominates the nonlinear absorption process of GO solutions in the case of picosecond pulses, while excited state absorptions (ESA) are responsible in the case of nanosecond pulses. Jiang *et al.*[99] studied the broadband optical limiting (OL) behaviours of the GO film and laser-induced rGO for femtosecond laser pulses at both 400 nm and 800 nm (Figure 2.2a). The laser-induced rGO showed enhancement of effective TPA coefficient by up to 19 times. Also the highly reduced GO film by chemical method displayed strong saturable absorption (SA) behavior. Liaros *et al.*[100] reported the nonlinear optical responses of some aqueous GO colloids under visible (532 nm) and IR (1064 nm), picosecond and nanosecond laser excitations, which present large broadband OL, SA, and negligible NLR. And SA was found for the low incident intensity whereas reverse saturable absorption (RSA) displayed at the higher intensity. Zhang *et al.*[101] observed the NLR properties of GO solutions in N-Dimethylformamide (DMF). The GO-DMF composite shows self-defocusing property in nanosecond time regime, which is mainly attributed to the transient thermal effect (Figure 2.2b).

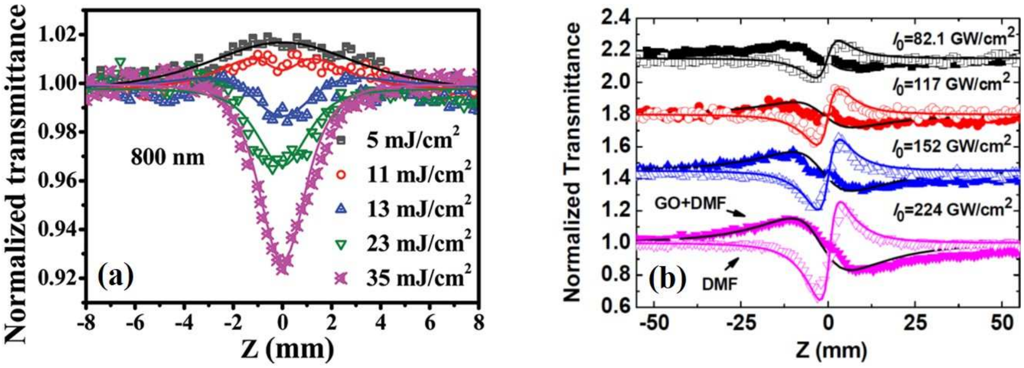

FIGURE 2.2: (a) Open aperture Z-scan results of a GO film at 800 nm under different input fluences[99]. (b) NLR Z-scan curves of the dispersion of GO solutions in DMF (solid icons) and the DMF-only sample (hollow icons). Solid lines are the theoretical fittings[101].

In addition, due to its 2D nature and presence of the oxygen functional groups, GO is readily functionalisable with complementary nonlinear optical materials in tandem configurations, or to be hybridised with organic dyes. Nalla *et al.*[102] prepared a conjugated polymer-GO composite, which exhibited both nonlinear absorption and NLR. Chantharasupawong *et al.*[103] synthesised the fluorinated GO solutions and observed the enhanced nonlinear absorption and nonlinear scattering (NS), which are an order of magnitude better than that of GO solutions. Liaros *et al.*[104] investigated the nonlinear optical responses of few layered GO dispersed in various organic solvents. Its nonlinear absorption was found to be significantly larger than that of single layered GO, depending upon the used solvents.

Table 2.2 summarises the researches on the nonlinear optical properties of GO and rGO based on materials, laser parameters, nonlinear behaviours, nonlinear mechanisms, and nonlinear coefficients.

TABLE 2.2: Nonlinear optical properties of GO/rGO (all experimental results)

Materials	Laser parameters*	Nonlinear behaviours	Nonlinear mechanisms	Nonlinear coefficients
GO (film)[99]	N/A, 20, 800, 1 kHz, 100 fs	SA#, OL	ESA, TPA	β=31 cm/GW
GO nanoribbons[105]	30, N/A, 532, 1 Hz, 8 ns	OL	TPA, NS	N/A
GO colloids[100]	20, 30, 532, 10 Hz, 4 ns	SA, OL	ESA	β=130 cm/GW
GO (solution)[98]	10, 20, 532, N/A, 35 ps	SA, RSA	TPA	β=2.2 cm/GW
	10, 20, 532, N/A, 35 ps		ESA	β=56 cm/GW
Fluorinated-GO (solutions)[103]	20, 30, 532, N/A, 5 ns	OL, RSA	TPA, NS	β=90 cm/GW
GO-TPP& (film)[102]	N/A, 20, 800, 1 kHz, 200 fs	SA, OL, self-defocusing	N/A	n_2= -0.05 cm^2/GW
				β=20 cm/GW
GO-DMF[101]	15, 12, 532, 10 Hz, 10 ns	SA, RSA, self-defocusing	TPA	β=0.37 cm/GW
	25, 16, 532, 10 Hz, 35 ps			n_2= -1.4$\times$10^{-6} cm^2/GW
	25, 31, 800, 1 kHz, 120 fs			n_2= -1.1$\times$10^{-6} cm^2/GW

*Laser parameters are summarised as effective focal length (cm), beam width (μm), wavelength (nm), repetition rate and pulse width (ns: nanosecond, ps: picosecond, fs: femtosecond)

#Abbreviations are OL (optical limiting), SA (saturable absorption), TPA (two-photon absorption), RSA (reverse saturable absorption), NS (nonlinear scattering) and ESA (excited state absorption).

&TPP: Sodium salt of poly[2-(3-thienyl)exthoxy-4-butylsulfonate]

2.3.2 Challenges and opportunities

Although the nonlinear properties of graphene-based materials have been extensively investigated, there are still several barriers to be overcome towards GO nonlinear optical applications.

Firstly, for high performance integrated photonic device design, the third-order nonlinearity, in particular the NLR (Kerr effect, n_2), is crucial for novel functionalities including all-optical switching, signal regeneration and fast optical communications[106,107]. However the research on nonlinearities of GO is largely limited to the nonlinear absorption such as OL or SA for modulating the light intensity. The experimental investigations on the Kerr nonlinearity have only been conducted in GO solutions or composites, which are not directly relevant to the properties of a GO film and challenging to be used for solid state integrated photonic devices. As a result, the GO film with considerable NLR has not been developed yet.

Secondly, it is expected that rGO should display different nonlinearities due to the removal of the oxygen functional groups. However the nonlinear activities during the process of the laser-induced reduction from GO to rGO have remained unexplored, which are the key for realising the functionality in the patterned optoelectronic devices.

Thirdly, because there is an on-going demand on increasing the optical nonlinearity of GO or GO-based hybrids, the required interaction length of light with the nonlinear media can be significantly reduced with a larger nonlinear coefficient, enabling a high level of miniaturisation[108]. This is particular critical for nonlinear materials with a significant linear loss, such as GO. As a result, an ultrathin film with less optical absorptions and ultrahigh nonlinearities is required to ensure sufficient signal transmission through the devices.

2.4 Ultrathin flat lens

2.4.1 Review

The optical lens has been playing a critical role in almost all areas of science and technology since its invention about 3000 years ago. With the advances in micro- and nanofabrication techniques, continued miniaturisation of the conventional optical lenses has always been requested for various applications such as communications, sensors, data storage and a wide range of other technology-driven and consumer-driven industries[109–111]. In particular, the rapid development in nano-optics and on-chip photonic systems has placed stringent demand for ultrathin flat lenses with 3D subwavelength focusing capabilities[112–114].

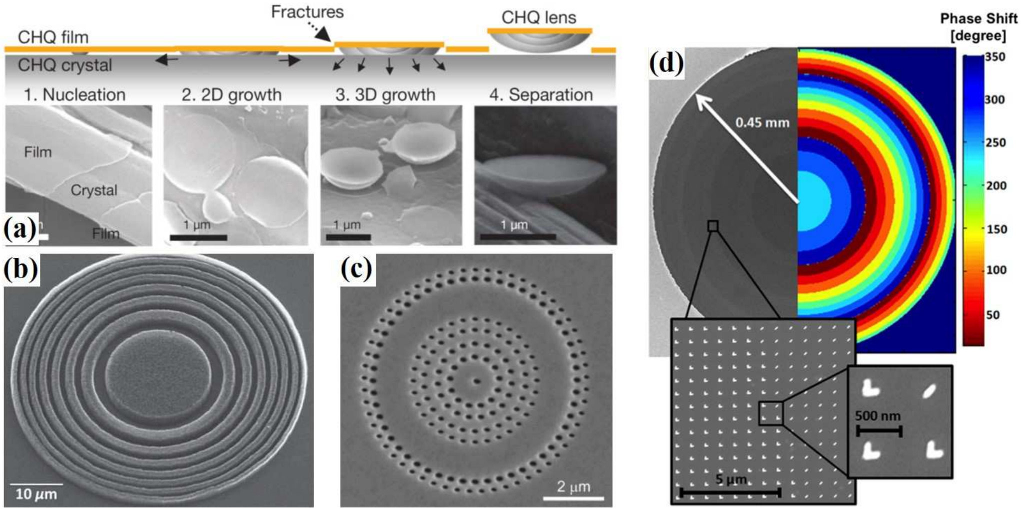

Figure 2.3: (a)Schematic diagrams and scanning electron microscope (SEM) images showing the self-assembly of lenses[115]. (b)SEM image of carbon nanotube Fresnel lens fabricated on silicon substrate. (c)SEM image of the holey metal lens[116]. (d)The SEM image of the fabricated metalens and the corresponding phase shift[117]. Inset: close up of patterned antennas.

The essence of optical lenses relies on the wavefront shaping of the incident light by manipulating its phase, amplitude and/or polarisation to realise a spherical wavefront on the exit plane. For the traditional refraction-based optical lenses, the wavefront shaping is mainly attributed to the phase modulation caused by the path length differences which can only be achieved gradually as the light propagating through the lens materials. As a result, the strength of the light bending is limited by the attainable refractive index of a given dielectric, which restricts the minimum lens size and thickness[118]. Li *et al.*[115] reported near-field high resolution by nanoscale spherical lenses that were self-assembled by the bottom-up integration of organic molecules (Figure 2.3a). Their results show near-field magnification that is able to resolve features beyond the diffraction limit. However complicated fabrication methods are required to make such conventional micro-lenses, including lithography or self-assembly methods[115,119]. In contrast, the Fresnel zone plates, which comprise alternating transparent and opaque zones to achieve amplitude modulation for wavefront shaping, offer the possibility of designing light weight and thinner lenses. Rajasekharan *et al.*[120] developed a carbon nanotube Fresnel lens made by exploiting the near-perfect optical absorption property of the nanotubes together with silicon nanofabrication techniques (Figure 2.3b). However, part of the incident light is reflected or absorbed by the opaque zones, which results in great losses and hence degrades its focusing performance. Moreover, the Fresnel zone plates use diffraction instead of refraction, which makes it inherently narrow banded[121]. A more successful design is the refractive-based Fresnel lenses, known as the phase-reversal zone plate[122]. Instead of blocking out every other zone, the entire plate is transparent with carefully designed thickness contrast and/or refractive index contrast between the adjacent zones, which offers the required phase delay.

In the last few years, plasmonic lenses and metasurfaces have opened up a new era for building ultrathin planar focusing devices[109–111,116,117,123–128]. Plasmonic lenses are based on nano-aperture or nanoslit arrays with varying geometries in a thin metal film (Figure 2.3c), and the phase profile is acquired accumulatively for waves propagating through the plasmonic or photonic waveguide modes supported by the nano-apertures. In contrast, the control of the wavefront using metasurfaces is achieved via the phase shifts experienced by radiation as it scatters off the optically thin antennas comprising the metasurfaces[117]. In addition, the progresses in artificial metamaterials as well as metasurfaces provide new avenues to build hyperlenses and metalenses that are able to image beyond the diffraction limit[110]. Through a magnification mechanism, hyperlenses are able to project super-resolution information to the far-field. However, hyperlenses lack the ability to focus plane waves and cannot realise the Fourier transform function due to the lack of a phase compensation mechanism. By introducing an abrupt interfacial phase discontinuity, metalens are proposed to not only super-resolve subwavelength details but also enable optical Fourier transforms. Although theoretical analysis and numerical simulations have proven its deep subwavelength focusing performance, experimental demonstrations of super-resolution metalens are still missing to prove the practical feasibility. Super-oscillatory lens has been demonstrated to achieve imaging resolution experimentally, but the subwavelength hotspot is not a real well-defined focal spot and the super-resolution imaging is achieved by disturbing the fragile interference balance of super-oscillation, which requires image reconstruction and therefore reduces the imaging speed[129].

To compare various ultrathin flat lenses and their performance, Table 2.3 summarises the current research on ultrathin flat lenses based on lens type, geometry (thickness and size), manufacturing method, constitute materials, working wavelength, the full width at the half maximum of the focal spot in xy (FWHM_{xy}) and yz (FWHM_{yz}) plane, the focal length (FL) and focusing efficiency.

Table 2.3: Ultrathin flat lens (all experimental results)

Lens type	Thickness	Size	Manufacturing	Materials	Wavelength	FWHM_{xy}	FWHM_{yz}	FL	Efficiency
Conventional[115]	<800 nm	3 μm	self-assembly	CHQ**	472 nm	200 nm	N/A	N/A	N/A
Conventional[130]	500 μm	200 μm	DLW	Silica	633 nm	1.7 μm	12.3 μm	N/A	N/A
Fresnel lens[131]	>15 μm	1 cm	Lithography	LC	633 nm	N/A	N/A	50 cm	39%
Fresnel lens[132]	500 μm	100 μm	DLW	Silica	632.8 nm	0.5 μm	N/A	60 mm	71 %
Fresnel lens[133]	>500 μm	250 μm	DLW	PMMA	633 nm	2 μm	N/A	0.5-5 mm	30%
Fresnel lens[134]	120 μm	400 μm	DLW	Silica	632.8 μm	8.2 μm	N/A	3 mm	37.6%
Fresnel lens[120]	>12 μm	38 μm	Lithography	Nanotube	633 nm	20 μm	N/A	158 μm	12 %
Fresnel lens[135]	3 mm	400 μm	DLW	Silica	633 nm	7 μm	N/A	3 mm	2 %
Fresnel lens[136]	30 μm	2 mm	DLW	Silica	633 nm	N/A	N/A	1 cm	17 %
Fresnel lens[137]	N/A	10 μm	FIB	Glass	633 nm	600 nm	N/A	500 nm#	N/A
Super Ocsillation[129]	100 nm	40 μm	FIB	Aluminum	640 nm	185 nm	N/A	10.3 μm	N/A
Plasmonic lens[116]	380 nm	7.26 μm	FIB	Gold	488, 531, 647 nm	2 μm	5 μm	12 μm	N/A
Plasmonic lens[123]	N/A	2D	FIB	Gold	637 nm	880 nm	6.23 μm	5 μm	N/A
Plasmonic lens[124]	140 nm	7.2 μm	FIB	Silver	850 nm	2.3 μm	15 μm	25 μm	N/A
Plasmonic lens[138]	180 nm	5 μm	FIB	Gold	500-780 nm	1.3 μm	4 μm	8-12.5 μm	N/A
Metasurface[117]	60 nm	0.9 mm	EBL	Gold	1.55 μm	100 μm	1.55 μm	3 cm	1%
Metasurface[125]	50 nm	17.3 μm	EBL	Gold	700-1000 nm	800 nm	2.3 μm	12 μm	14-27%
Metasurface[139]	200 nm	N/A	Lithography	Aluminum	0.45-0.75 THz	N/A	N/A	N/A	N/A
Metasurface[127]	100 nm	mm	Lithography	Gold	400 μm	260 μm	1 mm	4 mm	1%
Metasurface[126]	40 nm	80 μm	EBL	Gold	740 nm	1 μm	4 μm	60 μm	5%
Metasurface[140]	40 nm	180 μm	EBL	Gold	740 μm	7.2 μm	N/A	80 μm	5%
Metasurface[118]	30 nm	4 μm	FIB	Gold	476-676 nm	630 nm	2 μm	2.5-10 μm	10%*

*Transmission throughput

#Near field focusing

**Abbreviations are CHQ (calix[4]hydroquinone), EBL (electron-beam lithography), FIB (focused ion beam), PMMA (poly(methyl methacrylate)) and LC (liquid crystals).

2.4.2 Challenges and opportunities

Although tremendous effects have been devoted in developing ultrathin flat lenses, it is still challenging to achieve micro optical lenses with 3D subwavelength focusing resolution, high focusing efficiency, broadband operation, ultrathin thickness, low-cost manufacturing and flexible integration capability.

For conventional or Fresnel lenses, the attainable lens thickness, focusing resolution and efficiency are all dependent on the phase delay. Therefore, large local refractive index modifications of materials and thickness variations induced after manufacturing are required to provide sufficient phase delay. However, the local refractive index modifications of conventionally available dielectrics, which have been utilised for Fresnel lens so far, such as fused silica glasses and poly(methyl methacrylate) (PMMA), are found to be below 10^{-2}[133]. As a result, the thickness of the lens must be comparable to the operational wavelength to compensate the limited local refractive index modification.

Although plasmonic lenses and metasurfaces have inspired great interests in the applications of flat optics, they have limitations that cannot be neglected. First of all, the subwavelength nanoholes or antennas need to be designed individually in order to achieve the desirable phase profile, which present complex design rules and significant manufacturing challenges. Also material losses are an intrinsic property of metallic materials at the optical wavelengths, limiting the ultimate resolution as well as the focusing efficiency, especially when subwavelength hole arrays or resonant elements are involved[109]. Focusing efficiency of 10% is the theoretical limit and only 1% focusing efficiency has been realised experimentally[117], which greatly hampers its practical applications. Moreover, certain polarisation state of the incident light is required to achieve the designed phase profile, and the focusing ability may be affected under other polarisation states, which reduces the flexibility of the light sources[116]. Finally, the phase shift relies on the resonant features of the plasmonic structures, and it is therefore wavelength-dependent in general. Away from the optimal wavelength, the phase gradient and uniformity of the amplitude of each antenna cannot be maintained, which limits its broadband focusing abilities[141].

Although pioneering work has been carried out to achieve optical images with subwavelength resolutions even beyond the diffraction limit, including Pendry-Veselago negative index superlens[112], near-field scanning microscopy as well as fluorescence-based imaging methods, these super-resolution approaches necessitate the lens either to be in the near proximity of the object, or work only for narrow class of samples such as intensely luminescent or sparse objects. Moreover, there is no experimental demonstration on the subwavelength resolution in the axial direction (yz plane). Also these scanning- or random sampling-based non-projection techniques achieve super-resolving power by sacrificing the imaging speed, making them uncompetitive for dynamic imaging. As a result, the lens-based far-field imaging system remains the best option for more practical high-speed applications.

2.5 Ultrathin planar polarisers

2.5.1 Review

Polarisation is a basic but important characteristic of light wave conveying valuable information or signal in many optical systems. It is of great interest to manipulate the polarisation for many applications such as optoelectronics, life science microscopy, and display applications[142]. Conventional methods for advanced polarisation control rely on the use of anisotropic or chiral materials, demanding stringently on the intrinsic material properties and the interaction lengths between light and materials. Therefore, specific minimum thickness, bulky configurations and moderate performance are the key limitations greatly restricting the potential applications of the conventional polarisers in miniaturised optoelectronic or photonic systems.

Recently, enormous efforts have been devoted to realise miniaturised ultrathin polarisers. Novel concepts have been widely put forward both experimentally and theoretically including plasmonic resonators, metamaterials[143], metasurfaces[144], wire-grid structures[145], and guided resonances[146]. Grady *et al.*[143] demonstrated ultrathin, broadband, and highly efficient metamaterial-based THz polarisation converters that are capable of changing a linear polarisation state into its orthogonal one. Near-perfect anomalous refraction has been realised (Figure 2.4a). Ahn *et al.*[145] fabricated a 50 nm half-pitch wire-grid polariser with a polarisation extinction ratio over 2000 and the transmission of 85% at the wavelength of 450 nm (Figure 2.4b).

Meanwhile, photonic crystal (PC) has attracted a great deal of attention due to its broad applications in integrated optics such as telecommunications[147], sensing[148], imaging[149], optical switching[150], etc. In particular, PCs have been demonstrated to interact with external EM fields through the out-plane modes known as the guided resonances in the structure. Similar to the in-plane guided mode, the EM field is strongly confined within the PCs as guided resonances, whereas it can couple to the external radiation easily, providing an efficient way to channel light from within the PC slab to the external environment. As a result, the out-plane guided resonances of PCs have found many applications in novel PC-based devices such as light-emitting didoes[151,152], lasers[153,154], and directional output couplers[155]. In addition, the optical spectra (transmission or reflection) of the externally incident field can be significantly affected by the guided resonances, resulting in complex resonance signatures, which are useful for polarisation sensitive applications[156].

Fan *et al.*[146] presented a theoretical understanding of the complex spectral properties of guided resonances in a PC slab. Both the dispersion diagrams and the transmission or reflection spectra of these resonances have been calculated with a plane-wave band-structure computation method. The spectra are found to consist of sharp resonant features superimposed upon a smoothly varying background, which can be explained as the Fabry-Perot oscillations when light interacts with a uniform dielectric slab (Figure 2.4d). On the other hand, the sharp resonant

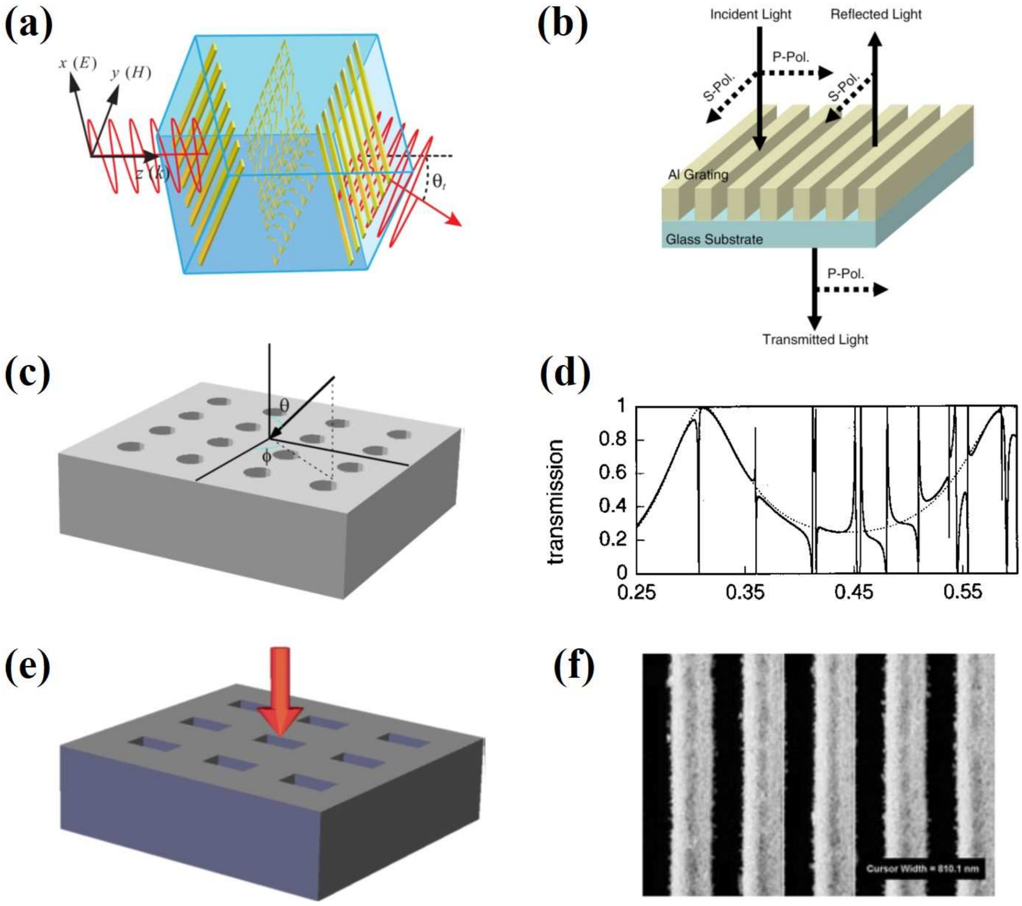

FIGURE 2.4: (a) Anomalous refraction design. A normally incident x-polarised wave is converted to a y-polarised transmission beam, which bends in the x-z plane to an angle θ_t with respect to the z axis[143]. (b) The schematic view of a wire-grid polariser[145]. (c) Schematic figure of a 2D PC structure consisting of a square lattice of circular air holes in a dielectric slab. The colatitude angle (θ) and azimuthal angle (ϕ) have been labeled accordingly[157]. (d) The transmission spectrum of the 2D PC slab. The dashed line is for a uniform dielectric slab with a frequency-dependent dielectric constant[146]. (e) The PC slab structure with asymmetric rectangular air holes for generating anisotropic polarisation dependent responses[157]. (f) SEM images of the fabricated polariser. The grating period is 810 nm[156].

features come from the guided resonances of the PC slab. As a result, two pathways in the transmission process have been proposed, which are the direct transmission process and the indirect portion from the guided resonances. Therefore, a general and intuitive theory has been introduced to explain the complexities in the line shapes, which is attributed to the interference between the direct transmission (or reflection) and the exponential decaying waves of the resonances.

The manipulation of the polarisation sensitive guided resonances has also been extensively investigated. Lousse *et al.*[157] studied the angular dependence (Figure 2.4c) and polarisation sensitivity by reducing the rotational symmetry of the structure (Figure 2.4e). They demonstrated the complete reflectivity with a wide angular range and a polarisation splitter, reflecting one polarisation completely while allowing 100% transmission for the other polarisation. Boutami *et al.*[158] reported a broadband reflectors with a strong sensitivity of the polarisation dependence by modifying the circular air holes into the elliptical ones. Zhou *et al.*[159] reported that the polarisation dependence can also be achieved by increasing the incident angle. Moreover, Lee *et al.*[156] presented an experimental result on guided resonance-based polariser using a 500-nm-thick layer of amorphous silicon on a glass substrate (Figure 2.4f) using electron-beam lithography (EBL) and plasma etching fabrication methods. A grating with period of 820 nm is fabricated to form an overall 300 μm × 300 μm area. The polariser has high and low transmittance for transverse-electric and transverse-magnetic polarisations, respectively, showing an experimental extinction ratio of 97 at a central wavelength of 1510 nm.

To compare various ultrathin polarisers and their performance, Table 2.4 summarises the current research on ultrathin polarisers based on polariser type, constituting materials, manufacturing method, thickness, working wavelength, the efficiency (optical output) and extinction ratio.

Table 2.4: Ultrathin polarisers for integrated optical applications (all experimental results)

Polariser type	Materials	Manufacturing	Thickness	Working wavelength	Efficiency	Extinction ratio
Wire-grid[160]	Al, Au	Evaporation coating	N/A	2 μm - 15 μm	80% at 5 μm	126 at 5 μm
Wire-grid[161]	Al	Lithography	1 μm	16 μm -70 μm	63% at 16 μm	18 at 16 μm
Wire-grid[162]	Al	Evaporation coating	>2 mm	2 μm - 30 μm	80% at 6 μm	150 at 6 μm
Wire-grid[163]	Al on chalcogenide	Lithography	>2 mm	6 μm - 12 μm	70% at 8 μm	100 at 11 μm
Wire-grid[164]	Al on Silicon	Lithography	0.5 mm	10 μm - 20 μm	70%	2000
Wire-grid[165]	WSi on SiO_2	two-beam lithography	0.5 mm	0.65 μm - 1.5 μm	80%	100
Wire-grid[166]	Au on Tsurupica	Evaporation coating	0.5 mm	0.5 THz - 3 THz	90%	10000
Guided resonance[156]	Si on SiO_2	EBL and Plasma etching	500 nm	1550 nm	97%	97 at 1510 nm
Guided resonance[167]	Si_3N_4 on SiO_2	UV laser fabrication	N/A	1565 nm	97%	360
Guided resonance[168]	Si on MgF_2	DLW	474 nm	2.8 μm - 3.4 μm	95%	100 at 3 μm
Anisotropic material[169]	GO on polymer	drop-casting	2 μm	0.65 μm - 1.64 μm	N/A	7 at 0.65 μm
Metamaterial[170]	Si	FIB	N/A	1550 nm	74%	N/A
Grating waveguide[171]	Si	EBL and Plasma etching	N/A	1550 nm	80%	100

2.5.2 Challenges and opportunities

Although ultrathin polarisers have been extensively studied both theoretically and experimentally, there exist major challenges as well as opportunities towards the practical applications.

For wire-grid polarisers, the periodicity of the grating is much smaller than the working wavelength. Therefore, limited by the fabrication technology it is still challenging to fabricate wire-grid polarisers in the visible or NIR range. In addition, substrates are required to support the subwavelength metallic wire-grid structures. As a result, the absorption bands of various substrates have placed limitations on the working wavelengths of the polarisers. Moreover, the extinction ratio and the efficiency of the polarisers are greatly restricted by the considerable metallic losses, in particular, in the shorter wavelength ranges.

For guided resonance-based polarisers, the constituting materials are greatly limited to Silicon or Indium phosphide due to the conventional available materials in the IR range. As a result, time consuming and cost-ineffective manufacturing methods are required to form the polarizers including EBL, reactive-ion etching (RIE) and plasma etching. Although the frequency of the guided resonance can be easily manipulated by modifying the geometries of the PC slab, there hardly exists any transparent materials with broad bandwith from visible to IR. Therefore the operation wavelength has been greatly limited to 1550 nm. As a result, the broadband guided resonance-based polarisers especially in the visible range has not been demonstrated. Finally, the flexible optical devices are highly demanded for the ultracompact, integratable and on-chip photonic applications, but now they are still missing. Therefore, ultrathin planar polarisers with high transmission efficiency, high extinction ratio, flexible and integratable capabilities, and cost-effective manufacturing methods are highly demanded.

Chapter 3

Linear optical properties of graphene oxide

Characterisation and understanding the fundamental optical properties of materials are the essential steps before any practical optical designs or applications. In general, the optical properties can be categorised into two schemes with respect to the intensity of the EM field, which are the linear dispersion relations and the optical nonlinearities. The linear dispersion relations reveal the information on the reflection, refraction, transmission, and absorption of the materials at various wavelengths, whereas the optical nonlinearities are critical for harmonic generation, multi-photon absorption, and Kerr effect etc. As discussed in the previous chapters, the optical properties of GO and rGO are highly sensitive to the oxygen functional groups in terms of the type, the fraction and their distributions on the basal plane, and hence limited results or understanding have been obtained so far. As a result, the optical properties of GO and rGO are urgently required towards their on-chip photonic applications.

In this chapter, the linear optical properties of the GO and laser-induced rGO films with certain thicknesses will be investigated thoroughly. In particular, the broadband linear dispersion relations from the UV to MIR regions will be characterised by using the spectroscope ellipsometry and the KK methods.

Independent characterisations from spectroscope ellipsometry and KK methods have been compared, and excellent consistence has been achieved. The tuning of the optical bandgap of GO during its laser reduction process has been investigated. Finally, physical mechanisms of the conductivity variations during the reduction process have been discussed.

3.1 Dispersion relations of graphene oxide in the visible range

In this section, the linear dispersion relations of GO thin films and laser-induced rGO thin films at different reduction extents will be studied experimentally by using the spectroscopic ellipsometer (SE). High quality GO thin films with controllable thicknesses have been prepared for the SE measurements. Large laser-induced rGO areas (1 cm^2) with increasing reduction extent have been fabricated by using the multi-focal laser fabrication technique, which enables parallel line patterning on the GO thin film. The SE with a focused spot ($\sim$ 500 μm) has been used to characterise the phase and amplitude information of the reflected beam. By fitting the measured values, the linear dispersion relations of the GO and laser-induced rGO films at different reduction extents have been investigated.

The GO solutions are synthesised by the chemical reduction of graphite via a modified Hummers method[47]. Specifically, graphite and $NaNO_3$ are mixed with concentrated H_2SO_4. By vigorous stirring, the reducing agent ($KMnO_4$) is added into the suspension. Then H_2O_2 is added into the mixture at 98°C. The product is washed and dried, and then the GO sheets are obtained after the purification. A deionised water/methanol mixture with an optimal ratio of 1:5 is used to disperse the GO flakes. Finally a cover glass is carefully cleaned with water, and the uniform GO thin films are produced by a spin-coating method onto the glass surface.

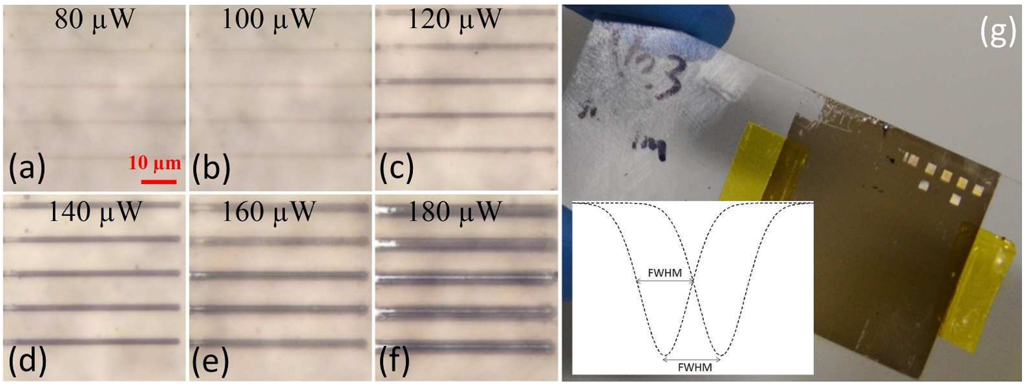

Figure 3.1: (a)-(f) Parallel line structures have been fabricated on the GO thin films at various laser powers of 80 μW, 100 μW, 120 μW, 140 μW, 160 μW and 180 μW, respectively. (g) The fabricated large rGO areas on the GO thin films at various laser powers. Inset: The spacing of the adjacent lines is fixed as the FWHM of the Gaussian beam distribution.

Standard ellipsometer techniques are commonly used for sensitive measurement of thin film thicknesses and optical constants. However, it is challenging to use the standard SE to characterise the GO film due to the generally required sample size of millimetre scale. The typical width of femtosecond laser-induced rGO line is on a $\sim$ μm scale, which makes it impossible to apply the standard SE method straightforwardly.

To enable the measurements of the dispersion relations of the GO film as well as the laser-induced rGO film, two improvements have been applied. Firstly, focused beam ellipsometer has been used. The spot size of the beam has been reduced to 500 μm^2 by utilising the focusing probes. Even smaller FWHM of the focal spot ($\sim$ 30 μm) can be achieved depending on the used objective. Secondly, large area of rGO zones reduced with different laser powers have been prepared by using the multi-focal laser fabrication techniques[172], as shown in Figure 3.1. In order to ensure the uniformity of the laser exposed large rGO zones to be suitable for the optical measurements, consecutive lines attaching properly are fabricated. The spacing of the adjacent lines is fixed as the FWHM of the Gaussian beam distribution (see the inset in Figure 3.1g) to guarantee the identical exposure of all the laser illuminated areas. Furthermore, the multi-focal laser fabrication technique has been used to speed up the entire process and also to improve the uniformity of the large scale rGO zones.

By tuning the used laser powers, the reduction extent can be controlled as shown in Figure 3.1a-f. The fabricated rGO lines become darker as the laser power increases, corresponding to the increase of the absorption coefficient of rGO. The line width and film thickness of the rGO lines as a function of the used laser powers have been measured and summarised, as shown in Figure 3.2. The line width is found to increase from 0.8 μm to 1.3 μm when the laser power increases from 80 μW to 180 μW, whereas the film thickness reduces from 200 nm to 100 nm. Also the fabrication line width and the film thickness of the laser-induced rGO thin films are both controlled by the laser power, and therefore these two correlated parameters should be designed simultaneously in the GO optical devices based on laser patterning. As a result, the spacing of the adjacent rGO lines can be easily determined, and large scale rGO zones (1 mm^2) have been fabricated on the GO thin film with different reduction extents (see Figure 3.1g), which are suitable for our focused beam ellipsometer measurements.

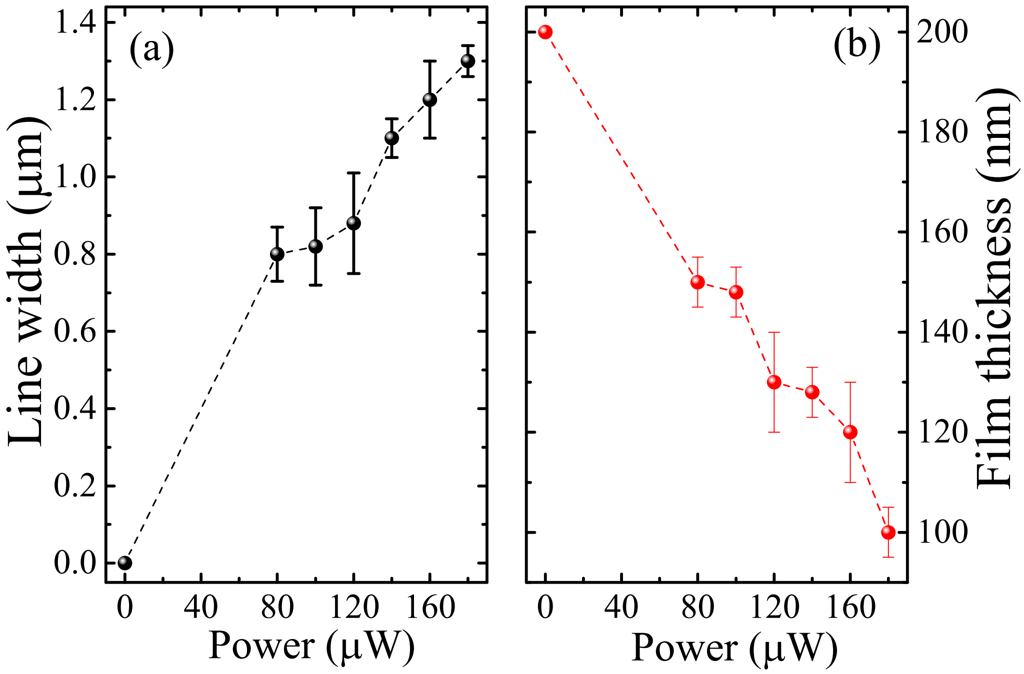

FIGURE 3.2: (a) The fabricated line widths of rGO at different laser powers have been characterised by using SEM. (b) The film thicknesses of rGO fabricated at different laser powers have been identified by using a SE.

The J.A. Wollam M-2000 spectroscopic ellipsometer is used to characterise the optical constants of the GO thin films. The working principle of an ellipsometer is to measure the reflection of a polarised light beam from a sample. Specifically,

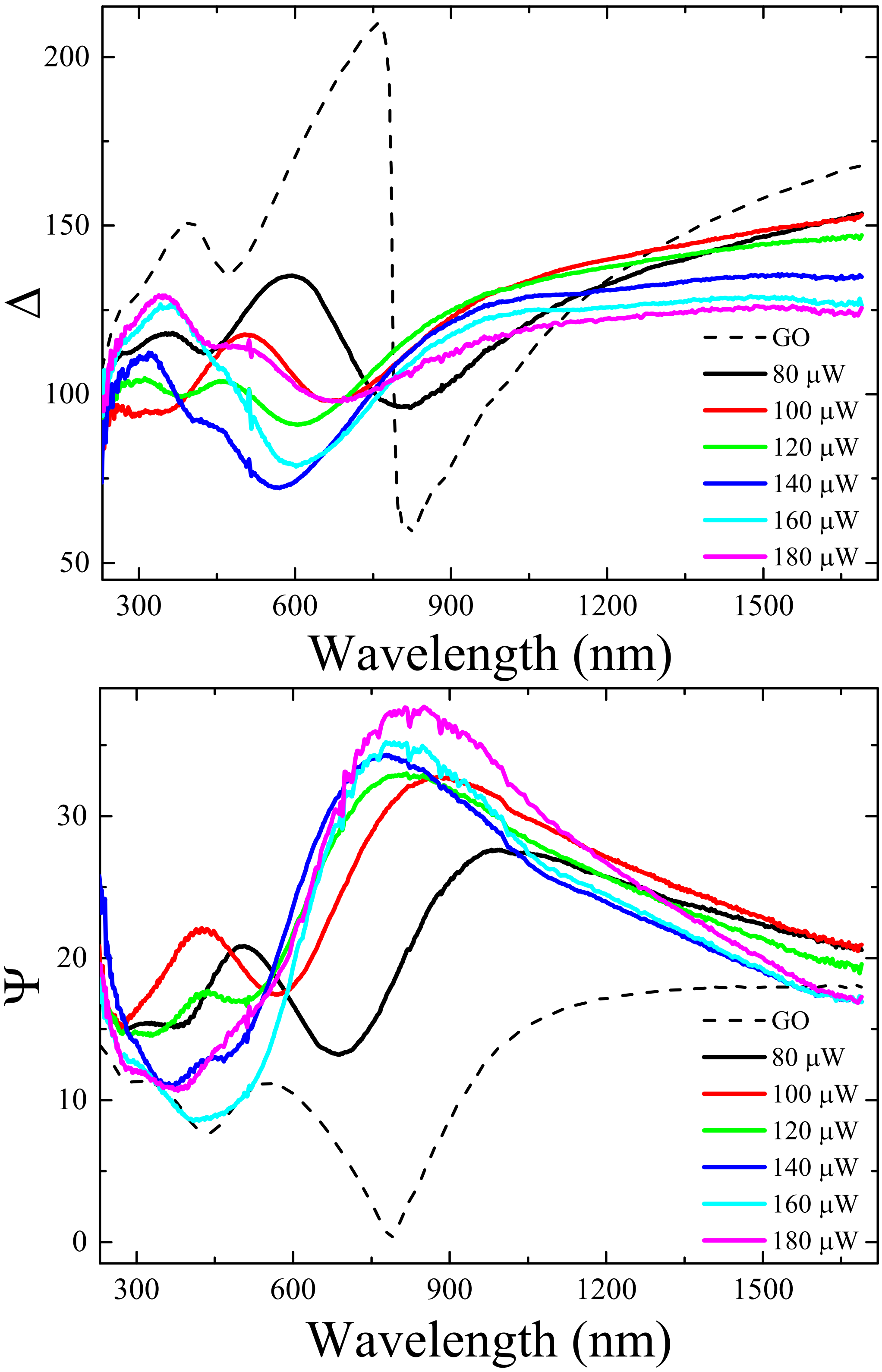

FIGURE 3.3: The measured values of Δ (a) and ψ (b) of the GO and laser-induced rGO films at different reduction extents.

both the incident light beam and the reflected light beam are the superposition of the orthogonal s- and p-polarisation components. The ellipsometer measures the ratio of the amplitude reflection coefficients of both s-polarisation (r_s) and p-polarisation (r_p), which can be defined as:

$$r_p/r_s = \tan\psi e^{i\Delta}$$

where $\psi = \arctan(|r_p|/|r_s|)$ and Δ is the phase difference between r_s and r_p. The dispersion relations as well as the thickness of the sample can be obtained by fitting the measured values of ψ and Δ properly.

Figure 3.3 shows the measured ψ and Δ of both GO and rGO films at different reduction extents (identified by the used laser power from 80 μW to 180 μW). Although the linear dispersion relations are unaccessible directly from the measurements, some typical behaviours of GO and rGO can be predicted. First of all, compared to the reference GO film (black dash line), all the rGO samples display the different ψ and Δ, which indicates large dielectric constant variations between GO and rGO samples. Secondly, both ψ and Δ change monotonically as the laser power increases, which further verifies the monotonic increase of the reduction extent. Finally, larger variations of ψ and Δ in the visible range (<1000 nm) have been observed in comparison to those in the NIR range (1000 nm - 1700 nm), corresponding to the possible larger absorption in the visible range.

To obtain the sample properties of interest, such as the the film thickness, the refractive index (n) and the extinction coefficient (κ), a model-based analysis of the SE data has to be performed. Although various models are available in the SE data analysis approach, the adapting of the proper model is the key to achieve the accurate n and κ values. Compared to transparent films (e.g. silicon dioxide), SE measurements on absorbing films are more difficult to analyse. The reason is that the general material model for the dispersion relations of the absorbing film is not always known before the measurement. Therefore, the “B-Spline” model and the “Gen-Osc” model are the main general film types to handle absorbing

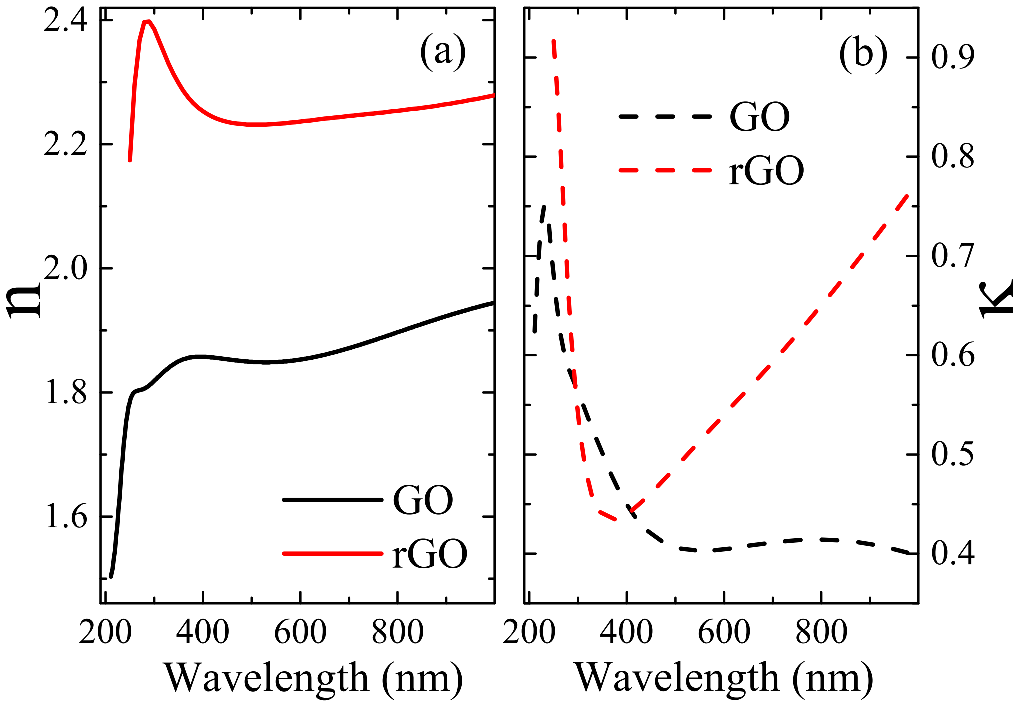

FIGURE 3.4: (a) The dispersion relations of refractive index of GO and rGO. (b) The dispersion relations of extinction coefficients of GO and rGO.

film analysis problems. In particular, B-spline model allows arbitrary flexibility in n and κ versus wavelength. However, the physically meaningful KK consistency, which determines the correlations of the optical constants, is not always guaranteed in the B-Spline model. Furthermore, many fitting parameters are required by the B-Spline film, which may result in correlation in the data fit. As a result, a B-Spline film is used to fit the SE data of the GO and rGO films initially, which allows arbitrary flexibility in n and κ values.

After the initial B-Spline modeling, the Gen-Osc film, which uses a summation of the standard oscillator lineshapes such as Lorentz and Drude models, is employed to model the absorbing features by describing the shape of the absorption. Finally the dispersion relations of the GO and rGO films with the highest reduction extent have been fitted from 200 nm to 1000 nm and shown as Figure 3.4. GO film shows an almost dispersionless refractive index of 1.9 above 400 nm, which further proves the broadband optical property of GO. However the refractive index of GO decreases immediately in the UV range, which is due to the abnormal dispersion from the strong absorption of GO in that range[94]. On the other hand, the extinction coefficient of GO film keeps as low as 0.4 above 400 nm and increases obviously in the UV range, which is consistent with the refractive index behaviours. The dispersion relation of the laser-induced rGO film with the largest reduction extent shows a similar trend compared to that of the GO film. However, both the n and κ values are found to increase and the absorption peak redshifts compared to that of the GO film, which is consistent with the UV-Vis spectra of the GO and rGO films[47]. As a result, the fitted high accuracy dispersion relations of both GO and laser-induced rGO films have not only validated the used fitting model, but also shed some light on the laser reduction mechanisms compared to the more widely used thermal and chemical reduction methods.

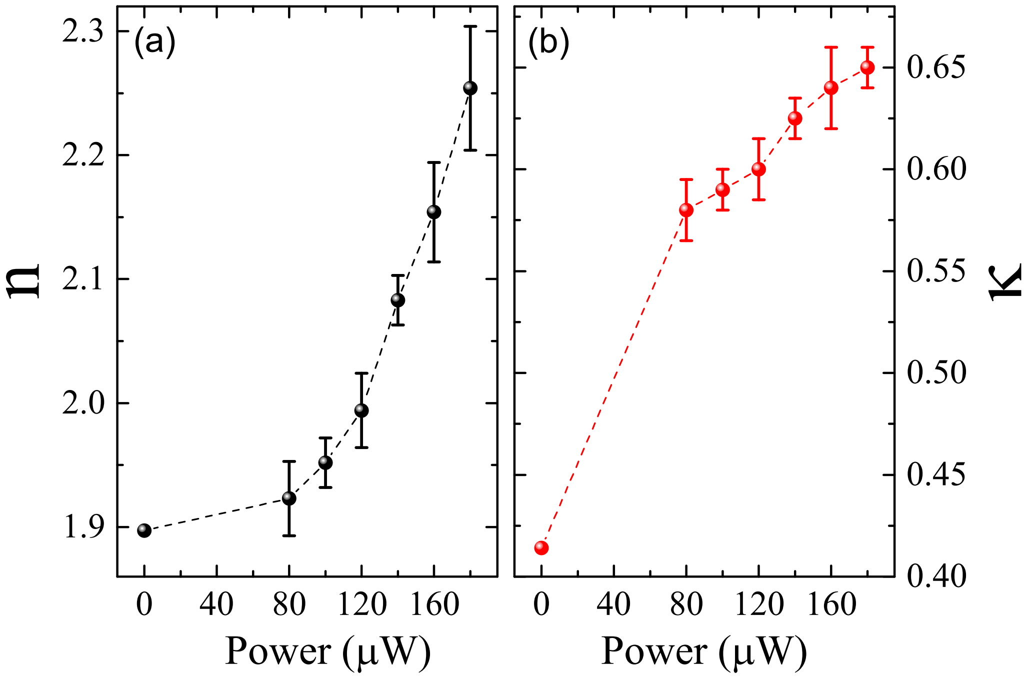

FIGURE 3.5: (a) The power dependent refractive index of the laser-induced rGO film at different reduction extents. (b) The power dependent extinction coefficient of the laser-induced rGO film at different reduction extents.

It is widely believed that the optical properties of GO are strongly linked to the oxygen functional groups[54]. Partially or fully removal of the oxygen functional groups may lead to the tuning of the dispersion relations of rGO. As a result, to further understand the behaviours of laser reduction of GO film, the dispersion relations of the rGO films at different reduction extents are fitted and shown as a function of the used laser powers (see Figure 3.5). Both the refractive index and the extinction coefficient of the laser-induced rGO films are found to increase as the laser power increases. Specifically, the refractive index difference between GO and rGO films is as large as 0.4, which is one order of magnitude larger compared to the traditional photo sensitive materials[133]. Meanwhile, the extinction coefficient increases from 0.4 to 0.65, corresponding to the enhanced absorption of rGO film compared to that of GO film. It has been reported that the optical constants of multilayer graphene are smaller than that of bulk graphite due to a possible decrease in interlayer interaction for a small number of layers[86,87]. Also the increase of n and κ values for the multi-layer thermally reduced GO stack is greater than the increase found in the case of thermally treated single or few layer (but still thin) GO sheets[83]. As a result, the differences in optical constants of the laser-induced rGO films may also be due to the influence of the interlamellar water. It has been measured that the thickness of rGO films upon laser patterning reduces obviously (see Figure 3.2b), which can be explained as a change in the thickness of the interlamellar water. Therefore, the laser patterning of GO film removes a significant amount of water. For thermal reduction of GO, a qualitative understanding of the influence of changing the amount of interlamellar water in multilayer stacks shows that the removing of water layer yields a significantly increased value for n, but only a slightly increased κ value[83]. As a result, it can be envisioned that the effect of laser reduction is to remove interlamellar water, which leads to the increase of refractive index. On the other hand, the rGO films become more metallic upon the laser annealing due to the recovery of sp^2 conjugation, which results in the significant increase of extinction coefficient.

In conclusion, the dispersion relations of the GO films and laser-induced rGO films at different reduction extents in the visible to NIR range have been characterised by using the focused beam SE technique. By fitting the measured ψ and Δ values using the B-Spline and Gen-Osc models, the KK consistent is guaranteed. Moreover, tunable optical properties can be achieved by carefully controlling the laser powers. The changing of both refractive index and extinction coefficient are attributed to the removal of interlamellar water and the oxygen functional groups, respectively. The SE studies of the GO and laser-induced rGO films show the potential of laser patternable GO films for the diverse photonic on-chip applications that can not be achieved by the traditional photo sensitive materials.

3.2 Dispersion relations of graphene oxide in the infrared range

Although the linear dispersion relations of graphene, GO and rGO have been studied, the wavelength range is strictly limited from the visible to NIR range (up to 1.7 μm), as summarised in Table 2.1. However the dispersion relations of GO and rGO films in the MIR or FIR ranges are critical for the IR photonic applications including IR photodetectors, surface plasmons, biosensing and imaging, and IR optical sources. Moreover, unlike the well characterised conductivity of graphene using the Kubo formula[173], the similar theoretical description for GO or rGO films has not yet been demonstrated. In fact, the optical properties are believed to be determined by the functional groups of the materials. As a result, the type, coverage and location of the various oxygen functional groups in GO film have made it challenging to develop an ideal theory for its conductivity.

In principle, the optical constants of solids can be determined in two ways, either from intensity measurements using unpolarised light (spectrum method) or from polarisation measurements (ellipsometry). The polarisation measurements require the nonnormal incident light whereas the intensity measurements can be performed either at normal incidence or at nonnormal incidence. As a result, the normal incidence intensity measurement is insensitive to polarisation effects, and roughness or contamination of the sample, which shows a better accuracy. Most importantly, various spectroscopic methods from the UV to THz range are available to perform intensity measurements, greatly extending the attainable wavelength range. It should be pointed out that a model-based fitting process is also required to deduce the optical constants from the intensity measurements. And two types of the KK methods are used in this section, which are the KK method in reflection mode and in transmission mode. Finally the linear dispersion relations of the GO and laser-induced rGO films have been investigated in the IR range up to 20 μm by using the spectra measurements. And the conductivity and optical bandgap of GO and rGO have been deduced and analysed, which may provide some clues for understanding the optical properties of GO from the visible to MIR range.

3.2.1 Kramers-Kronig relations

The linear optical properties of materials can be described using the complex material parameters including the dielectric constant $\vec{\varepsilon}$, the conductivity $\vec{\sigma}$, and the refractive index $\vec{N}_c$, which denote the change of the fields and current when an EM field is present. It should be pointed out that all of the parameters are complex vectors and can be expressed with 6 different parameters:

$$\begin{cases} \vec{\varepsilon} = \varepsilon_1 + i\varepsilon_2 \\ \vec{\sigma} = \sigma_1 + i\sigma_2 \\ \vec{N}_c = n + ik \end{cases}$$

Although 6 different parameters have to be determined to characterise the responses of materials, they can be related by solving the Maxwell equation and linked as:

$$\begin{cases} \sigma_1 = \frac{\omega\varepsilon_2}{4\pi} \\ \sigma_2 = (1-\varepsilon_1)\frac{\omega}{4\pi} \\ \varepsilon_1 = n^2 - k^2 \\ \varepsilon_2 = 2nk \end{cases}$$

The real part of conductivity (σ_1) can be calculated from the imaginary part of permeability (ε_2), and the imaginary part of conductivity (σ_2) is linked with the real part of permeability (ε_1). Meanwhile, the permeability can be deduced once $\vec{N}_c$ is given. As a result, all of the 6 parameters will be determined once one complex response function ($\vec{\varepsilon}$, $\vec{\sigma}$, or $\vec{N}_c$) is given. However, it is still challenging to obtain the dispersion relations of any of the three complex vectors straightforwardly.

TABLE 3.1: KK relations

Conductivity $\vec{\sigma}$	Permeability $\vec{\varepsilon}$	Refractive index $\vec{N}_c$
$\sigma_1(\omega) = \frac{2}{\pi} P \int_0^\infty \frac{\omega' \sigma_2(\omega')}{\omega'^2 - \omega^2} d\omega'$	$\varepsilon_1(\omega) - 1 = \frac{2}{\pi} P \int_0^\infty \frac{\omega' \varepsilon_2(\omega')}{\omega'^2 - \omega^2} d\omega'$	$n(\omega) - 1 = \frac{2}{\pi} P \int_0^\infty \frac{\omega' \kappa(\omega')}{\omega'^2 - \omega^2} d\omega'$
$\sigma_2(\omega) = -\frac{2\omega}{\pi} P \int_0^\infty \frac{\sigma_1(\omega')}{\omega'^2 - \omega^2} d\omega'$	$\varepsilon_2(\omega) = -\frac{2\omega}{\pi} P \int_0^\infty \frac{\omega'^2 [\varepsilon_1(\omega') - 1]}{\omega'^2 - \omega^2} d\omega'$	$\kappa(\omega) = -\frac{2}{\pi\omega} P \int_0^\infty \frac{\omega'^2 [n(\omega') - 1]}{\omega'^2 - \omega^2} d\omega'$

Based on the causality, various expressions connecting the real and imaginary parts of the complex response functions have been derived, which were firstly given by Kramers and Kronig[174] and known as the KK relations. As a result, the complex permeability, refractive index or conductivity can be evaluated when only one optical parameter is measured. Different KK relations are available for the complex response functions respectively, which have been summarised in Table 3.1.

By using the KK relations, all of the 6 physical parameters can be calculated once the dispersion of one of them is determined. However, the KK relations are non-local in frequency. The real (imaginary) part of the complex response function at a certain frequency ω is related to the behavior of the imaginary (real) component over the entire frequency range. This request posts great challenge to experiments because it is impossible to cover an infinite range of frequencies. In practice, the experimental data have to cover a spectral range as wide as possible in order to obtain more accurate optical parameters by using the KK relations.

3.2.2 Reflection Kramers-Kronig method

Although the real and imaginary parts of the optical constants are correlated by using the KK relations, it is impossible to measure any of the 6 parameters directly in the experiments. As a result, an additional KK relation has been developed to provide an experimental approach, which can be expressed as[94]:

$$\begin{cases} \ln|\vec{r}(\omega)| = \frac{1}{\pi} P \int_{-\infty}^{\infty} \frac{\theta(\omega')}{\omega'-\omega} d\omega' \\ \\ \theta(\omega) = -\frac{1}{\pi} P \int_{-\infty}^{\infty} \frac{\ln|\vec{r}(\omega')|}{\omega'-\omega} d\omega' \end{cases}$$

The equations describe the relation between the amplitude ($|\vec{r}(\omega)|$) of the measurable reflected beam from a bulk sample and its phase shift ($\theta(\omega)$). Then the refractive index and extinction coefficient can be calculated from $|\vec{r}|$ and θ through:

$$\begin{cases} n(\omega) = \frac{1-|\vec{r}(\omega)|^2}{|\vec{r}(\omega)|^2 - 2|\vec{r}(\omega)|\cos(\omega) + 1} \\ \\ \kappa(\omega) = \frac{2|\vec{r}(\omega)|\sin(\omega)}{|\vec{r}(\omega)|^2 - 2|\vec{r}(\omega)|\cos(\omega) + 1} \end{cases} \tag{3.1}$$

In principle, by experimentally measuring the reflectivity, the phase shift can be calculated through the reflection KK relation, and the 6 optical parameters are determined with the $|\vec{r}(\omega)|$ and $\theta(\omega)$ values through Equation 3.1. However, it is still challenging to apply the reflection KK method directly on the GO sample due to a few fundamental prerequisites. Firstly, only the reflection from the first interface of the sample should be included in $\vec{r}(\omega)$[94], which requires a large sample thickness with absolute zero transmission over the entire frequency range of interest. However, GO film has a comparatively low absorption above 500 nm. Therefore, in our experiment thick GO papers (~ mm scale) have been prepared to guarantee the absolute zero transmission from the visible to IR range. Secondly, gas generations have been reported in the laser reduction of the GO films[175]. Considerable surface roughnesses of the laser-induced rGO films, in particular when the thickness is large, will introduce inaccuracies in the reflection spectrum measurements. As a result, an integration sphere is applied to collect all the reflected light in the UV-Vis spectrometer system. Thirdly, the normal incident reflection is required in the reflection KK method[94]. As a result, a low numerical aperture (NA) objective is used in the fourier transform infrared spectroscopy (FTIR) spectrometer measurement without inserting the pin hole to largely eliminate the oblique incidences.

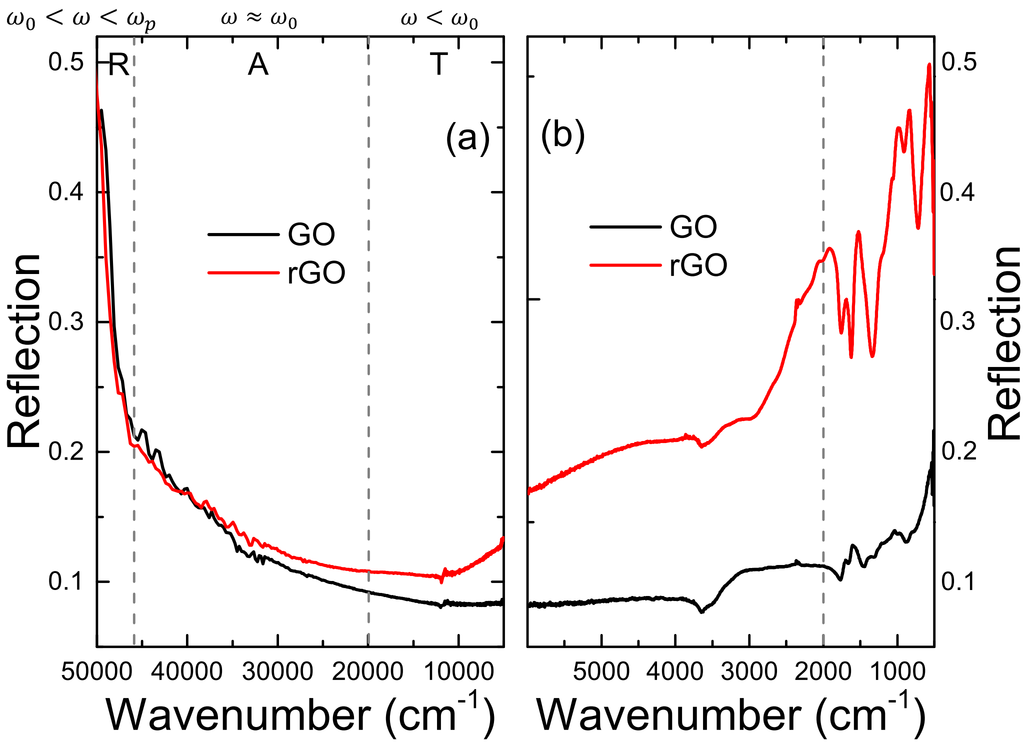

FIGURE 3.6: (a) The reflection spectra of the GO and laser-induced rGO films from the UV to visible range measured by a UV-Vis spectrometer. Three regions have been distinguished as transparent (T), absorption (A) and reflection (R) according to the Lorentz dispersion theory. (b) The reflection spectra of the GO and laser-induced rGO films in the IR range measured by a FTIR spectrometer. By using the low NA (0.2) objective, the normal incident is approximately achieved.

The reflection spectra of both GO and rGO films from the UV to visible range have been measured by using the PerkinElmer UV-Vis spectrometer working in the reflection mode at the normal incidence (Figure 3.6a). Meanwhile, the Bruker 70v FTIR spectrometer is used to obtain the reflection spectra of GO and rGO films in the IR range (Figure 3.6b). As a result, the reflection spectra have been measured over a large wavelength range from 200 nm (50000 cm^{-1}) to 20 μm (500 cm^{-1}). According to the Lorentz dispersion theory[94], the reflection behaviour can be categorised into four regions based on the frequency of the incident light (ω) and the fundamental frequency of the material (ω_0). In the low frequency range ($\omega < \omega_0$), the material is usually transparent with neither significant absorption nor reflection, displaying the normal dispersion, in which the refractive index increases for higher frequencies. In the case of $\omega \approx \omega_0$, the incident light is greatly absorbed by the material and the refractive index decreases with the increase of frequency, showing the abnormal dispersion. When $\omega_0 < \omega < \omega_p$ (ω_p is the plasma frequency), the incident light cannot penetrate the material and the large reflection as well as almost zero refractive index can be observed. Further increasing ω till $\omega \gg \omega_0$, the material becomes transparent with zero absorption and normal dispersion is observed.

Therefore, the measured reflection spectra of the GO and laser-induced rGO films in the UV-Vis range can be very well explained by the Lorentz theory, as shown in Figure 3.6a. It can be seen that the reflection is around 0.1 in the visible range (below 20000 cm^{-1}), corresponding to the $\omega < \omega_0$ case (T region in Figure 3.6a). Furthermore, the reflection increases dramatically above 20000 cm^{-1} due to the significant absorption when $\omega \approx \omega_0$ (A region in Figure 3.6a). Finally large reflection can be predicted approaching UV region (above 45000 cm^{-1}), which means the $\omega_0 < \omega < \omega_p$ (R region in Figure 3.6a). In the IR range, various peaks and valleys of the reflection curves have been observed especially in the MIR range (below 2000 cm^{-1}), as shown in Figure 3.6b. This is due to the significant absorptions from the different oxygen functional groups on GO and rGO films. Therefore different dispersion models other than the Lorentz theory should be used to explain their optical behaviours in the MIR or FIR regions. It is found that the reflection of the laser-induced rGO film is larger than the GO film over the entire band, indicating the overall increasing of the refractive index of laser-induced rGO compared to that of GO. However, obvious absorptions of the laser-induced rGO film in the IR range have been observed, indicating the limited reduction extent due to the challenges of reducing the thick GO paper using our laser system. Also the magnitude of reflection measured by the FTIR is smaller than that from the UV-Vis spectrometer. In the UV-Vis spectrometer system, the integration sphere is used to collect all the reflected light, which makes the measurement insensitive to surface roughness. However, a low NA objective is used in the FTIR spectrometer to measure the reflection, which leads to the loss of some of the reflected light. Therefore the magnitude of reflection in the IR range has been normalised to the UV-Vis range.

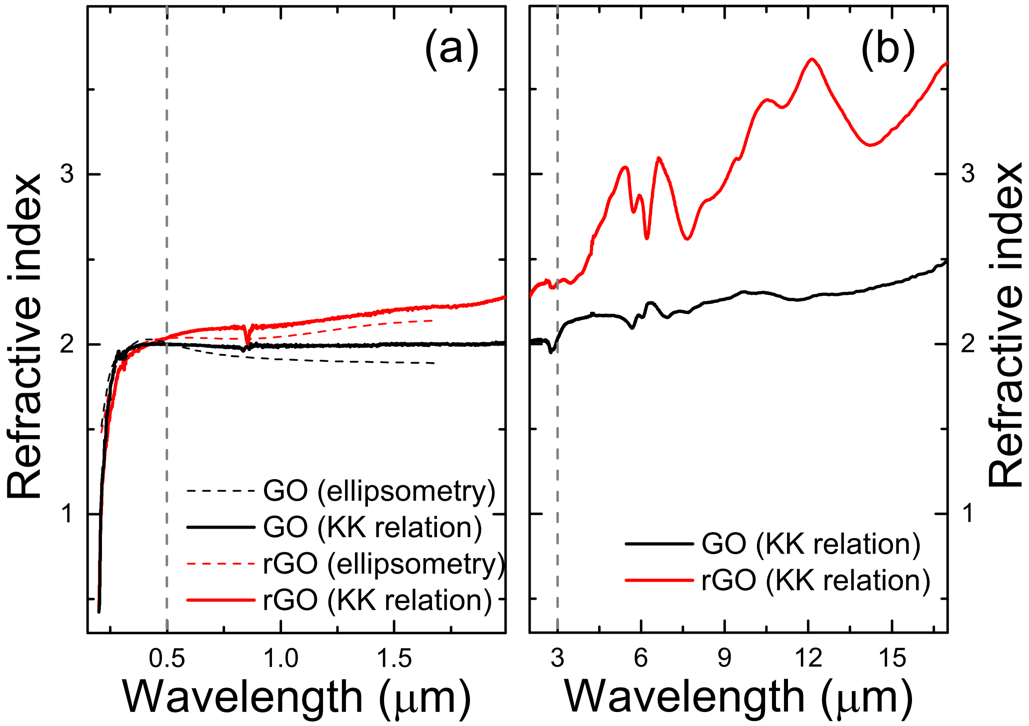

FIGURE 3.7: The deduced refractive index of GO and rGO from the visible (a) to the IR (b) ranges using the reflection KK relations. The refractive index in visible range (200 nm to 1700 nm) measured by using the ellipsometer is also provided as a reference (dash line in (a)).

The refractive index of the GO (solid black line in Figure 3.7a) and laser-induced rGO film (solid red line in Figure 3.7b) from 200 nm to 20 μm have been calculated by using the reflection KK relations (Equation 3.1). The ellipsometer measured refractive indices have also been provided as a reference. It should be emphasised that a good match of the refractive indices has been achieved by using two different methods, which further validates the acceptable accuracy of the reflection KK method in our GO films although finite spectral range has been used. The behaviour of the refractive index can also be distinguished into three regions as those in the reflection spectra. Firstly in the MIR region (above 3 μm), the refractive index is found to decrease as the frequency increases, which shows the abnormal dispersion due to the significant absorption from the oxygen functional groups[94]. Furthermore, from the visible to NIR range (500 nm to 3 μm), the dispersionless refractive index is observed, corresponding to the nearly transparent region of the materials. Below 500 nm the refractive index decreases dramatically due to the significant interband absorption of GO and rGO films, showing the abnormal dispersion relations. In comparison, the refractive index of rGO film is larger than that of GO film from the UV to IR ranges, whereas the increase is greatly limited compared to thin GO film shown in Figure 3.5, indicating the limited reduction extent of the thick GO paper by the laser due to the finite penetration depth.

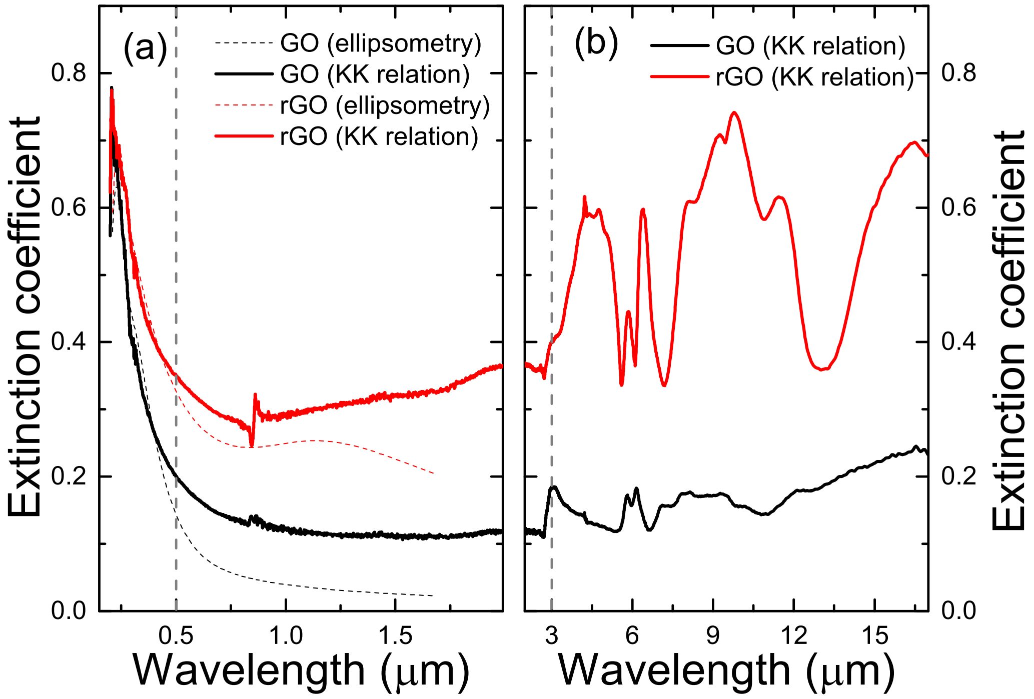

FIGURE 3.8: The deduced extinction coefficient of GO and rGO from the visible (a) to the IR (b) ranges using the reflection KK relations. The refractive index in visible range (200 nm to 1700 nm) measured by using the ellipsometer is also provided as a reference (dash line in (a)).

The extinction coefficient is used for characterising the dissipation of the EM waves in a medium and can also be calculated by using the KK relations, as plotted in Figure 3.8. Also the measured ellipsometer data of κ in the visible range have been included as a reference, which shows a good match. For both GO and rGO films, κ values demonstrate the obvious absorption in the MIR range (above 3 μm), the increasing of the absorption in the visible range especially below 500 nm and the Lorentz peak around 250 nm. Moreover, the absorption of rGO is found to be higher than GO after the laser reduction, which is due to the removing of the oxygen functional groups and hence the reducing of the bandgap.

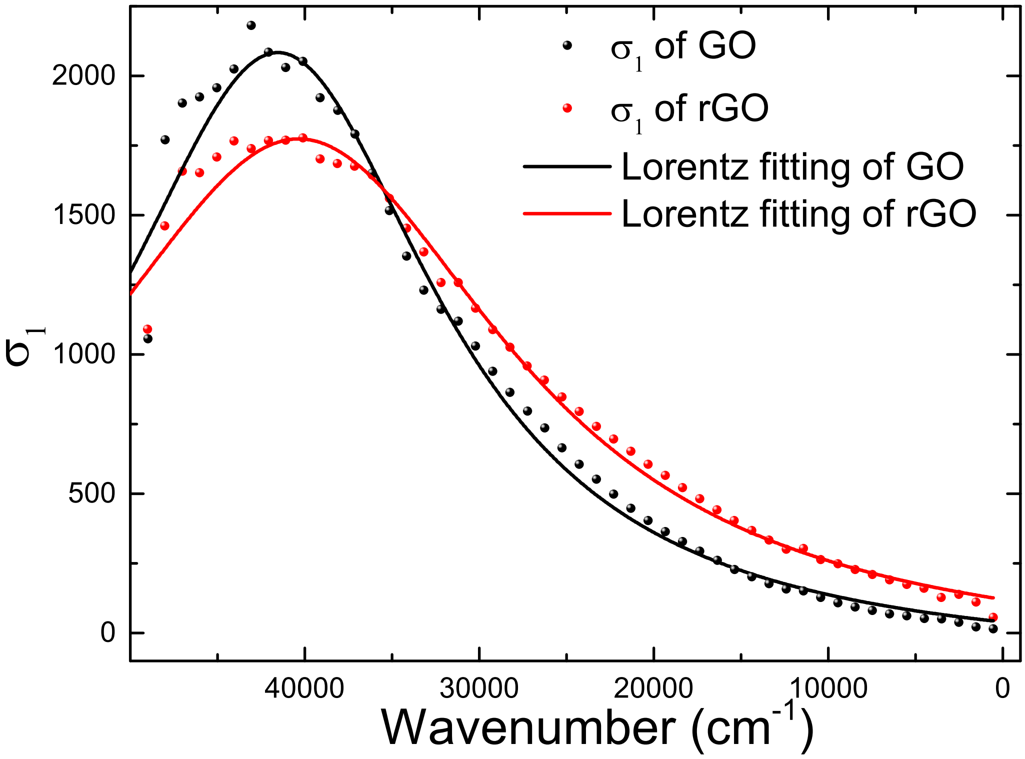

FIGURE 3.9: The real part of conductivity $\sigma_1(\omega)$ have been calculated by using the KK relations. The Lorentz fitting (solid lines) has also been used to characterise the behaviours of $\sigma_1(\omega)$.

The real part of the conductivity $\sigma_1(\omega)$ is another fundamental material parameter and has been used to understand the optical properties of solids in response to EM fields. As a result, $\sigma_1(\omega)$ of both GO and rGO films have been calculated and plotted in Figure 3.9 (black and red dots), indicating the typical Lorentz model describing the optical characteristics of many semiconductors. After fitting $\sigma_1(\omega)$ using the Lorentz model, the absorption peaks of both the GO and rGO samples can be determined by the Lorentz peak positions, which are at 41535 cm^{-1} and 40347 cm^{-1}, respectively. Therefore, the absorption peaks redshift from approximately 5.15 eV to 5.0 eV when the thick GO paper is reduced, indicating the variations of the optical bandgap (E_g) during the laser reduction process.

To determine the optical bandgap of GO and rGO films, the Tauc's formulation has been used, which can be expressed as[176]:

$$\omega^2\varepsilon_2 \sim (h\omega - E_g)^2, \tag{3.2}$$

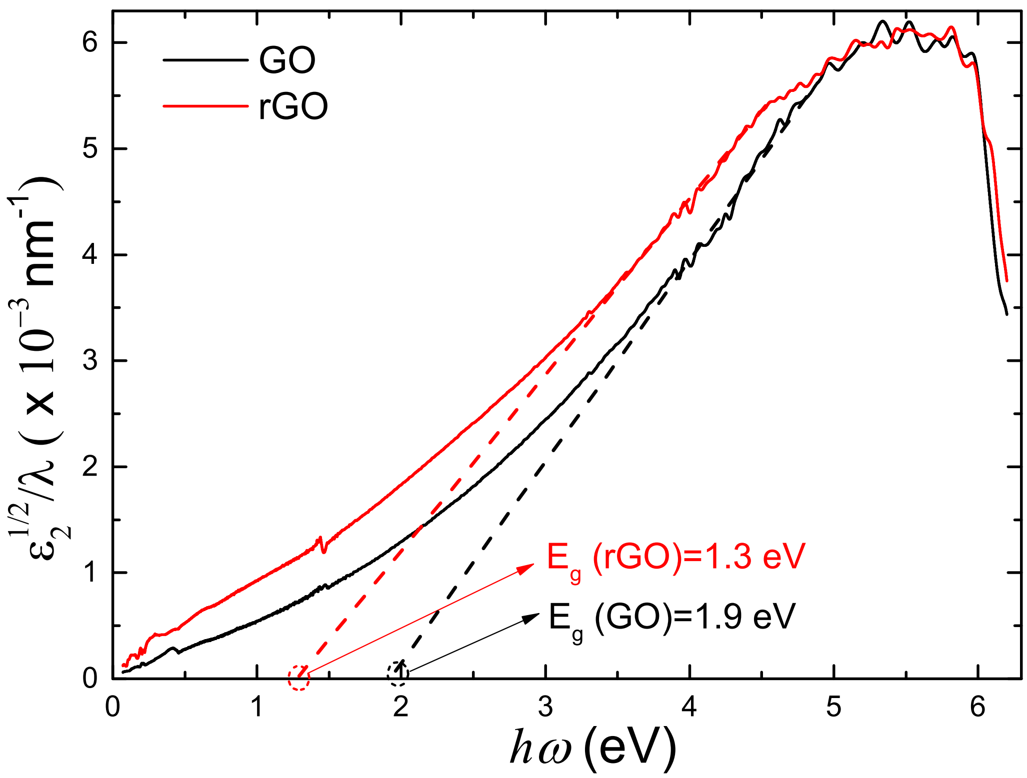

FIGURE 3.10: The plot of Tauc's formulation according to Equation 3.2. The optical bandgap can be determined by the linear extrapolations against the $h\omega$ axis, shown as the dashed line.

where ε_2 is the imaginary part of permeability, h is the Planck's constant and ω is the frequency of the incident light. According to Tauc's theory[176], the plot of $\varepsilon_2^{1/2}\omega$ as a function of $h\omega$ is a straight line. After the linear extrapolation, the intersection point with the $h\omega$ axis is the optical bandgap E_g. As a result, Figure 3.10 is the plot of Tauc's formulation for GO and rGO samples. By the linear extrapolations against the $h\omega$ axis (dashed line in Figure 3.10), the optical bandgap of GO and rGO samples are evaluated as 1.9 eV and 1.3 eV, respectively. It is reported that the bandgap of GO film is 2.8 eV and can be reduced to 0.02 eV after thermal treatment, indicating the tuning of bandgap over 2.7 eV[84]. In comparison, our results indicate the lower oxidation degree of the prepared thick GO paper with the initial bandgap of 1.9 eV. Also the tuning of bandgap is limited to 0.6 eV, indicating the incomplete reduction of the thick GO paper using laser illumination compared with the thermal treatment. Moreover, it is worth emphasising that the reflection KK method offers a versatile experimental approach to determine the dispersion relations of solid state materials over the entire spectrum due to the various available spectra characterisation methods from the UV to the microwave ranges.

3.2.3 Transmission Kramers-Kronig method

Although the optical properties of the GO and laser-induced rGO films in IR range have been demonstrated using the reflection KK method, the reduction extent is greatly limited due to the large film thickness, which is beyond the laser penetration depth. Also the optical properties of thick GO paper are different from those of single or few layer GO samples. To achieve a complete reduction of laser-induced rGO film as well as obtain the optical characteristics of thin GO sample, ultrathin GO films (~ 30 nm) have been prepared. However, the reflection KK relations can not be used due to the nonzero transmission of the ultrathin GO films. As a result, in this section, the transmission KK method has been developed to obtain the dispersion relations of both the GO and laser-induced rGO ultrathin films over the wavelength range from 200 nm to 24 μ m.

The transmission KK relations can be expressed as[177]:

$$\theta(\omega) = \frac{2\omega}{\pi} P \int_0^\infty \frac{\ln\left[t_f(\omega')\right]^{1/2}}{\omega'^2 - \omega^2} d\omega' - 2\pi\omega d \tag{3.3}$$

where t_f is the transmittance of the film only. The integration is along the contour in the ω plane and the contribution from the periphery of the circle is not zero, as in the reflection case, but equals to $2\pi\omega d$. Moreover, it is not possible to express the refractive index and extinction coefficient as simple functions of t_f and θ, as in the case of the reflection KK method (Equation 3.1). The t_f and θ have been linked to the complex refractive index in an inverse way by Heavens[178] as:

$$\begin{cases} t_f = 16(n^2 + \kappa^2)/(C^2 + D^2) \\ \theta = \arctan(\kappa C + nD)/(\kappa D - nC) \end{cases} \tag{3.4}$$

where:

$$\begin{cases} C = e^{K}\{[(1+n)(n+n_s)-\kappa^2]\cos N_0 + \kappa(1+2n+n_s)\sin N_0\} \\ \qquad + e^{-K}\{[(1-n)(n-n_s)+\kappa^2]\cos N_0 - \kappa(1-2n+n_s)\sin N_0\} \\ D = e^{K}\{[(1+n)(n+n_s)-\kappa^2]\sin N_0 - \kappa(1+2n+n_s)\cos N_0\} \\ \qquad - e^{-K}\{[(1-n)(n-n_s)+\kappa^2]\sin N_0 + \kappa(1-2n+n_s)\cos N_0\} \end{cases}$$

in which:

$$\begin{cases} K = 2\pi\kappa d/\lambda \\ N_0 = 2\pi n d/\lambda \end{cases}$$

To calculate n and κ values from t_f and θ, a computer-assisted iterative fitting process has to be performed. As a result, the procedure for transmission KK method can be summarised as measuring the film transmittance t_f, calculating the phase change θ, and finally fitting the inverse relations (Equation 3.4) iteratively.

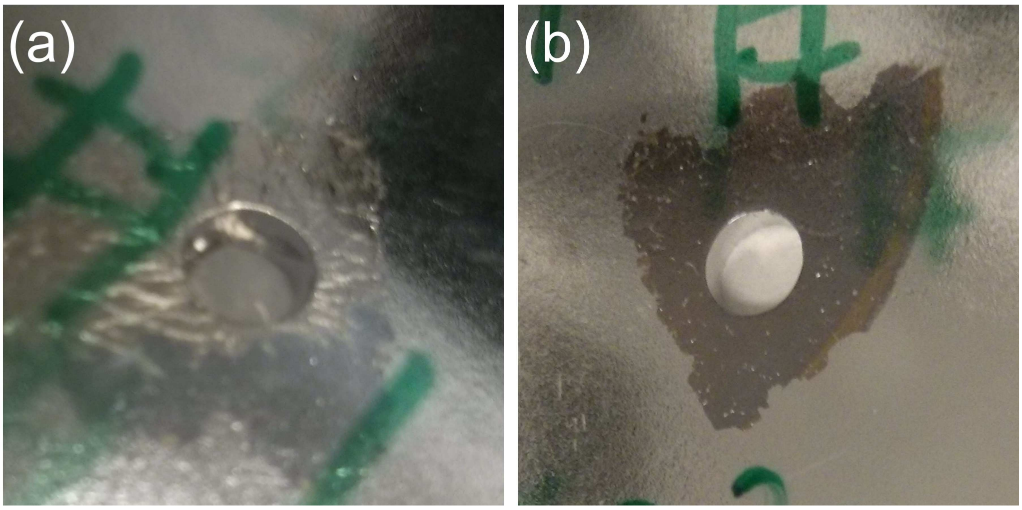

FIGURE 3.11: The free standing ultrathin GO film (∼30 nm) transferred on the sample holder before (a) and after (b) drying.

It is well known that significant deviations from the Beer's law can occur if the transmitted intensity of an incident beam of EM radiation is measured through a thin film[178]. The deviations are mainly attributed to reflection effects including multiple reflections as well as interference phenomena. Meanwhile, t_f is the absolute transmittance of the measured sample in the limit of zero film thickness. As a result, an ultrathin GO film (∼30 nm, $\ll \lambda$) has been prepared and the effects of multiple reflections can be ignored. Moreover, the use of substrate would introduce additional interfaces, resulting in the inaccuracy of the transmission spectrum. Therefore, a novel transferring technique has been used to prepare the freestanding ultrathin GO film, as shown in Figure 3.11. Firstly, the ultrathin GO film is prepared by using the vacuum filtration process with the Anodic Aluminum Oxide (AAO) membrane. Then the GO thin film can be carefully separated from the AAO membrane and float on the surface of water. A specially designed sample holder with a hole in the middle is used to get the floating GO film carefully as shown in Figure 3.11a. Finally after drying for 24 h, the high quality freestanding ultrathin GO film has been successfully attached to the sample holder (Figure 3.11b), which is ready for the spectrometer measurements.

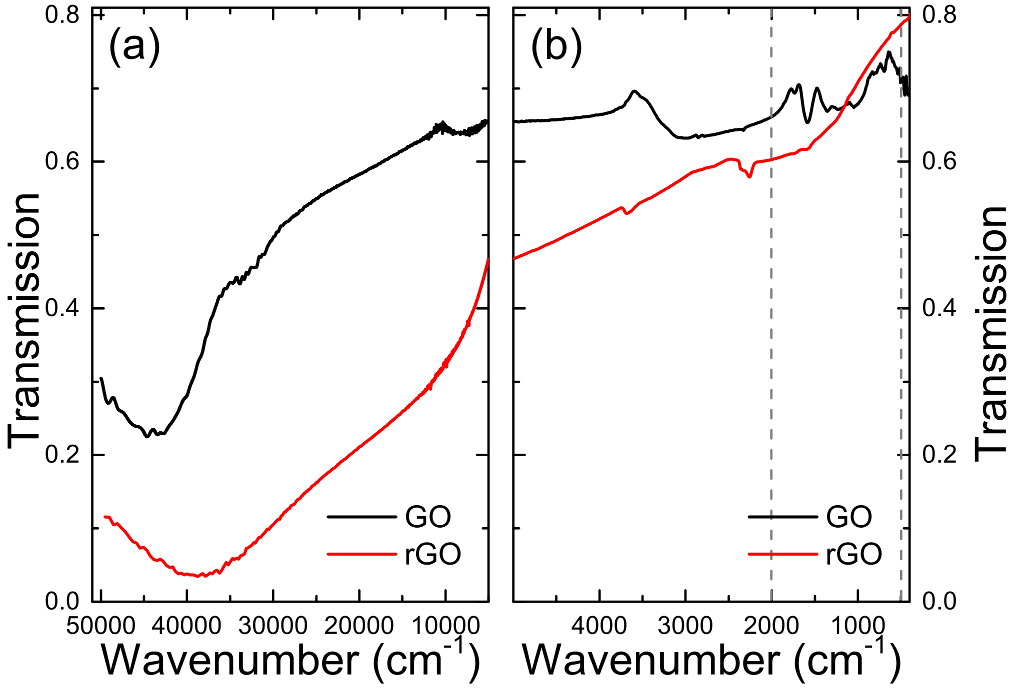

FIGURE 3.12: The transmission spectra of the GO and laser-induced rGO ultrathin films in the UV-Vis (a) and IR (b) ranges.

Figure 3.12 shows the measured transmission spectra of the GO and laser-induced rGO ultrathin films in the UV-Vis and IR ranges. Both the GO and rGO have a transmission valley around 40000 cm^{-1} due to the interband absorption (Figure 3.12a). In addition, rGO shows an overall smaller transmission and a redshift of the absorption peak due to the decreased bandgap. Meanwhile, the absorption of various oxygen functional groups has been observed in the FTIR transmission spectrum of GO from 2000 cm^{-1} to 500 cm^{-1} (Figure 3.12b). In comparison, those characteristics disappear for the transmission spectrum of rGO, indicating the removal of the oxygen functional groups. Compared with the laser reduction of thick GO paper used in the reflection KK method, an almost complete reduction is expected for the ultrathin GO film.

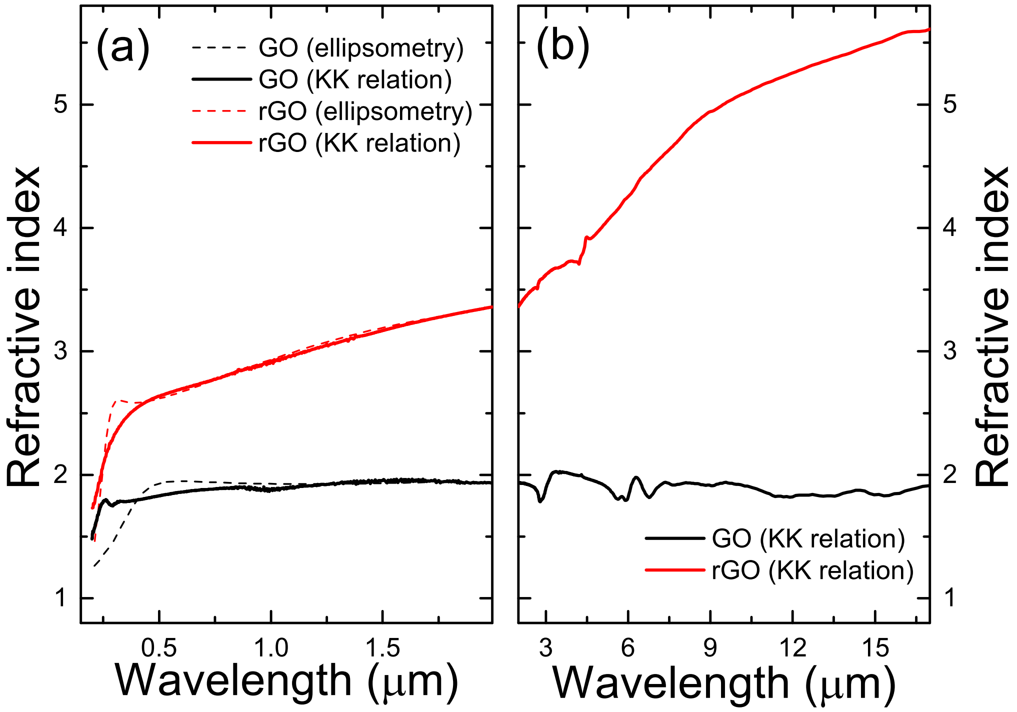

FIGURE 3.13: The calculated refractive index of the GO and laser-induced rGO ultrathin films in the UV-Vis (a) and IR (b) range.

The transmission KK relation has been used to calculate the phase change θ on the transmission according to Equation 3.3. Then the refractive indices of the GO and laser-induced rGO ultrathin films can be deduced by solving Equation 3.4 iteratively until the convergence of the n, κ values. Figure 3.13 is the calculated refractive indices of GO and rGO in the UV-Vis and IR ranges. The ellipsometer measured data have also been provided as a reference and a good match has been observed (Figure 3.13a), which proves the accuracy of the transmission KK method for the ultrathin GO and rGO films. Moreover, the refractive index of rGO is found to increase more than 0.5 in the UV-Vis range (Figure 3.13a) and even reaches 5.5 in the IR range (Figure 3.13b), which illustrates the high reduction extent and may serve as the potential high index material for various diffractive optical elements in the IR range given the low absorption.

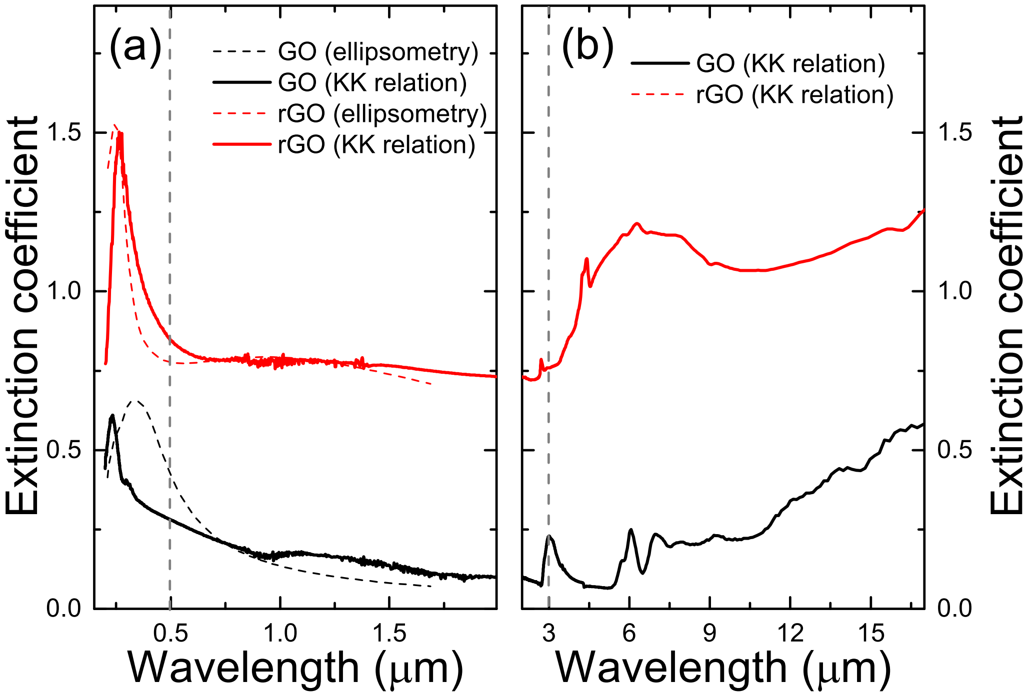

FIGURE 3.14: The deduced extinction coefficient of the GO and laser-induced rGO ultrathin films in the UV-Vis (a) and IR (b) ranges using the transmission KK method. The extinction coefficient in visible range (200 nm to 1700 nm) measured by using an ellipsometer is also provided as a reference (a).

The extinction coefficient is also calculated by using the transmission KK relations, as plotted in Figure 3.14. Also the measured ellipsometer data of κ in the visible range have been included as a reference, which shows a good match. For both GO and rGO ultrathin films, κ values demonstrate the obvious absorption in the MIR range (above 3 μm), the increasing of the absorption in the visible range especially below 500 nm and the Lorentz peak around 250 nm. Moreover, the absorption of the laser-induced rGO ultrathin films is found to be higher than rGO paper (Figure 3.8b), which is due to the higher reduction extent.

The real part of conductivity $\sigma_1(\omega)$ has also been calculated based on the relations between optical constants listed in Table 3.1, as shown in Figure 3.15. Again the typical Lorentz model has been used to fit the conductivity. The Lorentz absorption peaks of both the GO and rGO thin films have been observed at 5.5 eV and 4.7 eV in the transmission KK method, indicating a larger oxidation degree of the ultrathin GO film and the better bandgap tailoring capability compared with the thick GO paper (Figure 3.9).

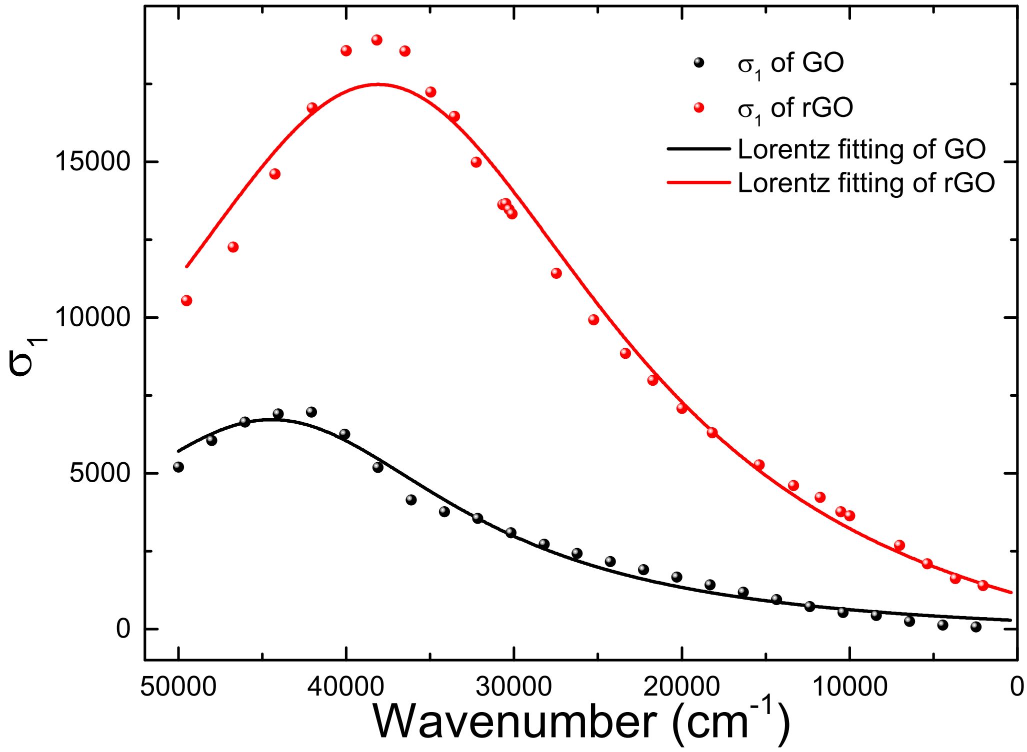

FIGURE 3.15: The real parts of conductivity $\sigma_1(\omega)$ for the GO and rGO ultrathin films have been calculated by using the KK relations. The Lorentz fitting (solid lines) has also been used to characterise the behaviours of $\sigma_1(\omega)$.

The optical bandgap of the ultrathin GO and rGO films have been determined by using the Tauc's formulation[176], as shown in Figure 3.16. It can be seen clearly that the optical bandgap of the ultrathin GO film is 2.7 eV and has been reduced to 0.78 eV after the laser reduction. Compared with the thick GO paper, the initial bandgap of the ultrathin GO film is 0.8 eV larger, which is possibly due to the less interlayer interactions. Also the tuning of the bandgap is found to be 1.92 eV for the ultrathin GO film after the laser reduction, around 3 times larger compared with that of the bulk rGO sample (0.6 eV), which is comparable with the bandgap tuning capability of the widely used thermal reduction method. Therefore, the laser reduction of the ultrathin GO films offers not only the flexible manufacturing ability, but also the large bandgap tailoring capability, which would be greatly used for all-GO based functional devices.

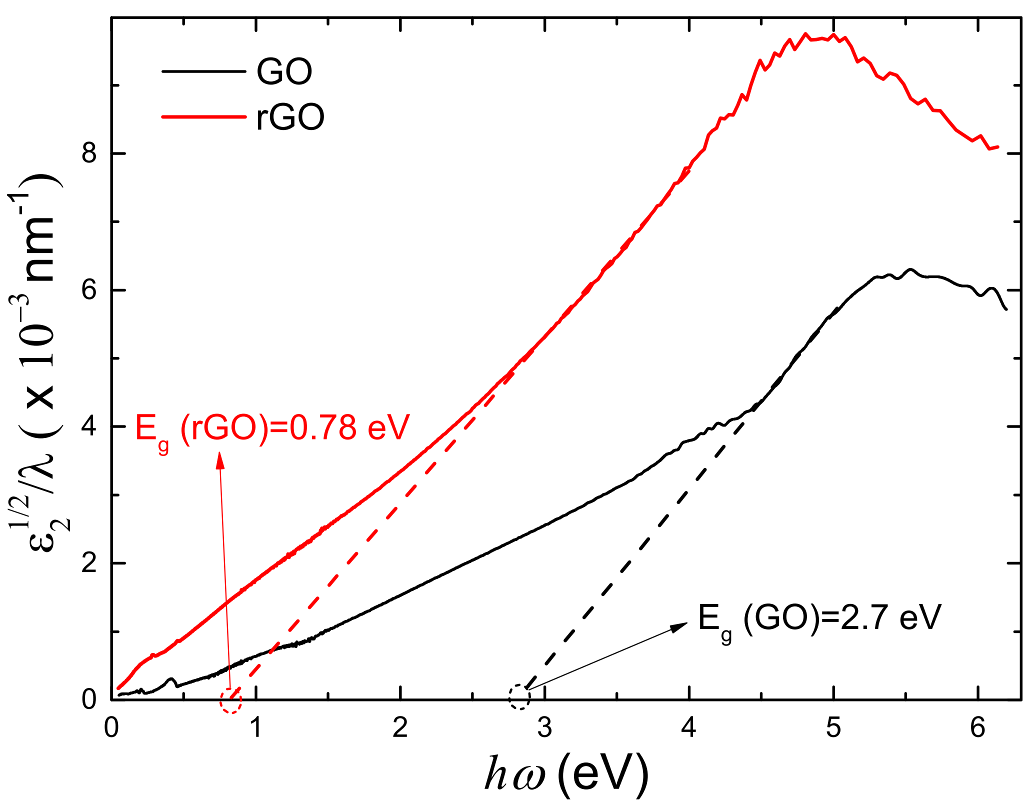

Figure 3.16: The plot of Tauc's formulation according to Equation 3.2. The optical bandgap can be determined by the linear extrapolations against the $h\omega$ axis, shown as the dashed line.

3.2.4 Conclusions

In conclusion, the KK relations have been successfully further developed and adopted to investigate the optical parameters of both GO and laser-induced rGO films over the broadband range from UV to IR range. Both reflection KK method and transmission KK method have been used based on the optical properties of the GO and rGO samples. Also the measured ellipsometer data have been provided as a reference and good matches have been observed for both refractive index and extinction coefficient, further validating the effectiveness of the two KK methods for ultrathin 2D materials. Lorentz model has been employed to characterise the optical behaviours in the visible range. The tuning of the optical bandgap of rGO compared to that of GO has been evaluated. The fundamental dispersion relations of the GO and laser-induced rGO films have been extended to the MIR range for the first time. The missing optical information of GO and rGO in the IR range is of great importance not only for the understanding of the conductivity theory of the materials, but also for the various IR applications in photodetecting, biomedical imaging and sensing, aerospace science and defences.

The successful adapting of the KK relations, in particular the transmission KK method, in characterising the ultrathin GO and rGO films opens up a novel avenue for optical property characterisations of 2D materials with atomic-scale thicknesses, which are inaccessible to the traditional spectroscope ellipsometry method. Moreover, the attainable frequency range can be greatly extended by combining various spectroscopic methods from the UV to microwave ranges, offering the optical properties over nearly the full spectrum. Furthermore, by simply performing the single spectrum measurement, either transmission or reflection, all of the optical parameters can be determined with high accuracies, which greatly promote the design and fabrication of functional integrated photonic devices based 2D materials.

Chapter 4

Nonlinear optical properties of graphene oxide

In addition to the linear optical properties discussed in Chapter 3, the optical nonlinearities are of great importance for high performance all-optical photonic devices. In particular, nonlinear optical absorption has been proved useful for a number of applications including OL to protect sensitive instruments from laser-induced damage, and SA for pulse compression, mode-locking and Q-switching[179]. On the other hand, the NLR (Kerr effect) is crucial for functionalities including all-optical switching, signal regeneration and fast optical communications[106]. However, as reviewed in Chapter 2, the research on nonlinearities of GO is largely limited to the nonlinear absorption of GO solutions, and the nonlinear activities during the process of the laser-induced reduction from GO to rGO films have remained unexplored, which are the key for realising the functionality in the patterned GO integratable optoelectronic devices.

In this chapter, the third-order optical nonlinearities of the GO and laser-induced rGO thin films have been investigated by using the Z-scan techniques. Both the nonlinear absorption and NLR are tunable during the laser-induced reduction process. Moreover, the enhanced nonlinearity has also been demonstrated by the successful functionalisation of the GO films with AuNPs.

4.1 Tunable nonlinearities of graphene oxide

In this section, we investigate the in-situ nonlinear activities of the chemically synthesised GO films (Figure 4.1) during their entire laser-induced reduction process through continuous increase of the laser irradiance until the optical breakdown. Most importantly, four stages of different nonlinear activities have been discovered with increased laser irradiance. Both the tuning of the nonlinear absorption response and a switch of the sign for the nonlinear refractive index are observed during the transition from GO to rGO. Meanwhile, the giant Kerr nonlinear responses are observed to be three orders of magnitude larger than those in the previous reports, leading to a giant nonlinear figure of merit (FOM) crucial for functional nonlinear device design. Our results have not only explored the rich nonlinear responses of the GO films during its reduction to the rGO films, but also demonstrated the tunability of the nonlinear properties, in particular n_2, of GO films for highly integrated nonlinear photonic applications on a thin film.

The high quality GO solutions (Figure 4.1a) are synthesised by the chemical reduction of graphite via a modified Hummers method[180]. Firstly, graphite and $NaNO_3$ are mixed with concentrated H_2SO_4. By vigorous stirring, the reducing agent $KMnO_4$ is added into the suspension. Then H_2O_2 is added into the mixture at 98 °C. The product is washed and dried, and then the GO sheets are obtained after the purification. A deionised water/methanol mixture with an optimal ratio of 1:5 is used to disperse GO the flakes. The high quality continuous GO thin films (See inset of Figure 4.1c) with controlled thicknesses are obtained through a spin coating process (Figure 4.1b) on a cover glass. Figure 4.1c presents the optical microscope image of the as-prepared GO thin films over a large scale.

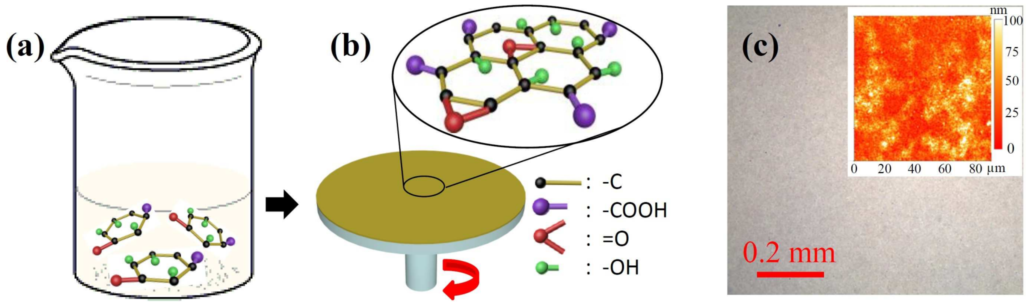

FIGURE 4.1: (a) GO solution synthesised by a self-assembly method. (b) Schematic figure of spin coating process. Inset: schematic atomic structure of the GO film with hydroxyl groups (green binding), epoxide groups (red binding) and carboxylic groups (purple binding). (c) Optical microscope image of the as-prepared GO thin film over a large area. Inset: The surface morphology of the GO layer has been characterised by using 3D optical profiler (Bruker ContourGT-I). The topographic image clearly shows that a continuous film with a surface roughness of less than 100 nm has been achieved for a 90×90 μm^2 area of the GO layer.

4.1.1 Nonlinear absorption of graphene oxide

The nonlinear absorption responses of the GO thin film through its entire reduction process are characterised by using the excitation fluence dependent open-aperture Z-scan measurement using a femtosecond laser with a central wavelength of 800 nm and a pulse duration of $\sim$ 100 fs. The laser beam is spatially filtered and focused onto the film, with a beam waist of $\sim 2.5\ \mu m$. A neutral density filter is employed to vary the input laser fluence continuously. The output fluence F_{out} versus input fluence F_{in} ranging from 0.03 to 57.3 $\mu J/cm^2$ (optical breakdown) is plotted in Figure 4.2a. The linear transmittance T of the GO film, given by the F_{out}/F_{in} ratio, is found to be 11.2% and is shown as a reference. At an ultra-low input fluence under 15.9 $\mu J/cm^2$ (red squares in Figure 4.2a) the F_{out}/F_{in} slightly exceeds the linear transmission, indicating that the SA occurs in the GO film. An open aperture Z-scan curve at F_{in}=4.5 $\mu J/cm^2$ (Figure 4.2b) indeed shows the SA behaviour.

Increasing the input fluence from 15.9 to 32 $\mu J/cm^2$ (green circles in Figure 4.2a) leads to a decrease of the F_{out}/F_{in} ratio to be below than the linear transmission T. It means that the OL effect becomes dominant in this region. The open aperture curve at F_{in}=25 $\mu J/cm^2$ (Figure 4.2c) clearly shows the OL

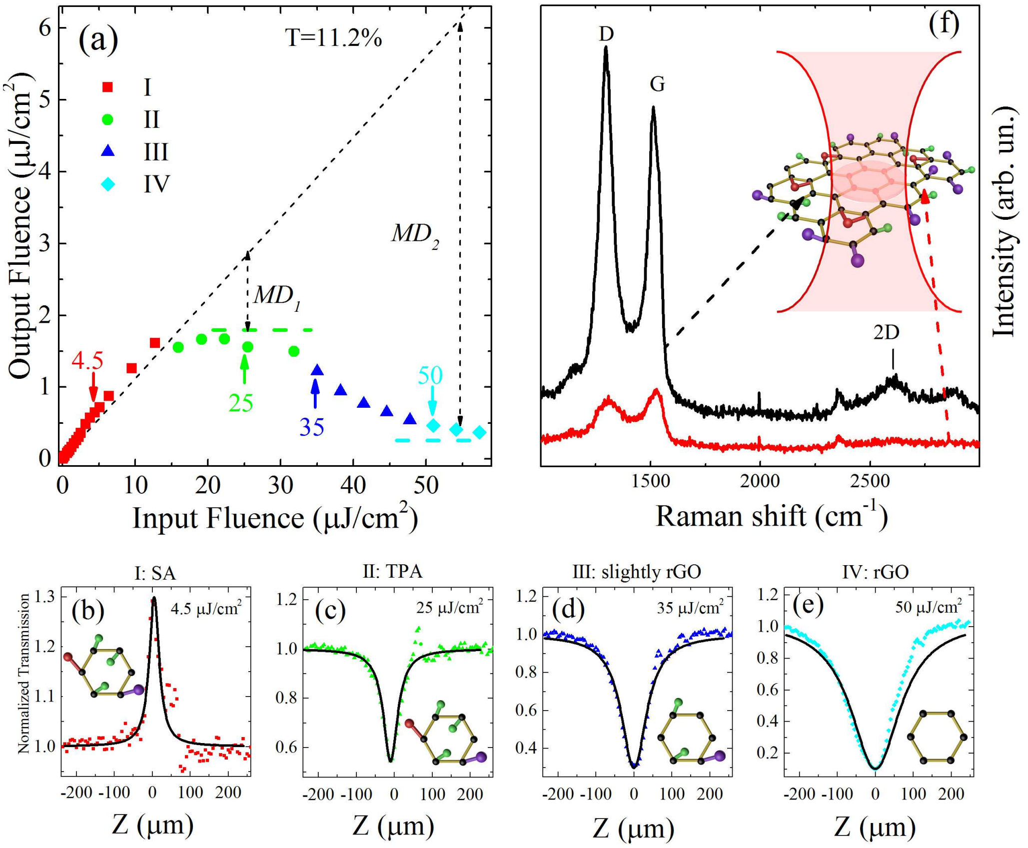

Figure 4.2: (a) Plot of output versus input fluence (scatters). Four different stages (I, II, III and IV) are labeled. T is the linear transmittance (black dash line). MD_1 and MD_2 represent the modulation depth in Stages II and IV, respectively. (b-e) Power dependent open aperture Z-scan results (scatters) fitted with the theory (black solid lines). Inset: schematic atomic structure of GO films. (f) Raman spectra of GO and fully reduced GO films. Inset: schematic figure of laser-induced reduction.

property. From the slope dF_{out}/dF_{in}, as indicated by the coloured dashed line in Figure 4.2a, the limiting differential transmittance can be determined[181]. The almost constant slope of the green dashed line at the input fluence from 15.9 to 32 μJ/cm^2 suggests that a modulation depth (MD) of approximately 50% can be achieved, which outperforms over the nanostructured plasmonic medium in a gold thin film[106]. The above mentioned transition from SA to OL is similar to the previous observations[98,99], however our results are achieved with much reduced (three orders of magnitude) fluence. In addition, the transition from saturable absorption to reverse saturable absorption has also been observed in multi-walled carbon nanotube-doped sol-gel hybrid glasses.In addition, the transition from SA to RSA has also been observed in multi-walled carbon nanotube-doped sol-gel hybrid glasses, which is the first demonstration of a temporal transition between SA and RSA in carbon nanotube-doped matrices[182].

When further increasing the laser fluence from 32 to 50 μJ/cm^2 (blue triangles in Figure 4.2a), interesting nonlinear responses, which have never been reported before, start to occur. The F_{out} value keeps decreasing and the slope of dF_{out}/dF_{in} becomes negative. The nonlinear absorption curve measured at F_{in}=35 μJ/cm^2 (Figure 4.2d) clearly shows a broadening effect, indicating the reduction of the GO starts to occur. Indeed it is found that the nonlinear absorption behaviour is no longer reversible when $F_{in} >$32 μJ/cm^2, suggesting a threshold fluence is reached for the commencement of the reduction.

The slope of dF_{out}/dF_{in} eventually approaches to another constant when $F_{in} >$50 μJ/cm^2 as shown by the cyan diamonds in Figure 4.2a due to the full reduction of the GO film. In this case, OL is still dominant but the curve is further broadened as shown in Figure 4.2e and measured at F_{in}= 50 μJ/cm^2. A MD more than 90% can be achieved in this case, which is again much higher than those reported so far.

From the above mentioned analysis, the nonlinear absorption behaviour of the thin film in the reduction process from GO to rGO can be divided into four different stages as indicated by the four different coloured regions in Figure 4.2a. In Stage I ($F_{in} <$15.9 μJ/cm^2), SA is observed from the GO thin film due to the ground-state bleaching of the sp^2 domain[99,101]. Specifically, the sp^2 domain has a narrow energy gap of $\sim$ 0.5 eV[69], and the optical absorption of electrons can be easily saturable, which results in the depletion of the valence band and filling of the conduction band. In Stage II (15.9 μJ/cm$^2 <$ $F_{in} <$32 μJ/cm^2), the TPA and ESA of the sp^3 matrix are responsible mechanisms for the observed OL[101]. The TPA is due to the electron transition from the ground state to the excited state in the sp^3 matrix. Neither SA in Stage I nor OL in Stage II is attributed to the loss of the oxygen functional groups, as shown in the insets of Figures4.2b,c. The oxygen functional group starts to decrease with the reduction of the GO film in Stage III (32 μJ/cm^2 $< F_{in} <$ 50 μJ/cm^2, inset of Figure 4.2d) and fully rGO with no oxygen functional group can be achieved eventually in Stage IV ($F_{in} >$ 50 μJ/cm^2, inset of Figure 4.2e), as confirmed from the Raman measurement shown in Figure 4.2f. Before the laser irradiation (red solid line in Figure 4.2f), the GO film contains the D-band (1339 cm^{-1}) and the G-band (1585 cm^{-1}). After the laser treatment (black solid line in Figure 4.2f), the 2D-band (2662 cm^{-1}) can be observed, indicating the formation of rGO. Meanwhile, the relative intensity of the D-band grows faster than that of the G-band and both D and G bands experience obvious narrowing. These are the typical indications for the transition from GO to rGO[183].

Carbon-based nano-materials OL effect has been extensively studied. Compared with the carbon-based nano-materials[184], the mechanism of OL effect of the GO thin film is different. The primary mechanism of carbon-based nano-materials for the OL effect is NS, which is due to the formation of solvent microbubbles at high excitation intensities as a consequence of energy transfer from the dispersed material to the solvent. The slow formation of microbubbles limits the OL effect of carbon-based nano-materials mostly within the nanosecond regime, whereas NS for ultrashort laser pulses (femtosecond or picosecond) is usually much weaker than that for the nanosecond laser pulses[99]. However, the OL mechanisms of the GO thin film are multiphoton absorption and ESA, which exist in the nanosecond, picosecond, and femtosecond regimes. In particular, multiphoton absorption dominates the nonlinear absorption process in ultrashort laser pulse excitation (femtosecond in this case), whereas ESA plays an important role in the case of nanosecond pulses[98].

4.1.2 Nonlinear refraction of graphene oxide

In Figure 4.3, the NLR of the GO thin film is measured by using the close aperture Z-scan method according to the four identified stages. The nonlinear absorption of GO film arising from the sp^2 domain and sp^3 matrix predicts rich NLR of the GO film. In Stage I (Figure 4.3a), a pronounced valley-peak pattern is observed under ultralow laser fluence (4.5 μJ/cm^2), indicating a large positive nonlinear refractive index n_2 (self-focusing) for the GO films. The observed NLR at this stage is mainly attributed to the population redistribution of the π electrons and the free carriers of the sp^2 domain as well as the bound electrons and free carriers of the sp^3 matrix[101,108]. As the input fluence increases in Stage II (Figure 4.3b), although the sign of n_2 is maintained, the magnitude of the valley-peak pattern starts to reduce and a transition from valley-peak to peak-valley configuration (self-defocusing) begins to occur gradually. Starting from 32 μJ/cm^2, the transition of the sign of n_2 becomes obvious, confirming perfectly the commencement of the reduction from GO to rGO. In this stage, the sp^2/sp^3 ratio increases due to the reduction of the oxygen functional groups. Therefore, the transition from self-focusing to self-defocusing is attributed to the different NLR responses of the GO and rGO. However, this transition state makes it difficult to fit with a typical NLR pattern (shown in Figure 4.3c). Eventually at Stage IV, the sign of the NLR curve is changed completely to negative as shown in Figure 4.3d, which is consistent with the previously reported NLR property of graphene[185], further confirming the reduction of the GO thin film to rGO when F_{in} >50 μJ/cm^2.

4.1.3 Nonlinear coefficients of graphene oxide

To further elucidate the magnitude of the nonlinear responses of the GO thin film during the four stages, both the nonlinear refractive index n_2 and the nonlinear absorption coefficient β are deduced by fitting the close aperture and open aperture Z-scan curves obtained at the four stages, as presented in Figure 4.4a. It is worth mentioning that the variations of the GO film absorbance, thickness and linear refractive index have been carefully characterised and taken into account when fitting the Z-scan curves. The absorbance of the GO film is highly dependent on the film thickness. And the Beer-Lawbert Law is used for the determination of absorption coefficient. Both n_2 and β exhibit large tuning ranges over the four stages during the entire reduction process. n_2 is positive before the reduction. Its value is slightly reduced in Stage I and remains almost constant in Stage II,

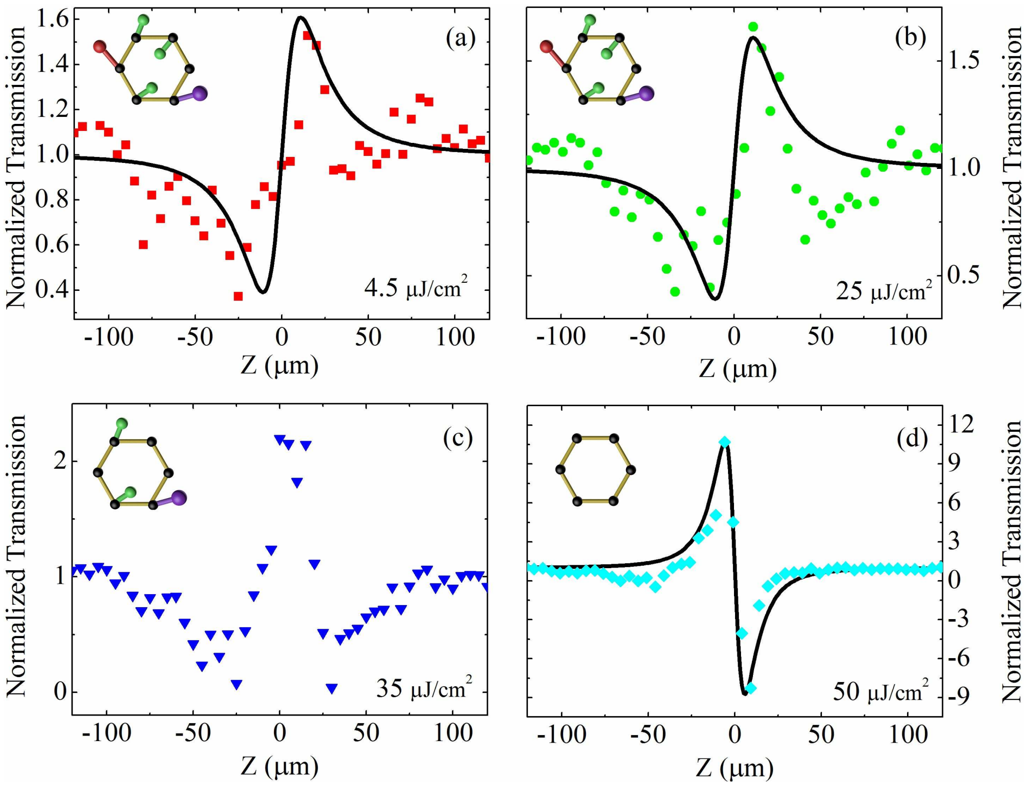

FIGURE 4.3: Close aperture Z-scan curves (scatters) under (a) 4.5 μJ/cm^2, (b) 25 μJ/cm^2, (c) 35 μJ/cm^2 and (d) 50 μJ/cm^2 fitted with the theory (black solid lines). Inset: schematic atomic structure of GO films in the four stages, respectively.

arising from the intrinsic third-order nonlinear optical response of GO film before the reduction[108]. A switch of the sign from positive to negative takes place in Stage III, corresponding to the reduction from GO to rGO. The achievable negative n_2 of rGO in Stage IV is found to be as large as 10^{-9} cm^2/W, the same order of magnitude for graphene reported recently[185,186], indicating the removal of oxygen functional groups within the GO film.

On the other hand, β is found to increase with the input fluence in Stage II where no reduction happens. Hence, the intensity dependent nonlinear absorption coefficient predicts the multiple mechanisms for OL in Stage II, such as the TPA as well as the ESA[108]. To evaluate the OL ability of our GO thin film, β is deduced to be 40000 cm/GW at 32 μJ/cm^2, which is 1000 times higher than the previously reported results at 800 nm[99]. The giant nonlinear absorption can be attributed to the comparatively large thickness of our GO film ($\sim$ 2 μm), in which localised sp^2 domain increases with smaller sp^3 matrix located mostly around the edges of the GO film[99]. The variation of β in Stages III and IV, however, is attributed to the reduction of GO film.

It should be noted that the comparatively large film thickness is used to allow us to observe the dynamic change of the four stages in the NLR without damaging the film. The OL property has been observed in varied GO film thicknesses from 100 nm to a few micrometers. For the OL application, a thin GO film (around 100 nm thick) with a linear transmittance of 89.8% can be achieved (result not shown).

The fact that both n_2 and β can be tuned over large dynamic ranges with controllable laser fluence offers great flexibility in designing highly integrated functional all-optical devices with desired third-order nonlinear properties. To this end, the nonlinear FOM is evaluated for the thin film at different stages of the laser-induced reduction process, as shown in Figure 4.4b. Since the definition of FOM is based on the TPA, in Stage I, where SA is dominant, the conventional nonlinear FOM is not calculated here. It can be seen clearly that the FOM of the thin film remains at a high level over the entire reduction process. In particular, the rGO film possesses a FOM of 4.56, which is 7 times higher than that for the silicon on insulator structure[187], a known structure with a high FOM, offering unprecedented potential for wide range highly integrated photonics applications.

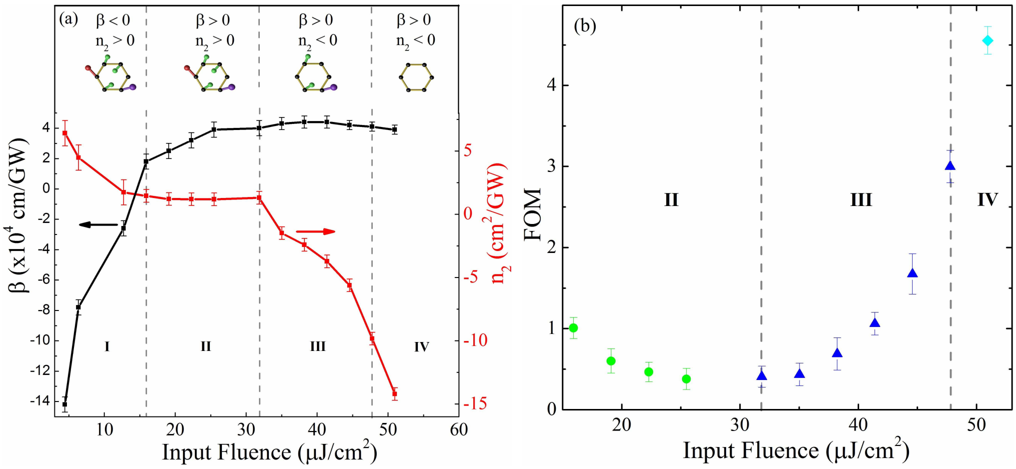

FIGURE 4.4: (a) Plot of NLR index n_2 and nonlinear absorption coefficient β versus the input fluence. Nonlinear activities as well as atomic structure of GO film in the four different stages (I, II, III and IV) are summarised. (b) Nonlinear FOM in Stages II, III and IV.

4.1.4 Conclusions

In this section, we have developed a high quality continuous GO thin film by using a self-assembly method. Rich and giant nonlinear responses of the GO film during its entire reduction process are unveiled by using the Z-scan measurement. Both the transition of the nonlinear absorption response from SA to OL and nonlinear refractive index from positive to negative have been observed at different input fluences. Four unique stages have been distinguished, corresponding to the entire reduction process of the GO film. Our results show that the third-order nonlinear responses of the GO film can be dynamically tuned by varying the laser input fluence. The GO thin film with tunable nonlinear response and a versatile patterning capability by DLW, may serve as a promising solid state material for novel nonlinear functional devices.

4.2 Enhanced nonlinearity of hybrid graphene oxide composite

In this section, we propose and demonstrate a flexible method to functionalise highly transparent GO film with AuNPs. The solid-state hybrid GO-AuNP films at different AuNP concentrations have been synthesised through a vacuum filtration process[47]. Significantly enhanced nonlinear absorption and NLR behaviors of the hybrid GO-AuNP films are characterised by the Z-scan measurement, which are tunable by changing the AuNP concentrations. Both the nonlinear absorption and refractive coefficients have also been retrieved by fitting the open-aperture and close-aperture Z-scan curves.

4.2.1 Hybridisation of graphene oxide with gold nanoparticles

In order to achieve highly uniform distribution of AuNPs inside the GO films, homogeneous GO and AuNP water solutions are mixed together. The concentration of GO in GO solution is 1.4 mg/ml and the concentration of AuNP in AuNP solution is 0.1% by weight. The hybrid GO-AuNP films can be obtained through the vacuum filtration method on the AAO membrane[47]. Then the hybrid GO-AuNP films are carefully peeled off as free-standing films so that they can be easily attached to any desired substrates. In our experiment, three hybrid GO-AuNP films with increased AuNP concentrations have been prepared and labelled as GO-AuNPs1, GO-AuNPs2 and GO-AuNPs3, respectively. The film thicknesses are kept the same at ~ 1 μm. The ratio of AuNP concentration in the three hybrid films is specifically fixed as 1:2:4 (as listed in Table 4.1) to ensure a comparable linear absorption at the measured wavelength of 800 nm. A pure GO film with the same GO quantity is prepared and used as a reference sample throughout the experimental characterisation. The AuNP-only sample with the highest AuNP concentration as that used in the GO-AuNPs3 sample has also been measured as a reference.

Table 4.1: The mixing of GO solution and AuNP solution in the hybrid films

GO film	GO-AuNPs1	GO-AuNPs2	GO-AuNPs3
2 ml GO solution	2 ml GO and 0.5 ml AuNP	2 ml GO and 1 ml AuNP	2 ml GO and 2 ml AuNP

To confirm the effective functionalisation of GO with AuNPs through the vacuum filtration method, we measure the UV-Vis absorption spectra of the three hybrid GO-AuNP films and compare them with the spectrum of the reference GO sample, as shown in Figure 4.5a. For the absorption spectrum of the GO film, significant absorption below 400 nm can be observed. The characteristic shoulder at 305 nm is attributed to the n$\rightarrow \pi^*$ transitions of the C=O bonds[188]. Clearly, the measured smooth UV-Vis spectrum and the characteristic absorptions of the

GO film suggest both the purity of our GO solutions and high quality of the GO film made by the vacuum filtration method.

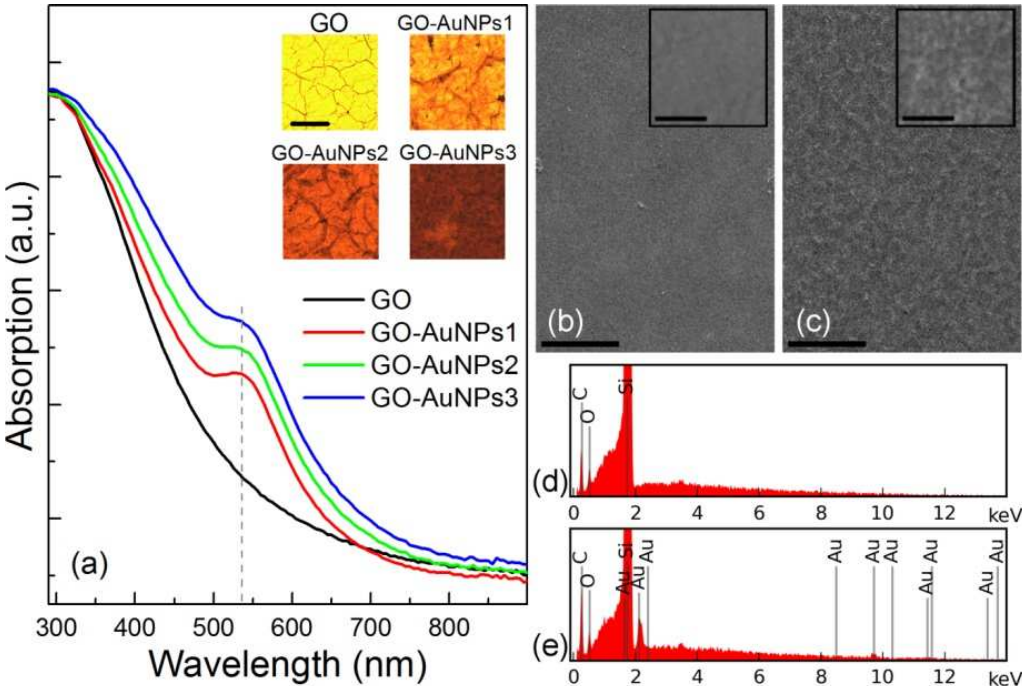

FIGURE 4.5: (a) UV-Vis absorption spectra of the GO, GO-AuNPs1, GO-AuNPs2 and GO-AuNPs3 films. Inset: the microscopic images of the four films. Scale bar, 20 μm. (b) and (c) SEM images of the pure GO film in comparison with the GO-AuNPs3 film. Scale bars, 20 μm. Inset: enlarged views. Scale bars, 500 nm. (d) and (e) EDX images of the pure GO film in comparison with the GO-AuNPs3 film, which clearly show the presents of AuNPs in the GO-AuNPs3 film.

In comparison, the absorption spectra of the hybrid GO-AuNP films show similar behaviors as that of the reference GO film except for the strong absorption peaks at around 535 nm (dashed grey line in Figure 4.5a), which can be attributed to the localised surface plasmon resonance of AuNPs (~60 nm in diameter). The strong absorption peaks also imply the high density of loaded AuNPs and a significant interaction between AuNPs and GO. Moreover, the absorption peaks are strongly dependent on the AuNP concentration, in particular, monotonically increasing with the concentration of AuNPs. The microscopic images of the four films are shown in the inset of Figure 4.5a. It can be seen clearly that the color varies from brown to red as the AuNP concentration increases, which is consistent with the absorption spectra. It should be emphasised that the linear absorptions of the four samples at 800 nm are reasonably low (less than 20%) and they are kept nearly the same by carefully adjusting the ratio of AuNP concentration in the three hybrid films (1:2:4) so that the optical nonlinearities of the four samples can be compared directly.

To examine the morphology of the hybrid GO-AuNPs films, SEM images are obtained for the pure GO film in comparison with the GO-AuNPs3 film (the highest AuNP loading case), as presented in Figures 4.5b,c. It can be clearly seen from both the SEM image and the Energy-dispersive X-ray spectroscopic (EDX) image (Figures 4.5d,e) that the AuNPs are presenting in the GO-AuNPs3 film and they distribute evenly over the entire GO film. No aggregation has been observed, indicating the high quality of the hybrid GO-AuNP films.

4.2.2 Nonlinear absorption of hybrid GO films

The optical nonlinearities of the GO and hybrid GO-AuNP films are studied by the Z-scan measurement, and the result of AuNP-only sample is also provided as a reference. The open-aperture Z-scan curves at the same input fluence are shown in Figure 4.6a. All of the four films present the OL property whereas no OL effect can be observed in the AuNP-only sample. The OL of GO is due to both ESA of the sp^3 matrix and the multiphoton absorption when electrons transit from the ground state to the excited state in the sp^3 matrix[101]. The OL ability, evidenced by the achievable minimal transmittance, has been greatly enhanced as the increase of the AuNP concentration.

Theoretical fittings of the open-aperture results are shown as the solid lines in Figure 4.6a. To further understand the entire nonlinear absorption behaviors, the excitation-fluence dependent open-aperture Z-scan measurement is conducted. The output fluence (F_{out}) versus input fluence (F_{in}) for the four films is plotted in Figure 4.6b. High linear transmittance T (∼80%) of the four films at 800 nm has been achieved and is plotted as a reference. The four films present similar nonlinear absorption behaviors. Firstly, at the small input fluences, the F_{out} $/F_{in}$ ratio is the same as T, indicating the samples show only the linear

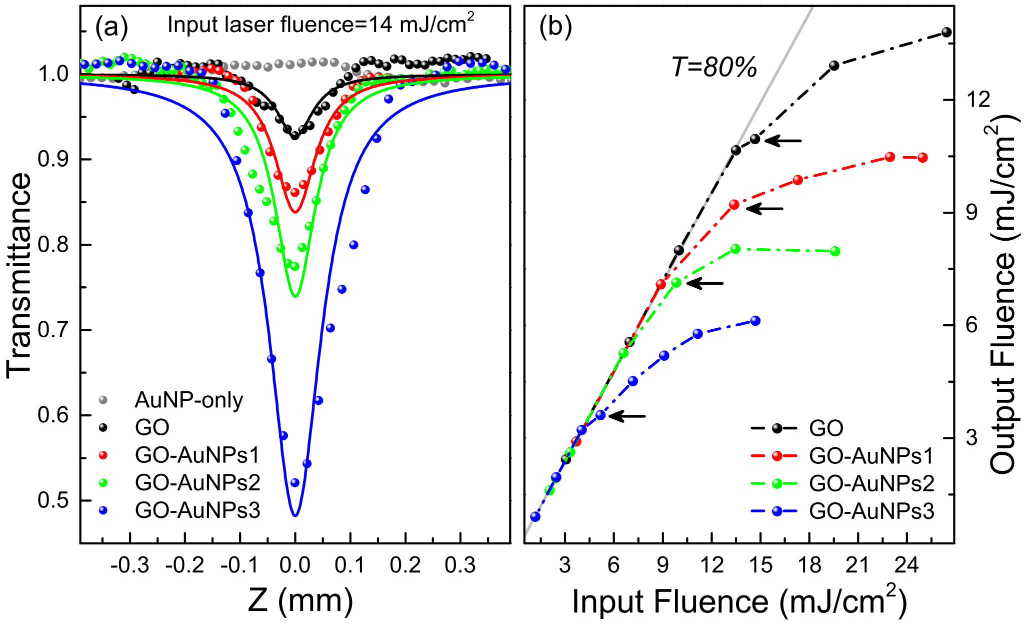

FIGURE 4.6: (a) Open aperture Z-scan results (scatters) of the AuNP-only, GO, GO-AuNPs1, GO-AuNPs2 and GO-AuNPs3 samples at the same input fluence (14 mJ/cm^2). The theoretical fittings are indicated as the solid lines. (b) Plot of output fluence versus input fluence for the four films. T represents the linear transmittance (grey solid line). The arrows show the OL onsets of the four films, respectively.

absorption. As the input fluence increases, F_{out} $/F_{in}$ starts to reduce and becomes smaller than T, representing the onset of the OL behavior. Finally, the saturation of the OL is reached at the large input fluence and no further reduction of F_{out} $/F_{in}$ can be achieved. Therefore, all the four samples exhibit the characteristic OL behaviors under various input fluences. However, there are differences among the four curves. First of all, the OL onsets (defined as the input fluence at which the transmittance starts to depart from T) are monotonically reduced as the concentration of AuNP increases (see arrows in Figure 4.6b). The input fluences, at which the OL saturates, are also found to be monotonically dependent on the concentration of AuNP. As a result, it is evidently proved that the enhanced nonlinear absorption of the hybrid GO-AuNP films is attributed to the hybridisation of AuNPs.

4.2.3 Nonlinear refraction of hybrid GO films

The NLR of the hybrid GO-AuNP films are also investigated by the close-aperture Z-scan measurement at the same input laser fluence and fitted theoretically, as shown in Figure 4.7. The pronounced valley-peak patterns can be observed in all the hybrid GO-AuNP films, corresponding to the positive nonlinear refractive index n_2 (self-focusing). However, no obvious NLR of AuNP-only sample can be observed under the same laser excitation. The NLR of GO is mainly attributed to the population redistribution of the π electrons and the free carriers of the sp^2 domain as well as the bound electrons and the free carriers of the sp^3 matrix[101]. Compared to the reference GO film, the hybrid GO-AuNP films demonstrate stronger NLR as the concentration of AuNP increases, which is proved by the increase of the difference between the peak and valley transmittance ΔT_{p-v}.

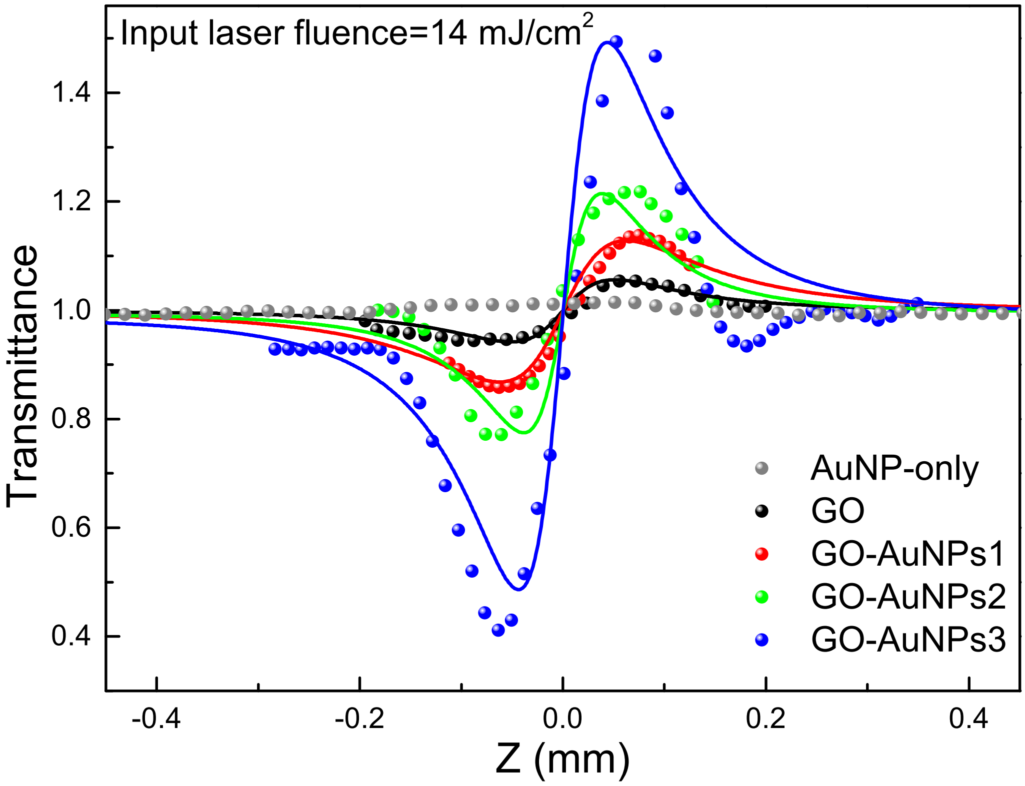

FIGURE 4.7: Close aperture Z-scan results (scatters) of the AuNP-only, GO, GO-AuNPs1, GO-AuNPs2 and GO-AuNPs3 samples at the same input laser fluence (14 mJ/cm^2). The theoretical fittings are indicated as solid lines.

4.2.4 Nonlinear coefficients of hybrid GO films

To further evaluate the magnitude of the nonlinearities of the hybrid GO-AuNP films, both the nonlinear absorption coefficient β and the nonlinear refractive index n_2 have been deduced by fitting the open-aperture and close-aperture curves respectively, as shown in Figure 4.8. β of the reference GO film is found to be as large as 17 cm/GW, which is the same order of the magnitude for the GO thin films reported recently[99]. However, β of the hybrid GO-AuNP films are found to increase as the concentration of AuNP increases, reaching 6 times of that of the reference GO film. On the other hand, the nonlinear refractive index of the reference GO film is fitted to be 4 x 10^{-13} cm^2/W. The hybridisation of AuNPs boosts the NLR as large as 6 times of that of the reference GO film. As a result, both the nonlinear absorption and the NLR can be effectively enhanced by the hybridisation of AuNPs.

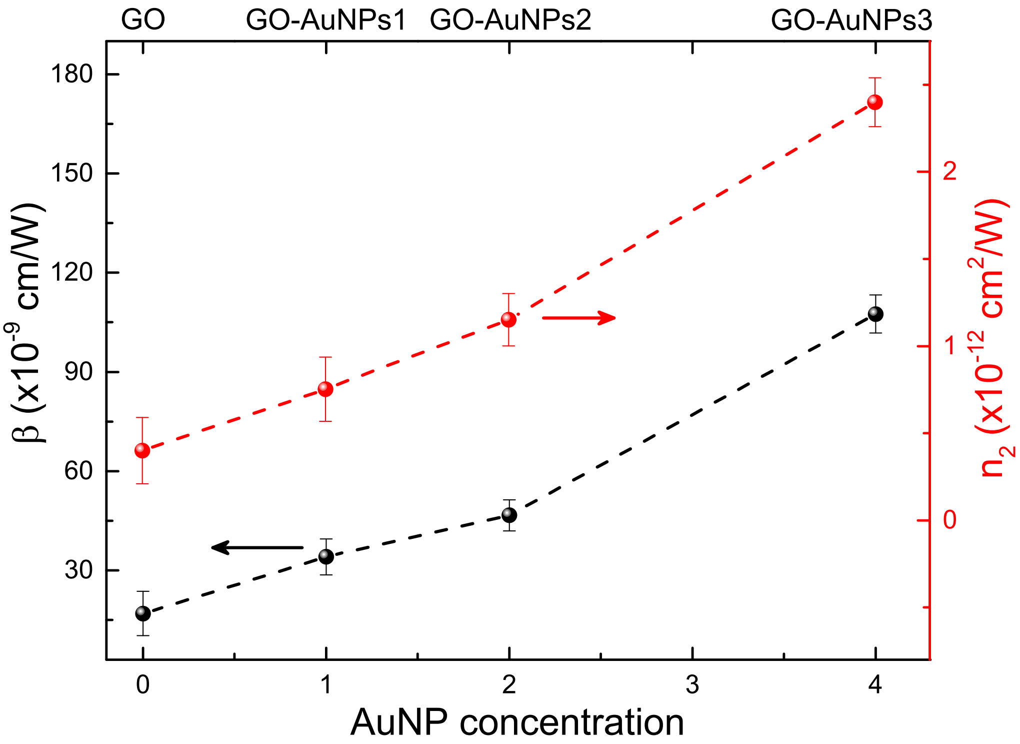

FIGURE 4.8: Nonlinear absorption coefficient β and nonlinear refractive index n_2 of GO, GO-AuNPs1, GO-AuNPs2 and GO-AuNPs3, deduced by fitting the open aperture and close aperture Z-scan curves.

The FTIR spectra have been widely used to study the vibrations of the oxygen functional groups in GO[189–192]. To further study the functionalisation of the hybrid GO-AuNP films and understand the possible mechanism of the enhanced nonlinearity, the FTIR transmission spectra of the four films are measured and shown as Figure 4.9. It is worth mentioning that the FTIR spectra of free-standing films (both GO and GO-AuNP), enabled by the vacuum filtration method, have been measured to eliminate any influence of the substrate. The FTIR spectrum of the reference GO film shows characteristic oxygen configurations in the structure[191], including the sp^2-hybridised C=C, carboxyl (COOH), ketonic species (C=O), hydroxyl (C-OH) and epoxide (C-O), as labelled in Figure 4.9. It can be observed with increased AuNP loading concentration, the hybrid GO-AuNP films show nearly similar FTIR spectra compared to the reference GO film, except for the increase of the absorption bands at 1651 cm^{-1} and 1074 cm^{-1}, corresponding to the COOH and C-OH groups. These results indicate that the AuNPs have been covalently bonded to the COOH and C-OH groups of the GO sheet, consistent with the previous report[193]. It is known that the C-OH group is located in the basal plane and the COOH group is at the edge site of the GO sheet[59]. Therefore AuNPs are believed to be decorated on the surface at the edge and between the GO sheets (see the inset of Figure 4.9). This chemical functionalisation of the GO film provides the potential enhancement mechanism for the observed high nonlinearity.

The enhanced optical nonlinearities of the hybrid GO-AuNP films are believed to be a result from the efficient energy and/or charge (electron) transfer upon photoexcitation, and the synergistic coupling effects between the constituents. Upon focused laser illumination, AuNPs undergo a multiphoton absorption process[108], which generates free electrons, making them function as electron donors in the GO-AuNP nanocomposite. The charge transfer from the electron donor, AuNPs, to the electron acceptor, GO, may result in the intramolecular donor-acceptor interaction between GO and AuNPs in our hybrid system. And GO could efficiently transfer the electrons, suppress the charge recombination and produce a charge-separated excited state[194–198]. Therefore, it is believed that the photo-induced energy and/or charge (electron) transfer from

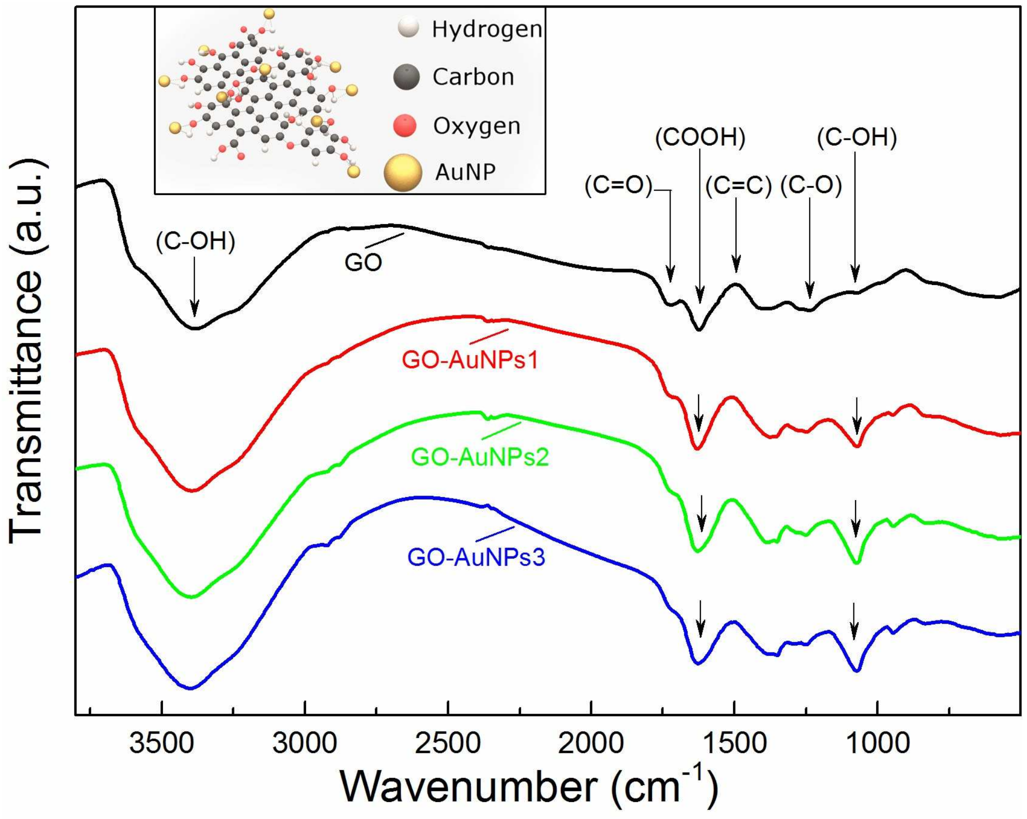

Figure 4.9: FTIR transmission spectra of the GO, GO-AuNPs1, GO-AuNPs2 and GO-AuNPs3 films. Various absorption bands corresponding to the functional groups in the GO films have been labelled. Inset: schematic illustration of the hybrid GO-AuNP films.

AuNPs to GO in the hybrid GO-AuNP films lead to the enhanced nonlinear optical properties. On the other hand, the rich organic anionic groups in GO make it chemically possible for AuNPs to interact with GO and the formation of interfacial bonds between AuNPs and GO, as suggested in the FTIR spectra in Figure 4.9, which may lead to strong synergistic coupling effects and hence the enhancement of nonlinear optical properties[199]. As mentioned in the previous section, the photoreduction of GO can occur under various laser illuminations due to the continuous removal of the oxygen functional groups on the GO sheets[200]. A threshold laser fluence can be found at which GO starts to be reduced. In our nonlinear experiment, the photoreduction of the hybrid GO-AuNP film has also been observed at high input laser fluence above 30 mJ/cm^2. To ensure the nonlinear effects reported in this work are from the intrinsic GO-AuNP films before any photoreduction happens, low input laser fluences (<25 mJ/cm^2) have been used. The linear absorption spectra of the hybrid films before and after the nonlinear measurements have been compared to confirm that no obvious change to the film has occurred during the measurement. As a result, the presented nonlinear effects of the hybrid GO-AuNP films are reversible and good stability of the GO-AuNP films can be observed under such laser illumination.

4.2.5 Conclusions

In summary, we present a universal and simple way to synthesise hybrid GO-AuNP films by the vacuum filtration method. The effective functionalisation of GO with AuNPs has been revealed by both the UV-Vis and FTIR spectra. Both the nonlinear absorption and refraction of the low-loss hybrid GO-AuNP films are found to be enhanced monotonically with the increase of AuNP concentration by the Z-scan measurement. The enhanced nonlinear light-matter interactions of the hybrid GO-AuNP films can be attributed to the efficient energy and/or charge (electron) transfer upon photoexcitation, and the synergistic coupling effects between AuNPs and GO. Our hybrid GO-AuNP films would provide a solid-state material platform for diverse nonlinear optical applications, such as ultra-sensitive optical limiter, optical modulator and photodetector. Moreover, the vacuum filtration method can serve as a universal strategy to functionalise GO by easily doping various nanoparticles with tunable concentrations to manipulate the physical properties of hybrid GO materials.

Chapter 5

Graphene oxide lens

As reviewed in Chapter 2, tremendous effects have been devoted in developing ultrathin flat lenses, such as micro Fresnel lenses and conventional lenses, plasmonic lenses and metalenses. However, it is still challenging to achieve micro optical lenses with 3D subwavelength focusing resolution, high focusing efficiency, broadband operation, ultrathin thickness, low-cost manufacturing and flexible integration capability. Given the linear and nonlinear optical properties of GO and rGO demonstrated in Chatper 3 and Chapter 4, it is now convenient to propose and realise various ultrathin flat optical devices on the GO and rGO films by fully exploring the flexible patterning capabilities of DLW on GO film as well as the controlled optical properties during the laser-induced reduction process. Therefore, in this chapter, we propose a new ultrathin flat lens concept that is able to effectively manipulate the phase and amplitude of an incident light beam simultaneously. We report on a 200 nm-thick GO flat lens with 3D subwavelength focusing that is able to tightly focus broadband light from visible to near-infrared (VIS-NIR) (∼1100 nm bandwidth) with an averaged absolute focusing efficiency of >32% over the entire band.

5.1 Conceptual design of the graphene oxide lens

The high quality ultrathin GO film has been prepared, and the surface morphology and thickness are characterised by using Bruker ContourGT InMotion 3D optical profiler, which offers a nondestructive method to measure the thickness of thin films. Figure 5.1 shows the surface profile of the prepared GO thin film with the well-controlled roughness of < 50 nm. In order to achieve the optimum focusing effect, the thickness of the prepared GO thin film is optimised at 200 nm based on the balanced requirements of the transmission, absorption, thickness variation, and achievable fabrication resolution.

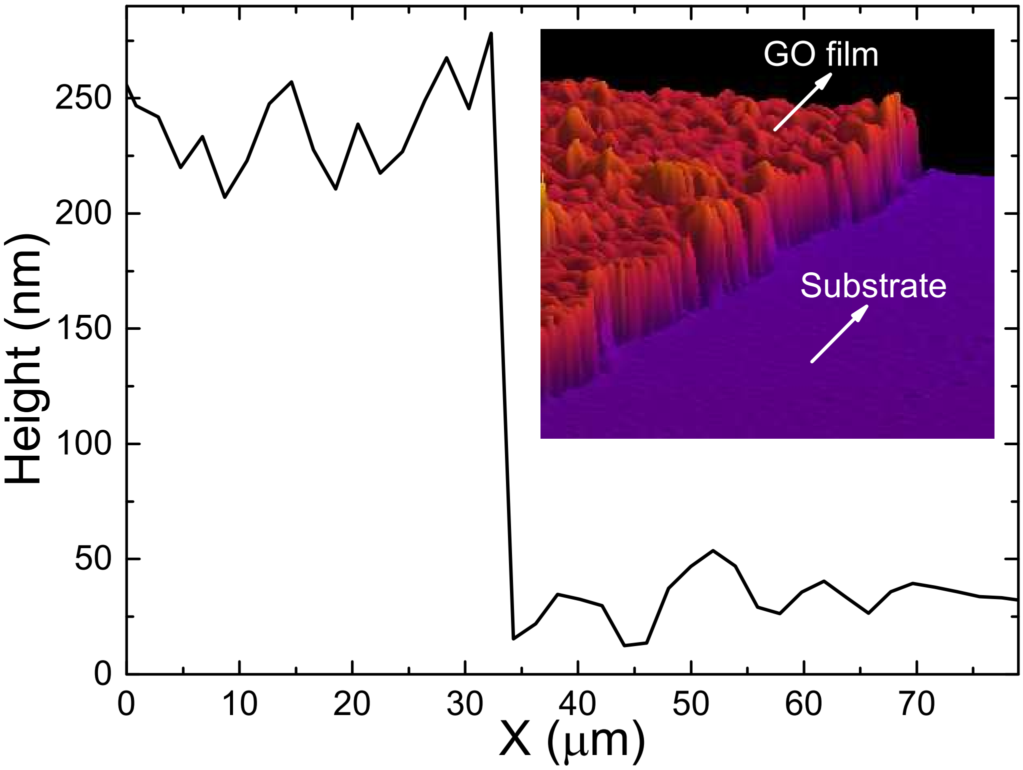

FIGURE 5.1: Thickness characterisation of the prepared GO thin film using an optical profiler. Inset: 3D optical profiler image of the prepared GO film on the substrate showing an averaged GO thickness of ~ 200 nm with an average roughness of < 50 nm.

The conceptual design of the GO ultrathin flat lens and the corresponding theoretical and experimental results are illustrated in Figure 5.2. The GO flat lens is made possible by the submicrometer concentric ring fabrication in a GO film by using the mask-free DLW method to covert the GO into rGO via the photoreduction process, as illustrated in Figure 5.2a. The laser power controlled removal of the oxygen functional groups in the exposed regions of the GO film leads to three continuously tunable local physical property variations: the reduction of film thickness (Figure 5.3a), the increase of refractive index and the decrease of transmission/increase of extinction coefficient (Figure 5.3b,c). It should be pointed out that the refractive index modulation of 0.8 has been achieved due to the higher oxidation extent of the improved GO solutions[201], compared to the results in Chapter 3. As a result, the three tunable local property variations provide an unprecedented flexibility in designing new ultrathin flat lens concept with capabilities of both amplitude and phase control (Figure 5.2b), and thus make our GO flat lens concept fundamentally different from the conventional Fresnel lenses and other flat lenses, which mostly rely on either phase or amplitude modulation solely[122,202].

To elucidate the light interaction with the GO flat lens, an analytical model based on the Rayleigh-Sommerfeld diffraction theory[122] is developed to evaluate the focusing capability of the GO lens. When a uniform plane wave impinges on the GO lens, part of the beam is absorbed and refracted by the rGO zones, experiencing substantial amplitude as well as phase modulations. The other part of the beam propagating through the GO zones only experiences ignorable amplitude modulations. The 3D focusing is a result of the interferences of wavelets originated in the lens plane from different zones[203], as illustrated in Figure 5.2d. It should be emphasised that although the refractive index modulation from GO to rGO is giant (Δn ∼0.8, one to two orders of magnitude larger than the conventional refractive materials[133]), the resultant maximum phase change between adjacent GO and rGO zones is smaller than π, which is the required phase change for effective constructive interference in the focal region. Under such a circumstance, the amplitude modulation in the rGO zones can make a substantial contribution to the final well-defined 3D focusing (Section 5.6).

The positions of each ring hold the key to allow both the amplitude and phase modulations positively contribute to the constructive interference in the focal region to generate a focal spot in the far field. To achieve constructive

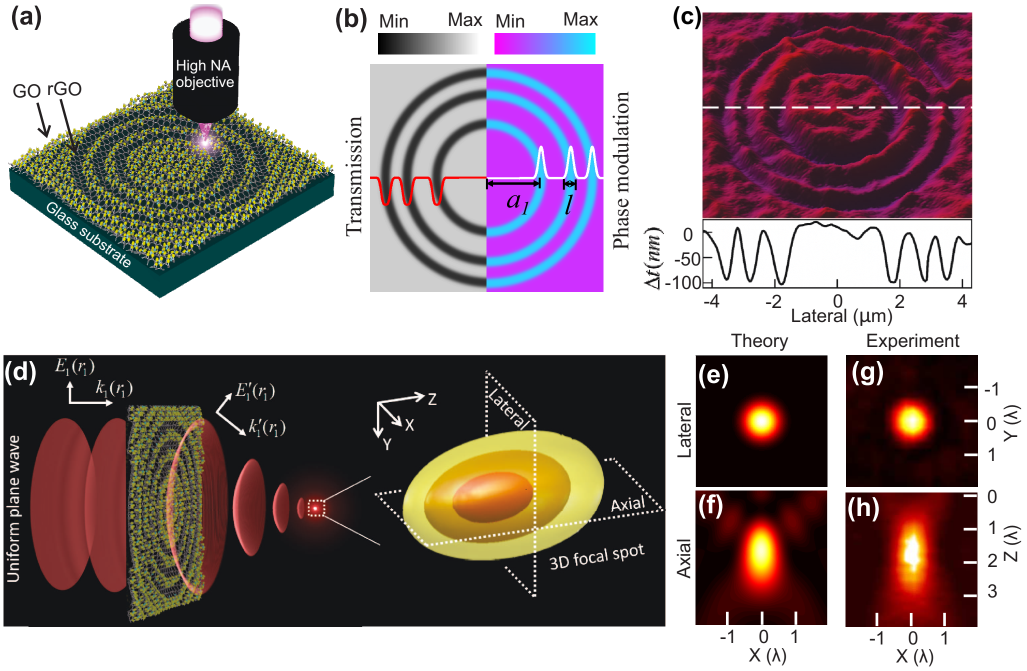

FIGURE 5.2: The design of the GO lens and the corresponding theoretical and experimental results. (a) Conceptual design and laser fabrication of the GO ultrathin lens. (b) Amplitude and phase modulations provided by the transmission and refractive index difference, respectively, between the GO and rGO zones. (c) Topographic profile of the GO lens measured with an optical profiler. (d) Left: Schematic of the wavefront manipulation by the GO lens converting the incident plane wave into a spherical wavefront. Right: Intensity distributions of the 3D focal spot predicted by the analytical model for a GO lens (a_1=1.8 μm, N=3). (e)-(f) Theoretical focal intensity distributions in the lateral and axial directions. (g)-(h) Experimental focal intensity distributions along the lateral and axial directions.

interference of all the GO and rGO zones in the focal region, the radius of the mth rGO zone a_m need to satisfy the following condition (Section 5.6):

$$a_m = \sqrt{\lambda \cdot f(2m - \Delta\varphi/\pi)} \tag{5.1}$$

where f is the designed focal length of the GO flat lens and $\Delta\varphi$ is the phase modulation between GO and rGO zones. It is thus evident that $a = \sqrt{\lambda \cdot f(2 - \Delta\varphi/\pi)}$ determines the positions of the rest rGO zones. As a result, we use a_1 and the total rGO zone number (N) to define the geometry of our GO flat lenses in this paper.

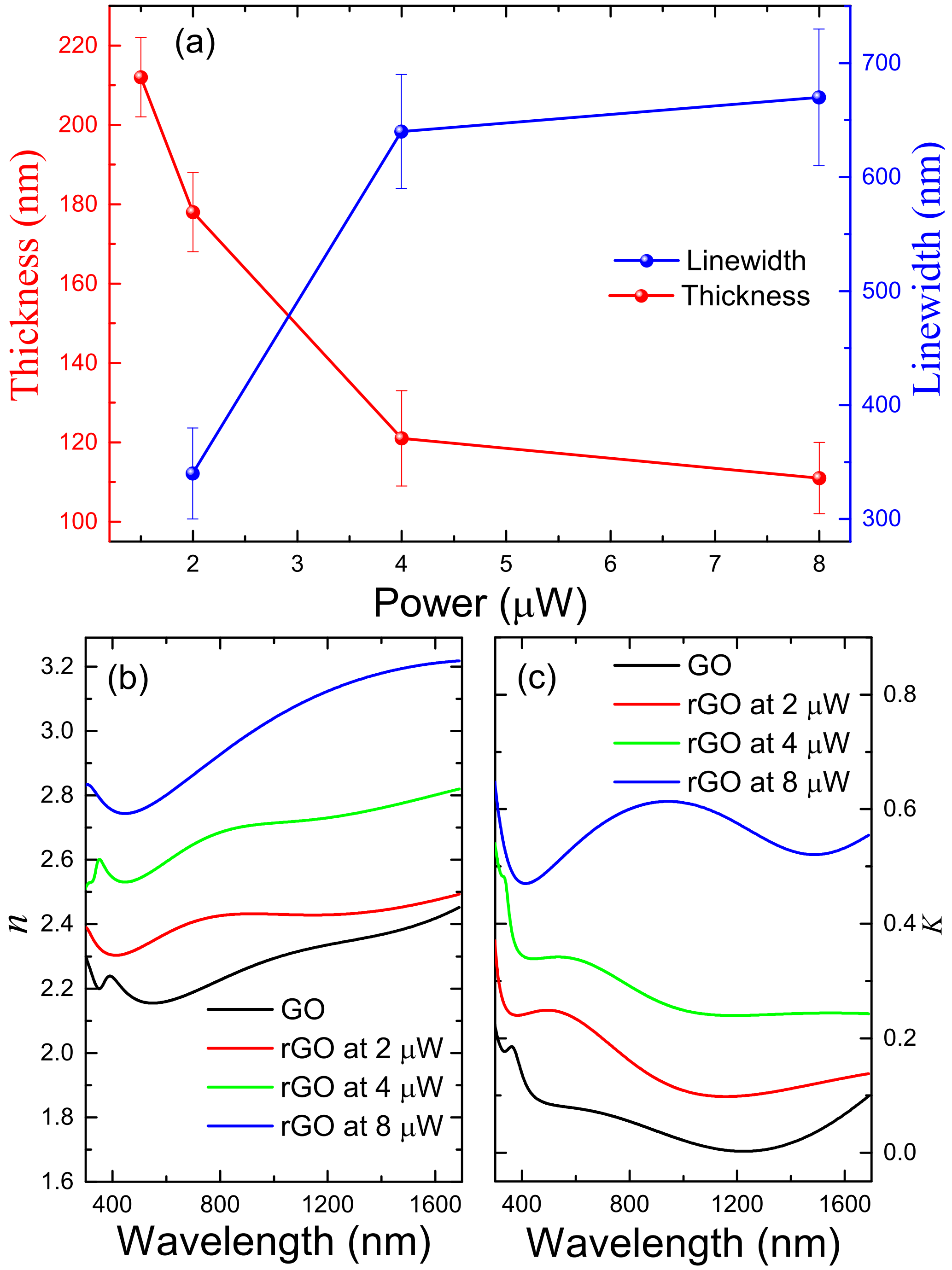

FIGURE 5.3: (a) Measured dependence of rGO film thicknesses and line widths on the power of the fabrication laser.(b) Dispersion relations of refractive indices (n) of rGO at different laser powers measured by using ellipsometry. (c) Measured dispersion relations of extinction coefficient (K) of rGO at different laser powers.

To achieve the optimised diffraction efficiency in the focal region, Gaussian profiles for the phase and amplitude modulation functions (Figure 5.2b,c) are employed to effectively direct the majority of the incident light to the first diffraction order[204]. The Gaussian profiles can be naturally facilitated by the intensity profile of the fabrication laser focused by a NA=1.4 objective at 800 nm, as shown in Figure 5.4. In this way, the theoretical maximal focusing efficiency of 50% can be achieved according to our calculations (not shown). In contrast, the conventional rectangular profiles distribute the light energy to a series of diffraction orders that severely degrade the focusing efficiency and resolution of the main focal spot. As shown in Figure 5.5, the focusing intensities of the lenses with Gaussian and rectangular profiles are calculated using our theoretical model and compared with each other. The lens with a Gaussian profile shows clearly much stronger focusing intensity with a higher focusing resolution.

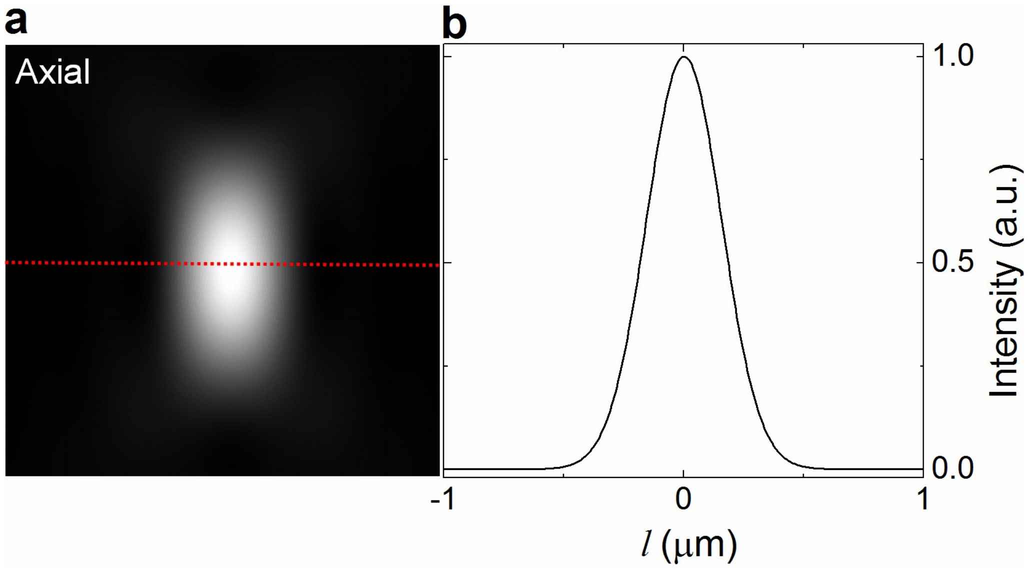

FIGURE 5.4: The normalised Gaussian beam profile of the fabrication laser at 800 nm focused by an NA=1.4 objective. (a) The intensity distribution of laser beam in the axial direction. (b) The cross-section of the intensity distribution along the red dash line in (a).

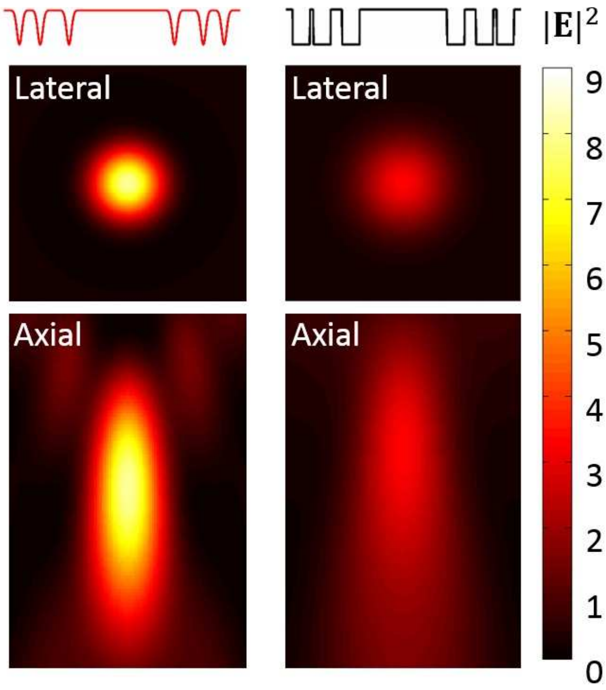

Figure 5.5: The focusing intensity distributions of lenses with Gaussian (left) and rectangular (right) profiles, respectively. Both lenses are designed with identical geometries (a_1=1.8 μm, N=3) and the illumination wavelength is fixed at 700 nm.

5.2 Experimental demonstration of the graphene oxide lens

To validate the theoretical model, the dependence of the focusing intensity of the GO lenses on a_1 is investigated. The calculated focusing intensity presents a nonlinear dependence on a_1, reaching a maximum for a three-ring (N=3) GO lens when a_1=1.8 μm. And the experimentally measured dependence of the normalised focusing intensities on a_1 agrees remarkably well with the theoretical prediction, as shown in Figure 5.6. The calculated 3D focal intensity distributions for the optimised lens (a_1=1.8 μm) is shown in Figure 5.2d, with the cross-sectional plots in the lateral and axial directions shown in Figure 5.2e,f, respectively. Well-defined strong focus with ignorable side-lobes (<10% of the intensity of the central lobe) is observed. The FWHM of the focal spot in the lateral direction (FWHM$_{lateral}$) is 0.8 λ and that in the axial direction (FWHM$_{axial}$) is 1.6 λ, leading to a high-quality 3D focal spot with wavelength-scale resolution. The corresponding GO lens is experimentally fabricated with the surface profile shown in Figure 5.2c, in which the Gaussian surface morphology is clearly evident. A Nikon N-STORM microscope is used for the visible lens characterisation. The cross-sectional distributions of the generated focal spots of the GO lenses are captured with a NA= 1.4, 100× objective into a CCD camera. By gradually adjusting the distance between the objective and the GO lens in a step of 100 nm, we are able to obtain the optical intensity distributions at different axial positions, and the 3D images of the focal spot can be reconstructed. The measured focal intensity distributions in the lateral (Figure 5.2g) and axial (Figure 5.2h) directions under 700 nm light illumination almost reproduce the theoretical plots, with a measured FWHM$_{lateral}$= 567 nm (0.81 λ) and a FWHM$_{axial}$= 1.3 μm (1.8 λ). The slight difference between the experiment and theory might be due to the imperfection of the fabrication and the surface roughness of the GO film.

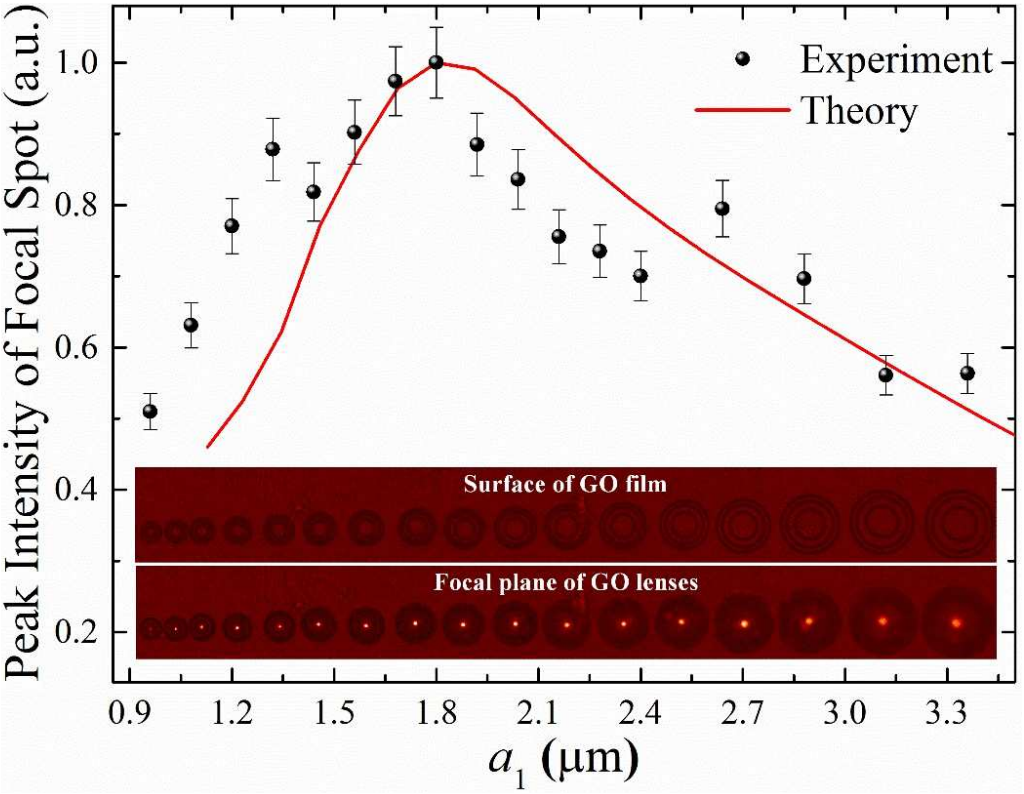

FIGURE 5.6: Dependence of focusing intensity on a_1. Inset: Measured images of GO lenses at the surface of GO film (top) and the lens focusing plane (Bottom).

Although 3D wavelength-level focusing has been demonstrated for the ultrathin

GO flat lens, it is not the best focusing resolution that the GO lens can achieve. According to our theoretical predictions, increasing the ring number N (equivalent to increase the aperture of the lens) and/or reducing a_1 can both improve the resolution, as shown in Figure 5.7. However, practically the maximum N and minimum a_1 are both determined by the smallest feature size (l) that the laser can fabricate on the GO film. To separate two consecutive rings, the feature size has to be smaller than the distance between the two rings as $l< a_{m+1}$-a_m. Meanwhile, the distance between the two outmost rings determines the maximum convergence angle β of the lens as $\sin\beta \propto 1/(a_N - a_{N-1})$. Therefore, the minimal feature size of each rGO zone is the key parameter practically limiting the achievable focusing resolution of the lens.

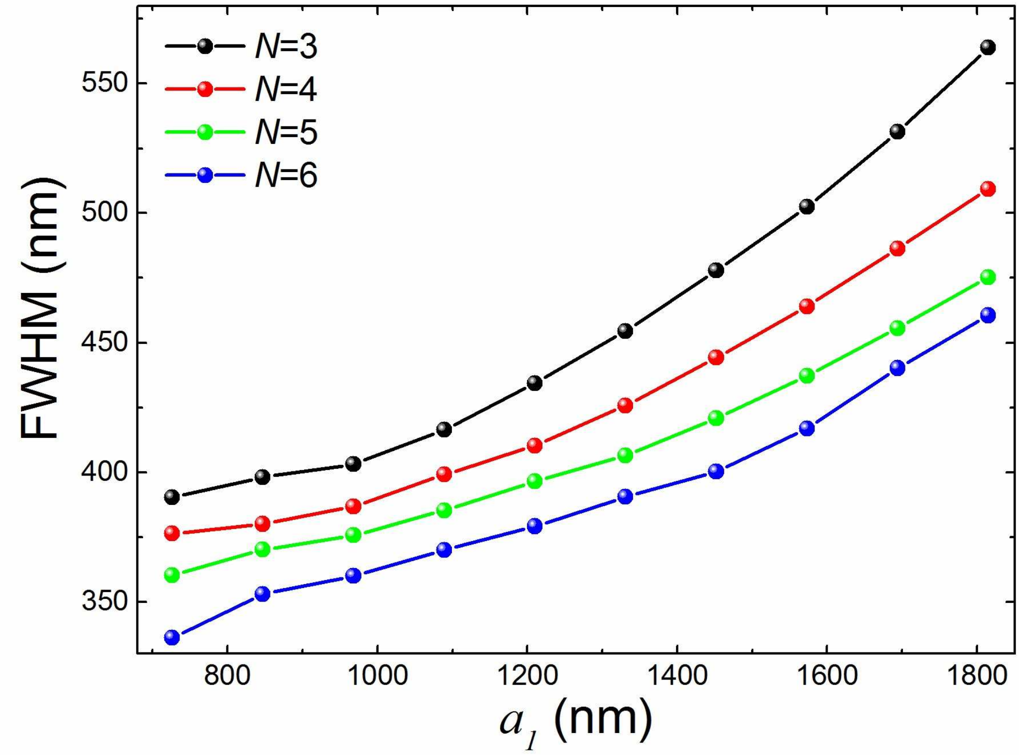

Figure 5.7: Focusing resolution variations at different N and a_1.

However, laser fabrication based on thermal reduction in literature can only achieve minimum feature size >1 μm[205], which severely restricts the lateral focusing resolution of the GO flat lens to be over 6.5 λ according to our experiments using a MHz repetition rate laser (not shown). Recently, it has been reported that GO has a threshold photon energy for photochemical reduction at

3.2 eV (λ=390 nm). Therefore, for a high peak power femtosecond laser beam operating at 800 nm, it is potentially possible to harness the nonlinear photochemical mechanism to enhance the fabrication resolution[206,207]. As a result, to minimise the thermal effect and potentially make use of the high resolution nonlinear reduction mechanism, we tightly focus low repetition rate femtosecond pulsed laser beam (100 fs, 10 kHz, 800 nm) with a high NA (1.4) objective to ensure the interval of the laser pulse to be sufficiently larger than the thermal diffusion constant of the GO[205]. As a result, a record small line width of $\sim$ 300 nm (0.38 λ) is achieved in the rGO laser fabrication (Figure 5.3a), which represents a more than three-fold resolution enhancement compared to the literature[205]. Consequently, maximum 6 rings with a minimum a_1=730 nm can be fabricated. It should be noted that the notation a_1 is the radius of the first ring of the lens, whereas the minimal feature size is the smallest fabricated line width l. The minimum a_1 is determined by the minimum feature size l ($\sim$ 300 nm).

Figure 5.8 presents the measured lateral and axial focusing intensity distributions of the experimentally fabricated 6-ring ultrathin GO flat lenses with different a_1 from 730 nm to 1200 nm. It is obvious that well-defined 3D foci are achieved in all cases. The FWHM in both the lateral and axial directions of the foci reduce as the decrease of a_1 following exactly the same trend predicted by our theory (Figure 5.8c). The highest lateral resolution is 343 nm (0.49 λ) and axial resolution is 584 nm (0.83 λ) illuminated by a light beam of λ=700 nm, leading to a 3D diffraction-limited resolution of $\lambda^3/5$. The demonstrated 3D subwavelength focal spot is to our knowledge the best far-field 3D resolution achieved so far for an ultrathin flat lens.

5.3 Focus intensity tuning

The fact that the phase and amplitude modulations of rGO zones are highly dependent on the fabrication laser power offers a simple and unique approach

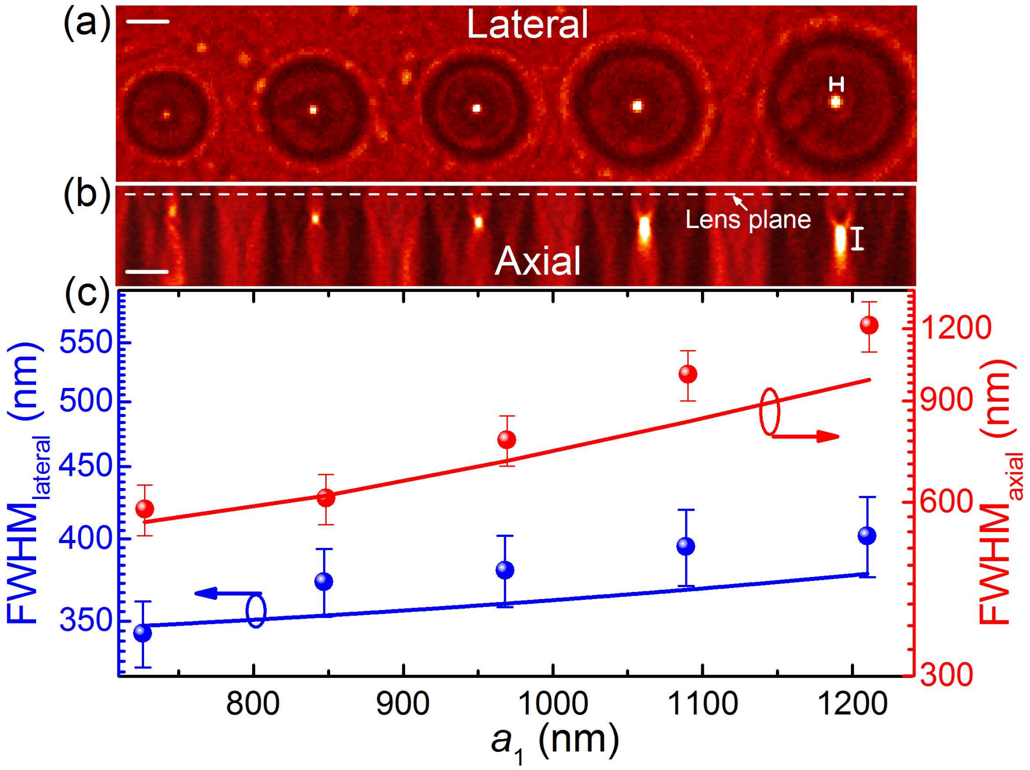

Figure 5.8: Dependence of focusing resolution on the radii of the first ring (a_1) for a six ring GO lens (N=6). Top: Measured cross-sectional intensity distributions in the lateral (a) and axial (b) directions, respectively. The lens plane is indicated as the white dash line in (b). (c) The measured dependence of FWHM$_{lateral}$ (blue spheres) and FWHM$_{axial}$ (red spheres) on a_1. The corresponding theoretical predictions (blue and red solid lines) are also presented and show excellent agreements with experimental results. Scale bar, 2 μm.

to tune the focus of the ultrathin GO flat lens. To demonstrate this capability, GO lenses with an identical geometry (a_1=1.6 μm, N=3) are fabricated with increasing laser powers from 1.5 μW to 8 μW. The normalised peak focusing intensity is found to increase with the fabrication laser power monotonically, as shown in Figure 5.9a. To further illustrate the laser controllable tunability of the focus intensity and large scale fabrication capability, a large size 200 nm-thick GO thin film is prepared on a glass substrate (Figure 5.9b), and a contour of Australian map comprising of 162 GO lenses and a contour of a kangaroo comprising of 89 GO lenses are fabricated with 3 μW and 7 μW laser powers respectively in a 1.5 mm^2 area (dashed circle in Figure 5.9b), as shown in the microscopic image in Figure 5.9c. By shining light on the fabricated region (Figure 5.9d), the kangaroo contour shows a much larger brightness compared to the contour of Australian map due to the higher focusing intensity of the comprising lenses (Figure 5.9e). The enlarged lateral cross-sectional intensity distributions of GO lenses taken from the kangaroo and Australian map are also shown in the insets of Figure 5.9a, which highlight the focusing intensity differences. These results demonstrate not only the versatile laser addressable tunability of the GO flat lenses, but also the scalable and reliable laser fabrication of GO films ready for large-scale manufacturing and applications.

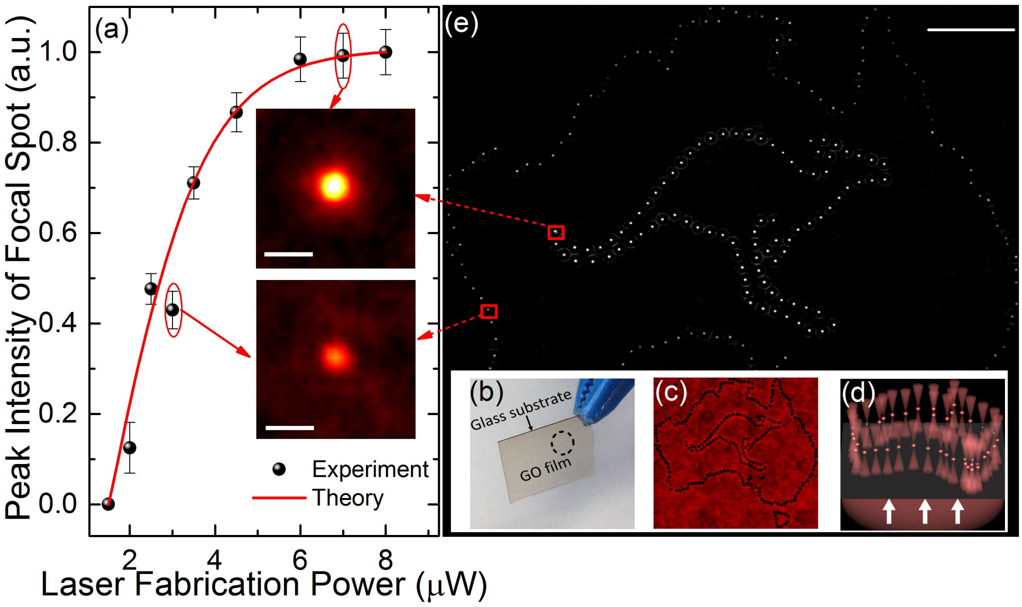

FIGURE 5.9: Laser controllable tunability of the focus intensity. (a) Normalised focusing intensities of GO lenses fabricated at increasing laser powers from 1.5 μW to 8 μW (black spheres). Theoretical prediction (red solid line) shows remarkable agreements with the experimental results. Insets: Cross-sectional intensity distributions in the lateral direction of two GO lenses fabricated at 3 μW and 7 μW, respectively. Scale bar, 1 μm. (b) The prepared large size 200 nm-thick GO thin film on a glass substrate. (c) Two sets of GO lenses following the contours of an Australian map and a kangaroo are patterned in a 1.5 mm^2 area (dashed circle in (b)). (d) Schematic diagram of focusing of the GO lenses under a plane wave illumination (white arrows). (e) Measured microscopic images of the contours of an Australian map and a kangaroo at the lens focusing plane showing different focusing intensities. Scale bar, 200 μm.

5.4 Broadband focusing

One of the critical challenges of the current ultrathin lenses such as metalenses[110], plasmonic lenses[123] and super-oscillation lenses[129] is the narrow bandwidth due to the constrains from both the dispersion properties of the constituting materials and the fundamental lens operation mechanisms[141]. The state-of-the-art bandwidth for an ultrathin flat lens is 280 nm[125], whereas most ultrathin flat lenses are only functional at a single wavelength[110,208]. In contrast, the wavefront shaping mechanism of our GO lens originates from the effective amplitude and phase modulations between the GO and rGO zones. Given the fact that the large modulations of both the refractive index and extinction coefficient between GO and rGO are almost maintained from visible (above 350 nm) to IR regions (Figure 5.3b,c), the GO lens provides a possible mechanism for achieving broadband focusing.

To realise the broadband focusing, the dependence of broadband focusing intensity of GO lenses on the first ring size (a_1) is calculated, as shown in Figure 5.10. For each lens with different a_1, an optimal wavelength exists at which the maximum focusing intensity can be achieved. As a result, we design and fabricate a GO lens (a_1=3.3 μm, N=3) with the optimal performance over the entire VIS-NIR wavelength range. A super-continuum laser with illumination wavelengths from 450 nm up to 1500 nm is used as the light source. Two CCD cameras, operating at visible (Watec 902H3 SUPREME) and IR (Xenics Xeva-1.7-320) regions, respectively, are used to capture the focal plane images of the GO lens at different wavelengths. Therefore, the cross-sectional focusing intensity distributions in the lateral direction of this lens are experimentally characterised under different illumination wavelengths from 450 nm to 1500 nm, as shown in the insets of Figure 5.11a. The results clearly demonstrate that well-defined subwavelength foci have been achieved at all wavelengths. Moreover, the measured absolute focusing efficiencies, defined as the ratio of the power in the focal region to the total input power before the lens, are higher than 32% on average in the entire measured VIS-NIR band (Figure 5.11a), representing a more than 30-time improvement compared to the state-of-the-art ultrathin flat lens[117]. It should be emphasised that such a broadband high resolution focusing over 1050 nm bandwidth is achieved with a single GO lens. In addition, it is interesting to note that the measured FWHM$_{lateral}$ of the foci at different wavelengths shows an almost constant value of ~ 0.8 μm, which is also predictable from the operating principle of our ultrathin lenses.

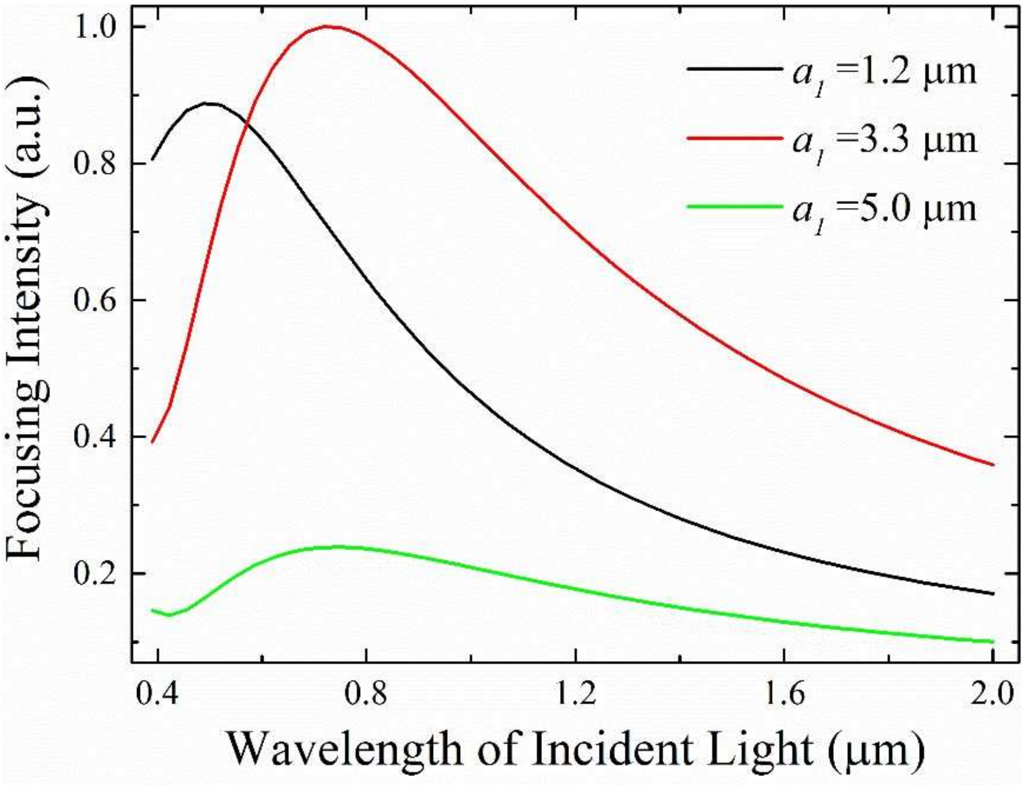

FIGURE 5.10: Broadband focusing intensity of GO lenses with different a_1

The broadband focusing of the GO lens allows us to minimise the chromatic aberration specifically in the visible regime, which is critical for multi-wavelength optical imaging and communications[138]. By carefully designing a_1 of our GO lens, the shift of the focal length over all visible wavelengths can be smaller than the depth of focus, which suggests that our GO lens can be optimised to focus the incoherent white light within a common focal region. To achieve the minimal chromatic aberration in the visible regime, a GO lens (a_1=1.2 μm, N=3) has been fabricated and characterised under white light illumination. The cross-sectional intensity distributions in both the lateral and axial directions are shown in Figure 5.11b,c, exhibiting an obvious high resolution 3D focal spot. By fitting the intensity distributions (Figure 5.11d), the FWHM in the lateral and axial directions are found to be 577 nm and 1.56 μm, respectively, which even outperform most of the ultrathin lens operating under single wavelength

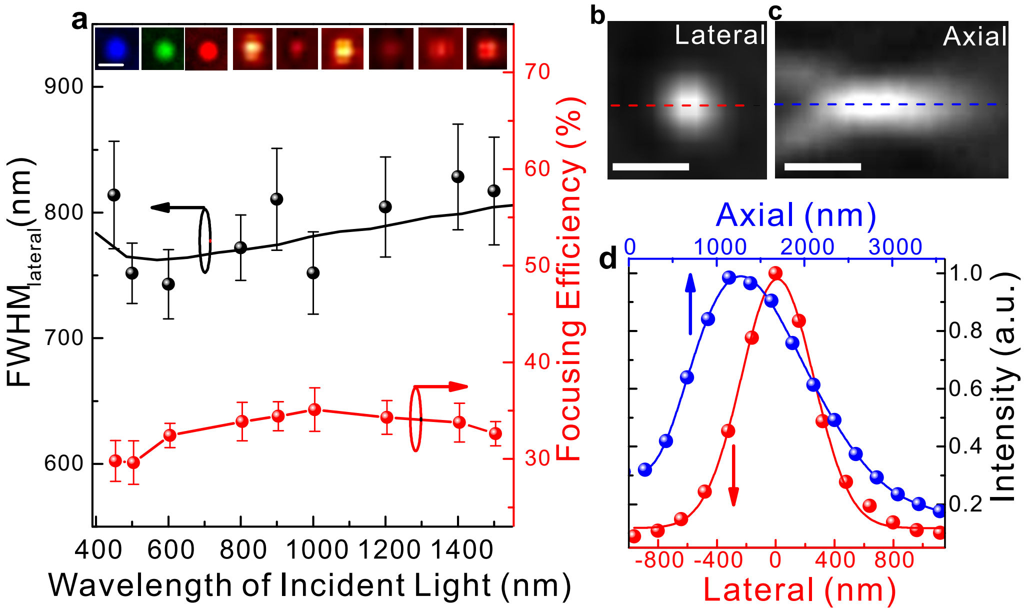

FIGURE 5.11: The broadband focusing capability from visible to IR. (a) Characterisation of the broadband focusing ability of a GO lens (a_1=3.3 μm, N=3). Both FWHM$_{lateral}$ (black spheres) and focusing efficiency (red spheres) are measured over a broadband illumination of the wavelengths from 450 nm to 1500 nm. Theoretical predictions of FWHM$_{lateral}$ (black solid line) are also presented matching well with the experimental results. Insets: Cross-sectional intensity distributions along the lateral direction captured by two charge-coupled devices (CCDs) operating at the visible and IR, respectively. Different colours indicating different input wavelengths schematically. Scale bar, 1 μm. (b)-(d) Focusing ability of a GO lens (a_1=1.2 μm, N=3) under a white light illumination. Measured cross-sectional intensity distributions along the lateral (b) and axial (c) directions under a white light illumination. The intensity distributions along the red dashed line in (b) and blue dashed line in (c) are also plotted (red and blue spheres in (d)) and fitted (red and blue solid lines in (d)), respectively. Scale bar, 1 μm.

illumination[110,208]. This is to our knowledge the first demonstration of a subwavelength scale flat lens that can focus white light three-dimensionally with minimal chromatic aberration.

5.5 Mechanical robustness and wavefront engineering

Given its strong mechanical robustness, large scale integratability and simultaneous patterning and beam manipulation abilities during the one-step

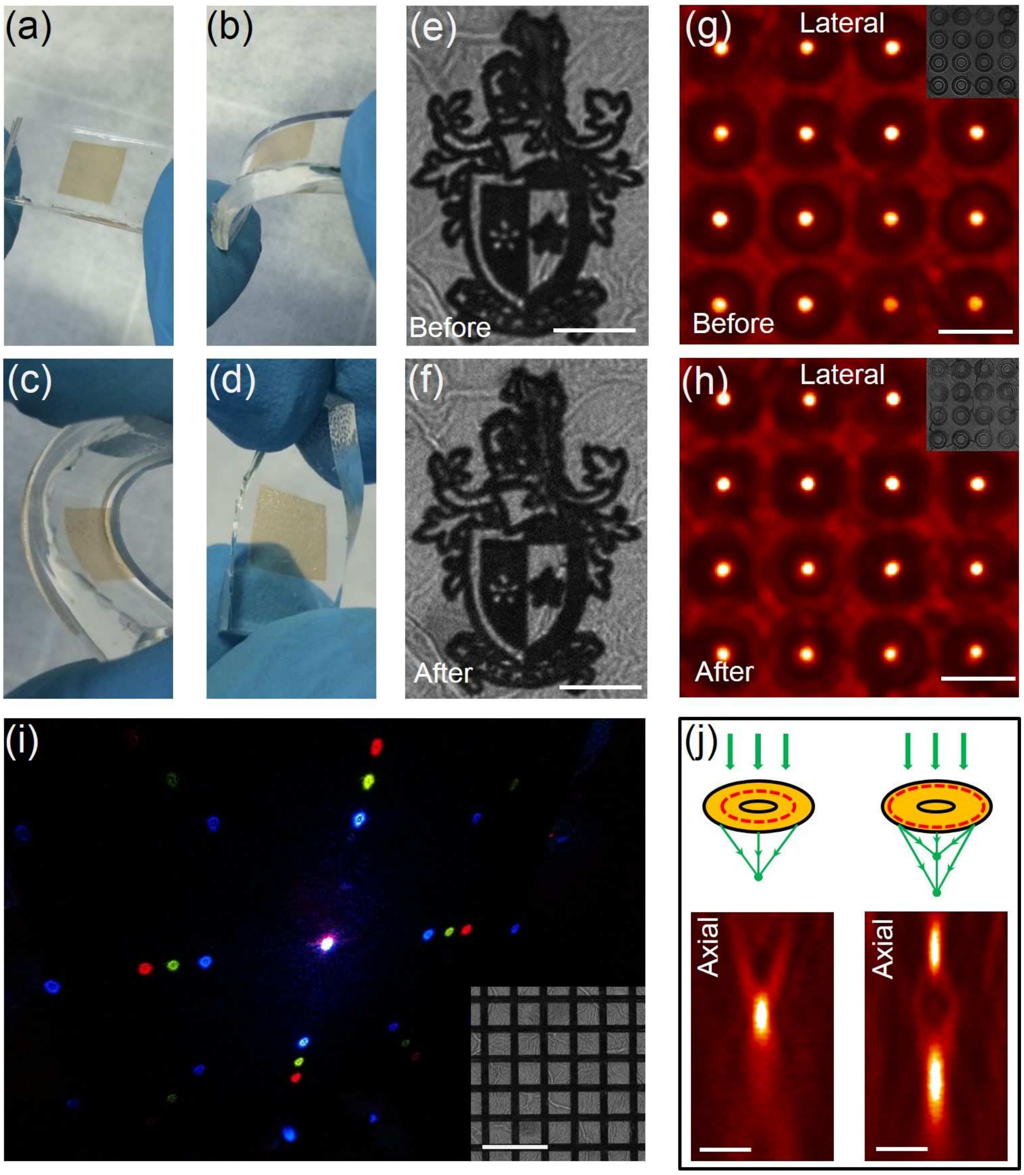

FIGURE 5.12: The mechanical flexibility and the versatility in wavefront manipulations of the GO films. (a)-(d) Bending and twisting of the GO thin film on a PDMS substrate. (e)-(f) Microscopic images of Swinburne logo fabricated on the GO thin film before (e) and after (f) bending. Scale bar, 10 μm. (g)-(h) Microscopic images of the GO lens array at the focusing plane before (g) and after (h) bending. Scale bar, 30 μm. Insets: microscopic images of the GO lens array fabricated on the GO film. (i) Diffraction image of a 2D grating, retrieved by using three beams at wavelength of 405 nm, 561 nm and 633 nm simultaneously. Inset: microscopic image of the 2D grating fabricated on the GO film. Scale bar, 20 μm. (j) Comparison of the single focal spot (left column) and multi-foci GO lenses (right column). The designs are shown schematically (top panel) and the focal intensity distributions along the axial directions are characterised experimentally (bottom panel). Scale bar, 2 μm.

mask-free DLW process, GO ultrathin films have the potential to revolutionise the next-generation integrated optical systems by making miniaturised and fully flexible photonics devices. To illustrate its mechanical flexibility and the versatility in wavefront manipulations, a large scale GO thin film is integrated on a flexible PDMS substrate and then is patterned with complex logos as well as other functional diffractive optical elements, as shown in Figure 5.12. After various bending and twisting (Figure 5.11a-d), both the complex logo (Figure 5.11e-f) and the 4 × 4 GO lens array (Figure 5.11g-h) survive without any compromise of the morphology or optical performance, demonstrating the excellent mechanical strength of our GO films.

Moreover, the wavefront shaping mechanism with our ultrathin GO film is readily applicable to other diffractive optical element design. Figure 5.11i presents a 2D grating, in which rGO (darker regions) and GO offer periodic phase and amplitude modulations. The diffraction pattern under 405 nm, 561 nm and 633 nm lasers simultaneous illumination clearly show the high diffraction performance of the GO grating. Finally, as shown in Figure 5.11j, a multi-foci GO lens (right column) can be realised by simply adjusting the position of the rGO rings in the single focal spot GO lens design (left column), which offers a great potential for super-resolution imaging, optical data storage and sensing applications[209].

5.6 Analytical calculation method of graphene oxide lens

The intensity distribution in the focal region of the ultrathin lens can be calculated using the Rayleigh-Sommerfeld diffraction theory[203] based on the Fresnel approximation with a circular symmetry as

$$E_2(r_2, z) = \frac{i2\pi}{\lambda z}\exp(-ikz)\exp(-\frac{ikr_2{}^2}{2z})\int_0^{+\infty} E_1(r_1)\exp(-\frac{ikr_1{}^2}{2z})J_0(\frac{kr_1r_2}{z})r_1dr_1 \tag{5.2}$$

where the subscripts '1' and '2' indicate the parameters in the lens plane and in the focal region, respectively. As a result, the field distributions in the focal region (E_2) at different lateral (r_2) and axial (z) positions can be calculated by integrating the field distribution ($E_1(r_1)$) over the entire lens plane. One example showing here is a GO lens design with three rGO zones, as shown in Figure 5.13.

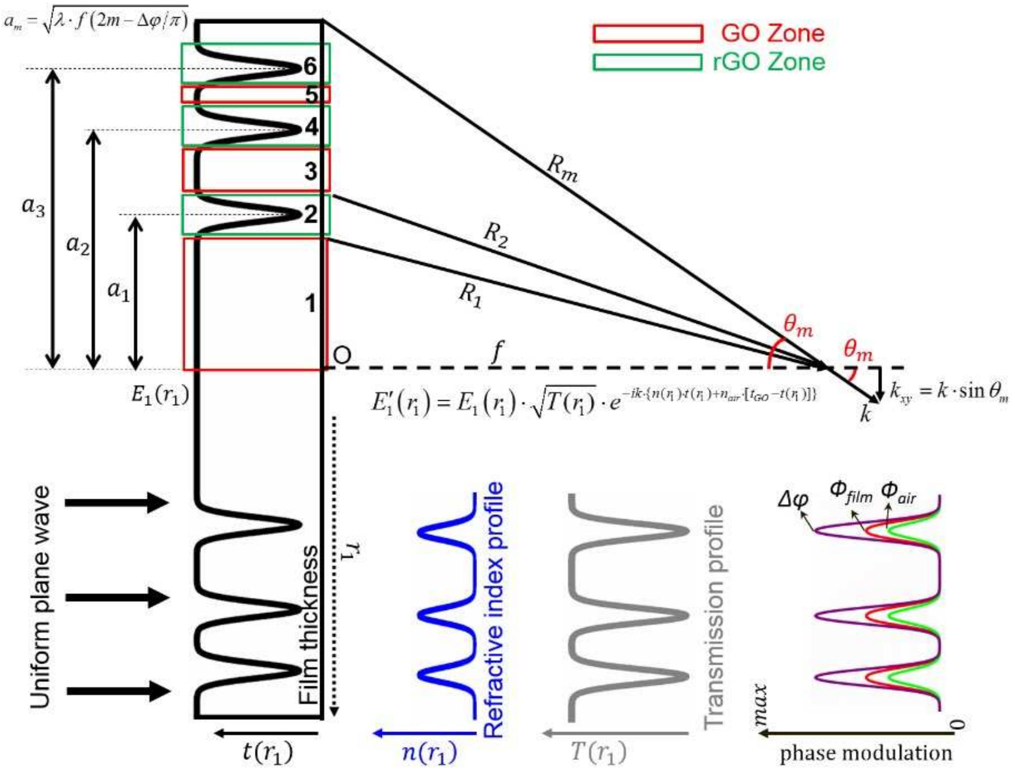

FIGURE 5.13: Schematic of the theoretical model calculating the focusing properties of a GO flat lens. a_m (a_1, a_2 and a_3) is the position of the laser fabricated mth rGO ring. f is the focal length of the GO lens. Six alternating rGO and GO zones are indicated as green and red rectangles, respectively. The Gaussian profiles of film thickness $t(r_1)$, refractive index $n(r_1)$ and transmission $T(r_1)$ have been plotted schematically. The plots of Φ_{film}, Φ_{air} and $\Delta\varphi$ have also been included.

When a uniform plane wave ($E_1(r_1)$=1) impinges the GO lens, part of the beam is absorbed and refracted by the rGO zones, experiencing substantial amplitude as well as phase modulations. The other part of the beam propagates through the GO zones only experiencing ignorable amplitude modulation. The modulated E-field becomes:

$$E'_1(r_1) = E_1(r_1) \cdot \sqrt{T(r_1)} \cdot e^{-ik(\Phi_{film}+\Phi_{air})} \tag{5.3}$$

where $T(r_1)$ is the transmission distribution, which can be calculated using the Beer-Lambert equation:

$$T(r_1) = e^{-\alpha(r_1)\cdot t(r_1)} \tag{5.4}$$

where $\alpha(r_1)$ is the absorption coefficient which can be calculated from extinction coefficient $K(r_1)$ through $\alpha(r_1)$=$4\pi \times K(r_1)/\lambda$. Φ_{film} (=$n(r_1)t(r_1)$) and Φ_{air} (=$n_{air}[t_{GO}$-$t(r_1)]$) are the phase modulations provided by the film and the air, respectively. Meanwhile, the modulated refractive index $n(r_1)$, thickness $t(r_1)$ and extinction coefficient $K(r_1)$ due to the laser photo-reduction can be formulated as:

$$\begin{cases} n(r_1) = n_{GO} + \Delta n \cdot M(r_1) \\ t(r_1) = t_{GO} + \Delta t \cdot M(r_1) \\ K(r_1) = K_{GO} + \Delta K \cdot M(r_1) \end{cases} \tag{5.5}$$

Here n_{GO}=2.2 is the refractive index of the GO film at 700 nm. t_{GO} = 200 nm is the thickness of the GO film. K_{GO} = 0.07 is the extinction coefficient of GO at 700 nm. All these parameters are measured experimentally. The modulation function M is expressed as

$$M(r_1) = C \sum_{m=1}^{N} e^{\frac{(r_1-a_m)^2}{2w^2}} \tag{5.6}$$

where C is a constant depending on the femtosecond laser power. a_m is the position of mth rGO zone, and N is the total number of rGO zones (N=3 in this design). Note that the modulation function M shows a Gaussian shape governed by the intensity distribution of the laser focus, with w controlling the FWHM. To this end, we have successfully applied the Gaussian profiles of material properties as well as the geometries of the GO lens into the analytical model, which is ready to calculate the performance of the GO lens made of materials with different physical properties at various geometries and is used all through this paper.

To understand the role of amplitude and phase modulations, the interference of two coherent beams with certain phase and amplitude modulations is studied firstly. Assuming that the electric fields of beam 1 and beam 2 are:

$$\begin{cases} E_1 = A_1 \cdot e^{-i\varphi_1} \\ E_2 = \sqrt{T_{12}} \cdot A_1 \cdot e^{-i(\varphi_1 + \Delta\varphi_{12})} \end{cases} \tag{5.7}$$

where T_{12} and $\Delta\varphi_{12}$ correspond to the amplitude and phase modulations. As a result, the intensity of the interference beam can be calculated directly via $|E|^2 = |E_1 + E_2|^2$. Therefore, the dependence of the interference intensity on the phase and amplitude modulations can be calculated, as shown in Figure 5.14. We can see clearly that the largest intensity occurs when the phase modulation ($\Delta\varphi_{12}$) is either zero or 2π with no amplitude modulation (T_{12}=1), which is well known as the constructive interference condition with $|E|^2 = 4|E_1|^2$. Moreover, four regions with different roles of amplitude and phase modulations can be distinguished, as indicated in Figure 5.14. In regions I and III, increase of phase modulation reduces the interference intensity, whereas the interference intensity increases with the phase modulation in regions II and IV. On the other hand, in regions I and IV, larger amplitude modulation deteriorates the interference intensity. However, in regions II and III it is preferred to have larger amplitude modulation.

As a result, to show the effects of both phase and amplitude modulations in a general lens design without limiting to any particular case, numerical calculations were applied to map over the complete phase modulation ($0 \sim 2\pi$) and amplitude modulation (0∼1), as shown in Figure 5.15. One can see clearly that different roles of amplitude and phase modulations can be distinguished, which shows similar behaviour as two beam interference (Figure 5.14). Moreover, the unique surface contour shows the dependence of the lens performance (e. g. lens peak focusing intensity normalised to the incident beam intensity in Figure 5.15) on the phase and amplitude modulations. As a result, given the attainable material properties, both the amplitude and phase modulations, and the geometry of the lens can be optimised to achieve the best performance. Compared to the conventional

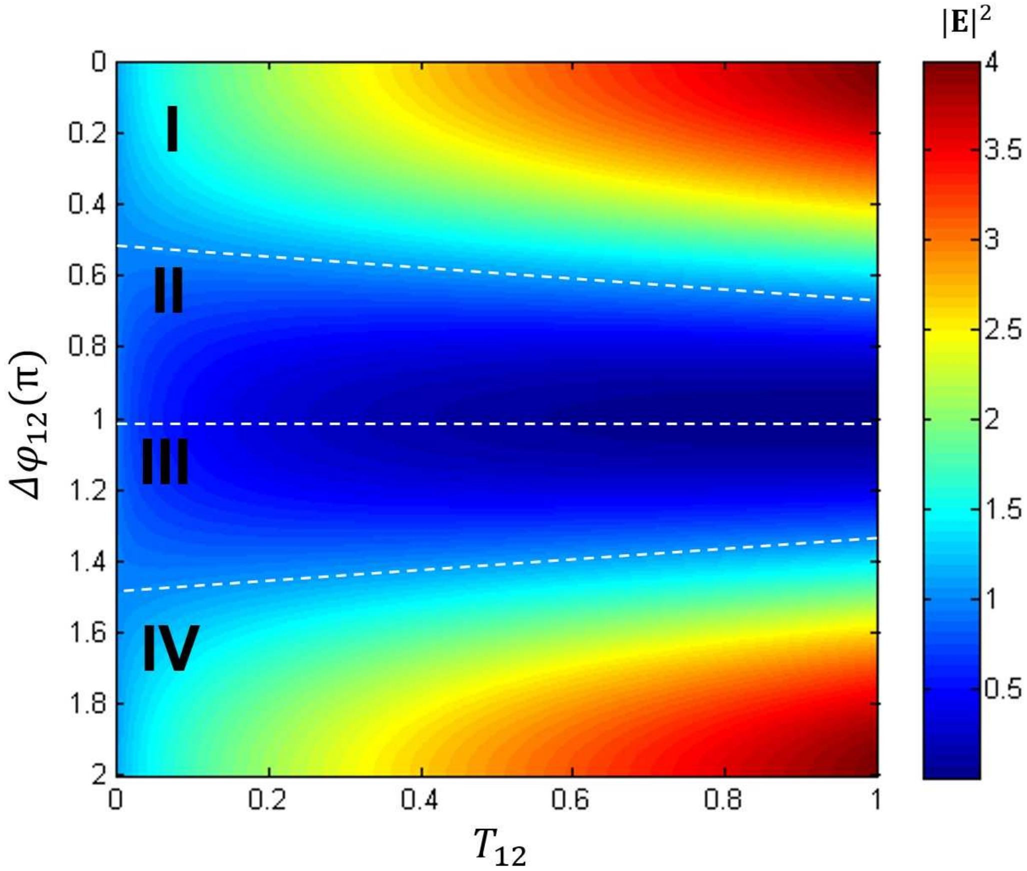

Figure 5.14: Effects of amplitude and phase modulations on the interference of two coherent beams.

amplitude type Fresnel zone plate, more light is transmitted for our GO lens. The predicated maximum efficiency reaches >50%, which breaks the theoretical limitation of focusing efficiency of amplitude-type Fresnel zone plate (∼10%)[122]. Although 2π phase shift is not achieved between the adjacent GO and rGO zones, the Gaussian profile of each rGO boosts the overall GO lens performance over phase type Fresnel lens in subwavelength 3D resolution, ultrathin lens thickness and smaller lens sizes with a focusing efficiency (>50%) exceeding the theoretical limitations of phase type Fresnel lens (40%).

For our GO lens, the focusing is the interference of light passing through the GO and rGO zones, which provide phase and amplitude modulations. The phase modulation between the adjacent GO and rGO zones (only zone 1 and zone 2 are shown here) can be expressed as:

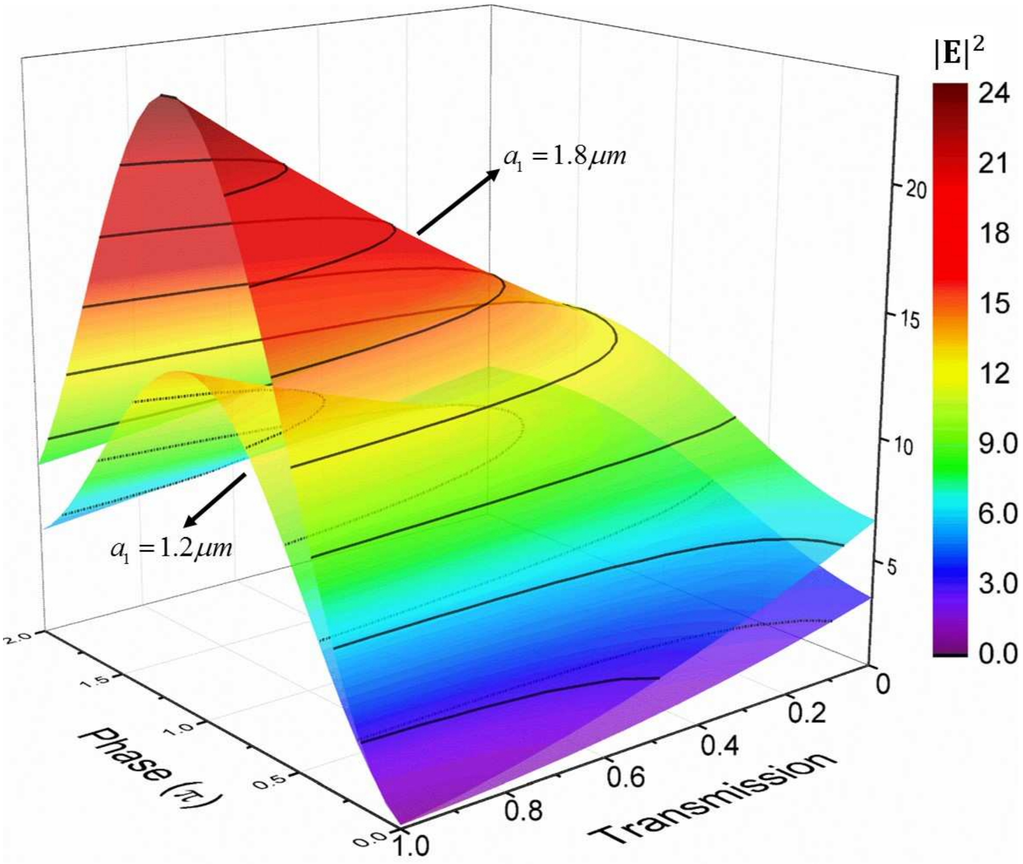

FIGURE 5.15: Effects of transmission (amplitude) and phase modulations on the GO lens with different a_1.

$$\Delta\phi = \frac{2\pi}{\lambda} \cdot (R_2 - R_1) + \Delta\varphi \tag{5.8}$$

where $\Delta\varphi$ is the phase modulation between GO and rGO zones. Given the fact that the phase modulation within one rGO zone is comparatively weak, it is physically sound to approximate the phase modulation $\Delta\varphi$ as a constant across each rGO zone, which is taken as the average of the Gaussian function. To guarantee a constructive interference between all the GO zones and rGO zones, $\Delta\varphi$ should be fixed at 2π, corresponding to constructive interference. As a result, we can get:

$$(R_m - f) = m\lambda - \lambda \cdot \frac{\Delta\varphi}{2\pi} \tag{5.9}$$

where f is the focal length of GO lens, as indicated in Figure 5.13. Therefore, by solving the Equation 5.9 using the relation $R_m^2 = a_m^2 + f^2$, we can easily obtain that:

$$a_m = \sqrt{\lambda \cdot f(2m - \Delta\varphi/\pi)} \tag{5.10}$$

During the laser-induced reduction process of GO, three physical properties (film thickness, refractive index and extinction coefficient) are correlated and all dependent on the reduction extent, which is eventually controlled by the laser power. Therefore, for a given phase modulation, the corresponding amplitude modulation is determined. As a result, we are able to consider both the amplitude and phase modulations at the same time by only including the phase modulation factor in the equation (Equation 5.10) for the lens design.

The amplitude and phase modulations were optimised according to the following two criteria. 1): Maximising the constructive interference between all the GO zones and all the rGO zones. 2): Minimising the destructive interference between the adjacent GO and rGO zones. In this way, it is possible to achieve the best focusing/interference condition for a given phase/amplitude modulation to eventually optimise both the focal spot size and the focusing efficiency.

The effective wave vector along the lateral direction which can be formulated as:

$$k_{xy} = k \cdot \sin\theta_m \tag{5.11}$$

Here θ_m is the diffraction angle between the wave vector and the optical axis (See Figure 5.13) of the light from the mth zone (a_m), which can be calculated by the diffraction Equation 5.4 as:

$$\sin\theta_m = \lambda/(a_m - a_{m-1}) \tag{5.12}$$

By substituting Equation 5.12 into Equation 5.11, one can obtain:

$$k_{xy} = 2\pi/(a_{m+1} - a_m) \tag{5.13}$$

which is independent of the incident wavelength.

5.7 Conclusions

Based on the unique and giant refractive index and absorption modulations of the sprayable GO thin film during its laser reduction process, we demonstrate a GO ultrathin (~200 nm) flat lens that shows far-field 3D subwavelength focusing ($\lambda^3/5$) with an absolute focusing efficiency >32% for a broad wavelength range from 400 nm to 1500 nm. Our flexible GO lenses are mechanically robust and maintain excellent focusing properties under high stress. The simple and scalable fabrication approach enables wide potential applications in on-chip nanophotonics. The new wavefront shaping concept with laser patterned GO ultrathin films, provides new and viable solutions for ultralight weight, highly efficient, highly integratable and flexible optical systems, opening up new avenues for various multidisciplinary applications including non-invasive 3D biomedical imaging, laser tweezing, all-optical broadband photonic chips, light harvesting, aerospace photonics, optical microelectromechanical systems and lab-on-chip devices.

Chapter 6

Graphene oxide polariser

As reviewed in Chapter 2, ultrathin polarisers have been extensively studied both theoretically and experimentally including metamaterials, metasurfaces, wire-grid polarisers and guided resonance-based polarisers, as the indispensable elements in integrated optical systems. However, the extinction ratio and the efficiency of the polarisers are greatly restricted by the considerable metallic losses, in particular, in the shorter wavelength ranges for the wire-grid polarisers. Also, the operation wavelength of the guided resonance-based polarisers is greatly limited to 1550 nm due to the conventional available transparent materials in the IR range such as silicon and indium phosphide. Moreover, time consuming and cost-ineffective manufacturing methods are required for both fabrication and deposition of conventional materials such as silicon or metals. As a result, it is still challenging to realise ultrathin polarisers from the visible to the IR ranges with high extinction ratio, high transmission efficiency, flexible and integratable capabilities and cost-effective manufacturing methods.

In this chapter, inspired by the wonderful optical properties of GO and laser-induced rGO, an ultrathin micro-polariser on GO film has been proposed. The optical spectra of the GO film with the periodic C-shape array has been calculated and strong polarisation dependence has been observed based on the guided resonances in 2D PC slabs with asymmetric C-shape structures. A linear ultrathin micro-polariser with high extinction ratio (>3000), one order of magnitude larger than the current guided resonance-based polarisers, has been achieved by carefully designing the GO film thickness, the C-shape opening angle and the radius. Moreover, the operational wavelength of the micro-polariser with high extinction ratio can be turned from the visible (600 nm) to the NIR (1.6 μm) range by modifying the periodicity of the C-shape array thanks to the dispersionless nature of GO. In addition, the polarisation state of the transmitted beam can be dynamically manipulated by simply rotating the micro-polariser. Finally, the incident-angle dependence of the micro-polariser has been investigated and high extinction ratio remains for a wide range of incident angles as large as 30°.

6.1 Achieving high extinction ratio

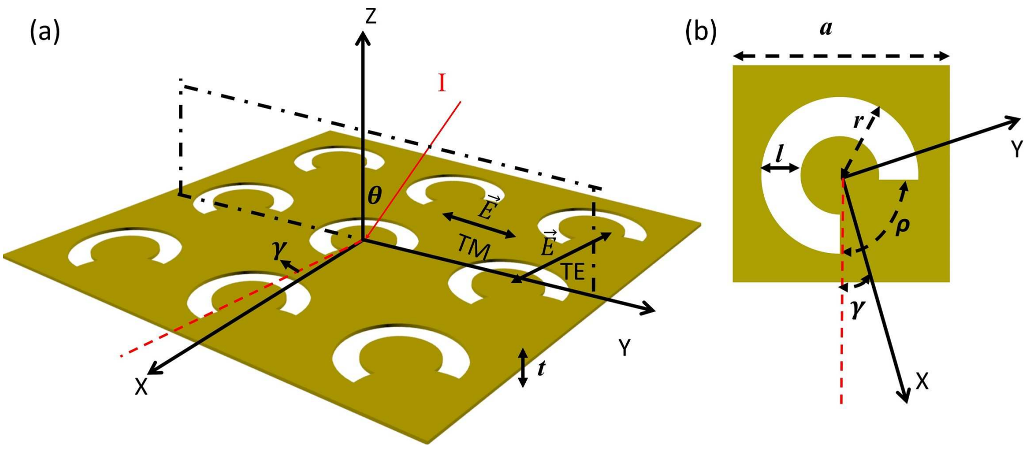

Figure 6.1: (a) Conceptual design for the GO film with 2D periodic C-shape array. The C-shape array is in the x-y plane and the incident light is in the y-z plane with a colatitude angle θ. The geometry of individual C-shape has also been defined in (b).

It has been demonstrated that in the semiconductor materials the incident light can be strongly confined within the PC slab through the out-plane guided resonances, which can significantly influence the transmission or reflection of the externally incident light, resulting in the complex Fano resonant line shapes[146]. The incident energy can go straight through the slab and generate the initial pulse, which is known as the direct transmission process. On the other hand, the remaining portion of the incident energy excites the guided resonances, which is the indirect transmission process. As a result, the transmission property is determined by the interference between the direct and indirect pathways. Also the transmission spectra become asymmetric and can vary from 0 to 100% within a very narrow frequency range. The optical response of 2D structures with a 90° rotational symmetry is independent on the polarisation of the incident exciting wave. However, the normal transmission becomes polarisation sensitive to the incident wave when reducing the rotational symmetry of the periodic structure due to the changing of the coupling time between the two resonant modes, which provides the possibility to achieve the polarisation sensitive devices such as the polariser[158]. Therefore, by introducing the highly asymmetric C-shape array, a micro-polariser on GO thin film is proposed, as shown in Figure 6.1. The polariser is in the x-y plane and the incident light is in the y-z plane. The electric field of the incident light is either perpendicular to the incident plane (TE polarisation) or parallel to the incident plane (TM polarisation). t is the GO film thickness and θ is the colatitude angle of the incident light. The geometry of the C-shape can be defined as a (periodicity), l (linewidth of the C-shape), r (radius of the C-shape), and ρ (the C-shape opening angle), as labelled in Figure 6.1.

The periodic 2D C-shape array (a=1 μm, l=0.3 μm, r=0.33 μm, ρ=180°) on the GO thin film (100 nm) has been firstly designed and the transmission spectra have been calculated for TM and TE polarisations, respectively, as shown in Figure 6.2a. Clearly the asymmetric Fano resonances can be observed for both polarisations, corresponding to the indirect transmission process where the incident energy excites the guided resonances. Also the direct transmission process has been confirmed by the Febry-Perot oscillation of the background. Moreover, by introducing the asymmetric structures (C-shape in our case), the spectra are highly sensitive to the incident polarisation. For example, a high transmission as large as 0.8 for TE polarisation can be observed at $\sim$ 1.3 μm, whereas almost zero transmission is shown at the same wavelength for the TM polarisation due to the strong confinement of the incident light within the PC slab (inset of Figure 6.2a). As a result, the observed strong polarisation

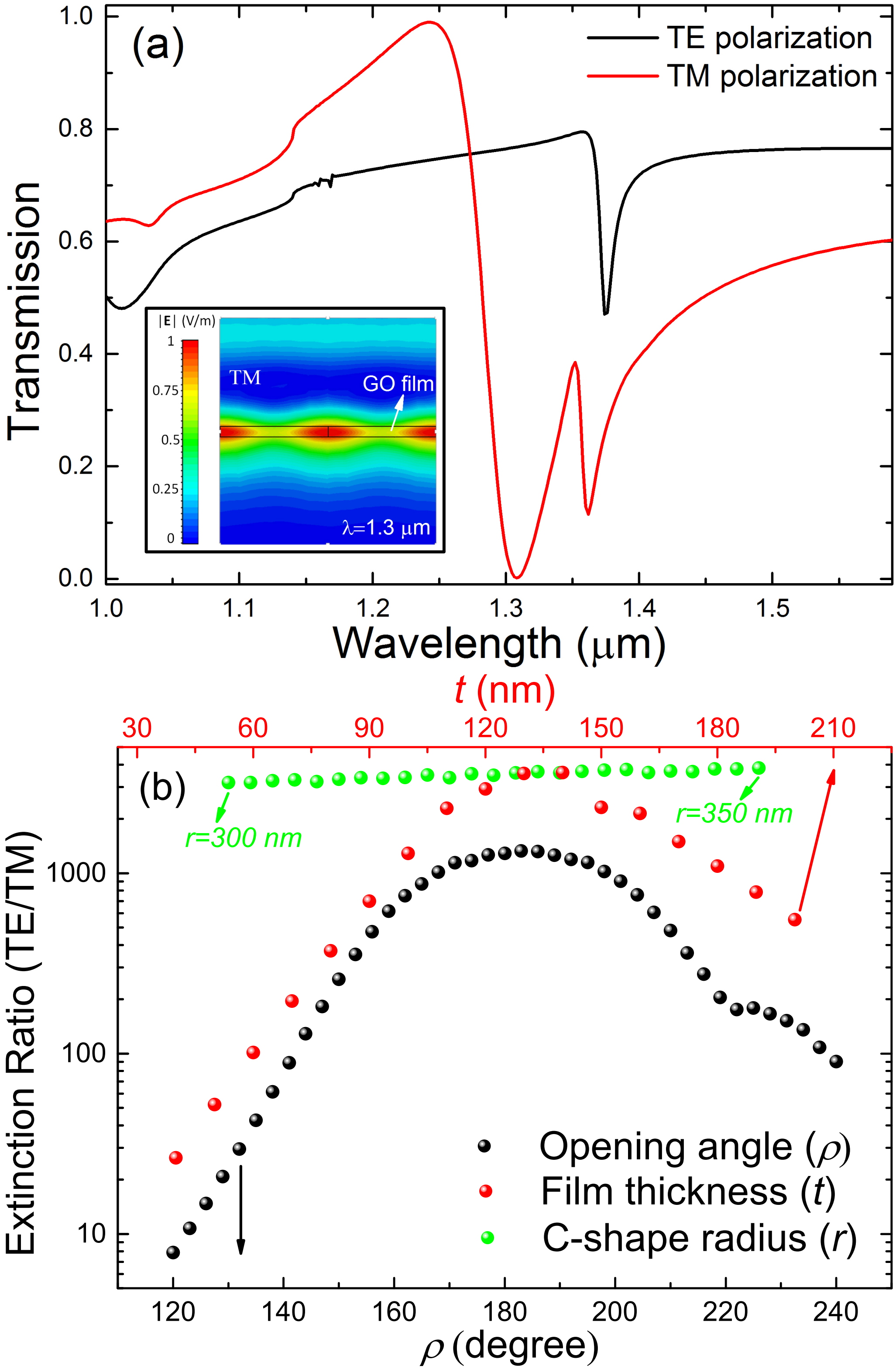

Figure 6.2: (a) The transmission spectra of the proposed GO polariser with TE and TM polarised light incidence. Inset: The strong confinement of the incident light within the PC slab under TM polarisation. (b) The optimisation of the extinction ratio of the micro-polariser by modifying the GO film thickness (t), the C-shape radius (r) and the C-shape opening angle (ρ). The C-shape radius (green dots) is changed from 300 nm to 350 nm with a step of 2 nm.

sensitivity of the guided resonance on our GO thin film can potentially serve as an ultrathin planer polariser.

The TE polarisation extinction ratio of our GO mico-polariser, defined as the ratio of transmittance of the TE incident wave to that of the TM incident wave, has been designed by modifying the film thickness, C-shape opening angle and the radius. Figure 6.2b shows the dependent of the extinction ratio at 1.3 μm on the C-shape geometries including the C-shape opening angel ρ, the film thickness t and the radius r, while the periodicity is fixed at 1 μm. The opening angle ρ is firstly turned from 120° to 240° and the extinction ratio (TE/TM) is found to be larger than 1, indicating that higher transmission can be achieved when the electric field of the incident light is along the effective long edge of the C-shape (x-axis). Moreover, the largest extinction ratio can be optimised at 1000 when ρ=180°, corresponding to the poorest rotational symmetry of the structure. Furthermore, the observed guided resonances is dependent on the thickness of the PC slab, which could affect the confinement of the EM fields within the slab and the coupling efficiency to the external radiation. As a result, the GO film thickness has also been optimised within the range from 30 nm to 210 nm, in which the transmission of GO film are kept over 80% sufficient for practical applications, significantly outperforming the metallic wire-grid or metasurface polarisers. By optimising the GO film thickness at 140 nm, the extinction ratio can be further increased as large as 3600, which exceeds the state-of-the-art ultrathin polarisers based on PC slab guided resonances by one order of magnitude[167]. Finally, the extinction ratio shows little dependence on the radius of individual C-shape structure, indicating the fact that the guided resonances are the coupling between external radiation with the PC modes created by the periodic structures other than the localised modes in the individual structures.

6.2 Broadband tuning of working wavelength

The working wavelength of broadband mirror or polariser based on 2D PC slab is mainly restricted at 1550 nm due to the confinement of the constitution materials such as silicon or indium phosphide. Materials with both high refractive indices and transparency are required to realise the broadband working wavelength range. And few applications of 2D PC slab in the visible range have been reported so far. As a dispersionless material, GO shows a broadband low absorption and a considerable high refractive index from the visible to the IR ranges. Therefore, it is possible to achieve the broadband micro-polariser with our GO film from the visible to the IR ranges.

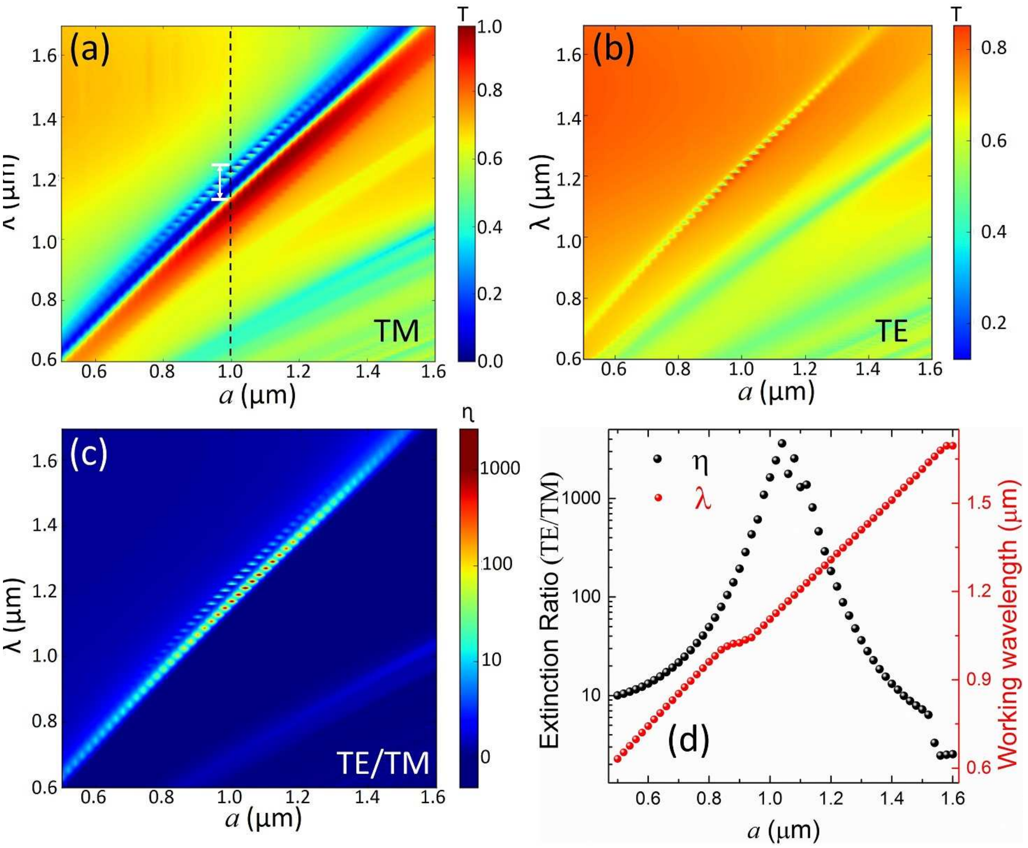

FIGURE 6.3: (a)The dependence of TM transmission on the incident wavelength and the periodicity of the C-shape array. (b)The dependence of TE transmission on the incident wavelength and the periodicity of the C-shape array. (c)The dependence of the extinction ratio on the incident wavelength and the periodicity of the C-shape array, calculated by dividing TE transmission over TM transmission. (d) The tuning of working wavelength by modifying the periodicity and the corresponding extinction ratio of the micro-polariser.

To study the broadband tunability of our GO micro-polariser, the periodicity of the C-shape array is turned from 0.5 μm to 1.6 μm and the transmission under both TE and TM polarisations has been simulated, as shown in Figure 6.3a and Figure 6.3b, respectively. A transmission dip as low as -20 dB can be observed under TM polarisation and is found to shift as the periodicity changes. As a result, it is possible to surpress the TM incident light from the visible (0.6 μm) to the IR (1.7 μm) ranges by continuously tuning the periodicity of the 2D C-shape array.

In comparison, the transmittance of the TE polarised light remains as large as 0.5 in the same wavelength range. The tuning of the periodicity only affects the transmittance of the TE polarised incident light. Therefore, by tuning the periodicity of the C-shape array, we have successfully shifted the transmission dip of TM polarised light while maintaining the transmittance of TE polarised light over a broadband range from the visible to the IR ranges, which makes our GO micro-polariser a potential broadband TE polariser. It should be noted that the transmission dip is narrow banded once the geometry of the C-shape structure is fixed, as marked in Figure 6.3a, which could perform as a high-Q narrow band filter with strong polarisation sensitivity.

To characterise the performance of our GO micro-polariser, the dependence of the extinction ratio (η) on the tuning of periodicity has been calculated by dividing the TE transmission value over the TM transmission value, as shown in Figure 6.3c. Clearly η>1 has been achieved over a broadband range from 600 nm to 1.7 μm by tuning the periodicity of the C-shape array, which is due to the shifting of the TM transmission dip and a large TE transmission, serving as a TE linear polariser with tunable working wavelength from the visible to the NIR range. The extinction ratio at the corresponding working wavelength has been plotted quantitatively as show in Figure 6.3d. The maximum of extinction ratio as large as 3600 has been observed for incident wavelength of 1.14 μm with the periodicity of 1.04 μm. Although the working wavelength can be tuned over a broadband range, modifying the periodicity away from 1.04 μm results in the decrease of the extinction ratio, deteriorating the GO micro-polariser performance. This can be explained by the reducing of TE transmission due to the increased absorption of the GO thin film in the visible range and the reducing of the filling ratio of C-shape structure in the IR range as the increasing of the periodicity. Specifically, the indirect path way from guided resonance in the IR range is reduced, resulting in the decrease of TE transmission.

6.3 Polarisation state tuning of output beam

The polarisation state of the output beam passing through the GO micro-polariser has been studied. By tuning the C-shape rotation angle γ (see Figure 6.1), the polarisation degree of the output beam can be manipulated. Figure 6.4a and Figure 6.4b are the calculated extinction ratio dependence on the C-shape rotation angle (γ) over broadband working wavelength for TE/TM and TM/TE polarisations, respectively. One can see clearly that large extinction ratio is observed for TE polarisation at γ=0 and for TM polarisation at γ=90 due to the rotational symmetry of the C-shape. Moreover, the extinction ratio is found to change when rotating the C-shape structure, resulting in the transition of the output polarisation state from TE polarisation to TM polarisation.

To further understand the dependence of the output polarisation state on the C-shape rotation angle (γ), the polarisation degree (V) has been calculated at 1.14 μm incident light (along the white dashed line in Figure 6.4a,b) and plotted in Figure 6.4c. It is well known that the light is completely polarised when V=1, whereas V equals 0 for unpolarised or natural light. As a result, V is found to close to 1 for γ <30°, indicating that the TE output beam can be obtained. However, V decreases dramatically when γ >30° and reduces to 0 at γ=45°, corresponding to the natural light output. Moreover, the output light is converted to TM polarisation when γ >60°. For conventional polariser, the degree of polarisation changes dramatically with the rotation of the polariser, following the sine function. In comparison, our GO micro-polariser, with the 2D C-shape array, shows the large tolerance of the rotational alignment as large as 30° and also the complete polarisation tuning capability of the output beam.

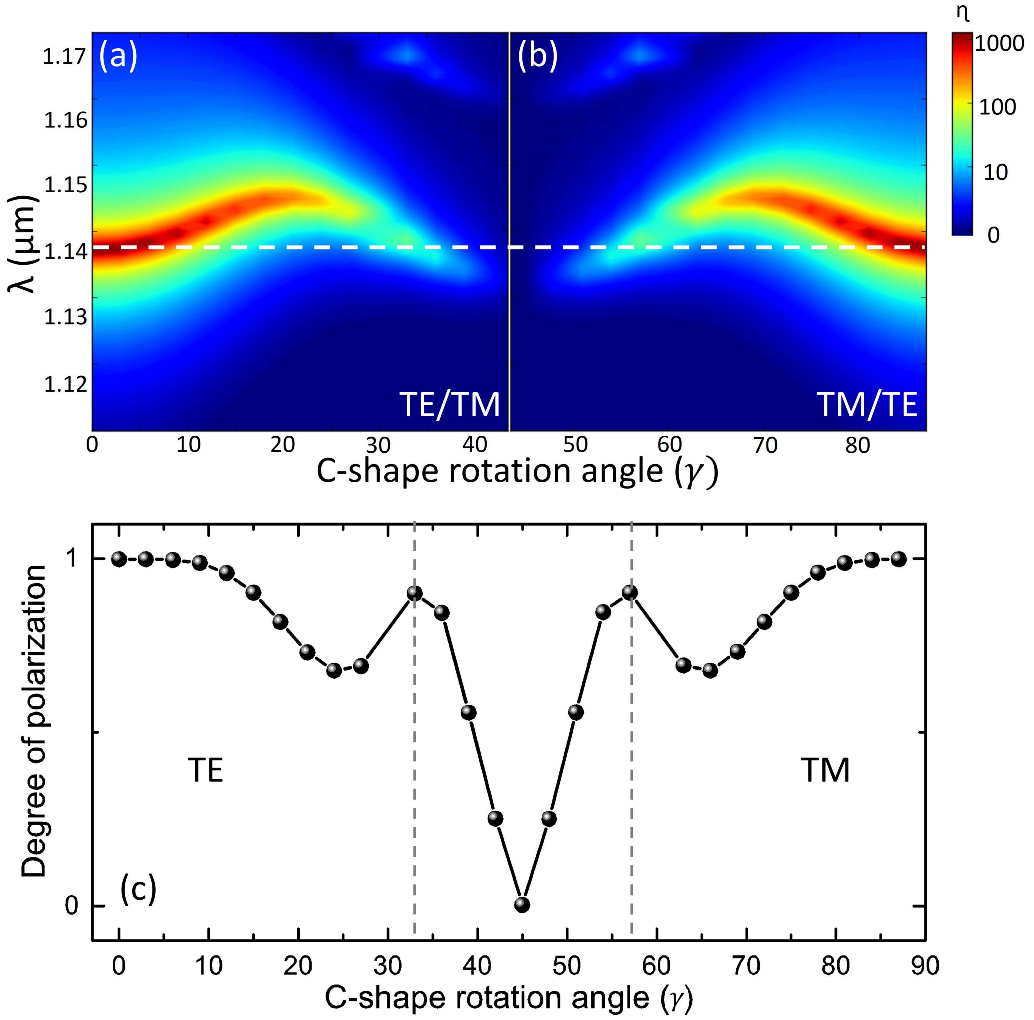

FIGURE 6.4: The dependence of the extinction ratio on the C-shape rotation angle (γ) has been plotted for TE/TM (a) and TM/TE (b) configurations over broadband working wavelength. (c) The degree of polarisation of the output beam has been calculated based on the C-shape rotation angle (γ) at 1.14 μm incident light, as indicated in the white dashed line in (a) and (b).

6.4 Angular dependence of the graphene oxide polariser

From an experimental point of view, an incident beam with a finite cross-section contains multiple angular components. Although large extinction ratio of our GO micro-polariser has been demonstrated at the normal incidence, a realistic characterisation of the polariser should also take into account the incident-angle dependence of the performance. As a result, by changing the colatitude angle θ (see Figure 6.1) from 0° to 50°, the extinction ratio has been calculated, as shown in

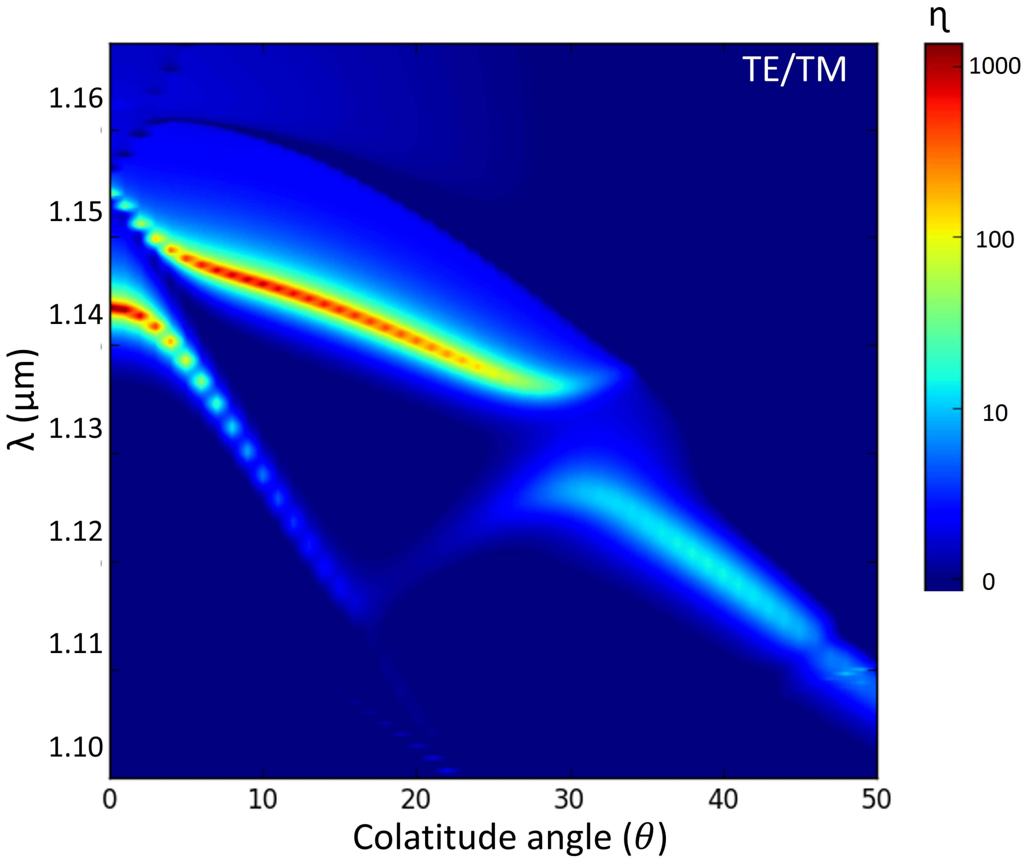

Figure 6.5: The angular dependence of the extinction ratio has been simulated for TE/TM polarisation. The colatitude angle is tuned from 0° to 50°.

Figure 6.5. At the normal incidence, an extinction ratio as large as 3600 has been observed at 1.14 μm incident light for TE/TM polarisations. As the colatitude angle θ increases from 0° to 5°, both the extinction ratio and the wavelength at which the maximum extinction ratio is achieved are found to decrease. While further increasing the colatitude angle θ from 5° to 30°, an additional maximum of extinction ratio is observed around 1.15 μm and blueshifts as θ increases. This can be explained by the phase matching conditions of the guided resonances. In particular, the in-plane wave vector $k_{\|}$ becomes nonzero as the increase of the colatitude angle θ and can be expressed as:

$$k_{\|} = k_0 \cdot \sin\theta,$$

where k_0 is the wave vector of the incident light. Therefore, the transmission dip of the TM polarised light split as θ increases due to the additional phase change that results in the splitting of the Fano resonance or guided resonance modes[159]. On the contrary, less angle dependent transmission of TE polarisation has been observed due to the relatively-unchanged phase matching conditions associated with the relatively flat model dispersion properties[210]. Although the optimal working wavelength of the micro-polariser is found to shift due to the oblique incidence, it is limited within 10 nm bandwidth of shifting. Therefore, we claim that the strong extinction ratio of over 100 remains for a wide range of incident angle as large as 30°, which makes our GO micro-polariser an ideal component for practical and wide incident angle applications.

6.5 Conclusions

In conclusion, we propose an ultrathin GO micro-polariser based on the guided resonances of the 2D PC slab. The optical properties of the 2D C-shape array on the GO thin film are simulated and the extinction ratio of the polariser as high as 3600 has been achieved when the rotational symmetry is largely broken, which exceeds the state-of-the-art ultrathin polarisers based on PC slab guided resonances by one order of magnitude[167]. Also the thickness of the GO thin film is optimised at 100 nm not only to support the guided resonances, but also to reduce the linear absorptions. As a result, the efficiency as large as 80% of the ultrathin GO polariser has been achieved, suppressing the metallic wire-grid or metasurface polarisers. The working wavelength can be tuned over a broadband range from the visible to the IR ranges due to the dispersionless nature of GO, largely extending the current working wavelength range (1.5 μm) using silicon or indium phosphide materials. By rotating the C-shape structure, the polarisation state of the output beam can be maintained over a large rotational angle, providing the large tolerance of the rotational alignment as large as 30°. Finally the dependence of the performance of the polariser on the oblique incidence has been investigated and large extinction ratio can be achieved for a wide range of oblique incident angle as large as 30°. In comparison with the waveguide-based polarisers[211], the proposed GO polariser modulates the polarisation state of a normal incident light, which reduces the transmission losses as that in a waveguide structure. The anisotropic complex dielectric function of GO has also been used to realise a broadband waveguide polariser recently[169]. However, the optical anisotropy is not required in our proposed GO polariser, which makes the concept transferrable to various materials such as the multilayer carbon film. It should be also emphasised that the proposed ultrathin GO polariser can be readily fabricated by using the one-step mask-free DLW method, offering flexible and cost-effective manufacturing capabilities. Therefore, our GO micro-polariser may provide various on-chip photonic applications due to its high efficiency, broadband working wavelength range, large extinction ratio and cost-effective manufacturing.

Chapter 7

Conclusions and outlooks

7.1 Conclusions

This thesis investigates the fundamental optical properties of the GO and laser-induced rGO films, and their applications in the classical optical devices. A wide range of topics have been covered including the experimental and theoretical methods, the physical understanding of the optical responses, and the design and optimisation of the GO optical devices. The major achievements can be summarised as follows:

1. The linear dispersion relations of the GO and laser-induced rGO thin films at various reduction extents have been investigated by using the focused beam spectroscope ellipsometry technique from the visible (200 nm) to the NIR (1.7 μm) ranges. The B-Spline followed by Gen-Osc models have been used to fit the measured values to obtain the KK consistent. The linear dispersion relations can be tuned depending on the reduction parameters (laser powers in our case), and the changing of both refractive index and extinction coefficient are attributed to the removal of interlamellar water and the oxygen functional groups, respectively.

2. For the first time, the KK relations have been used to determine the linear dispersion relations of GO and rGO over the broadband range from the visible (200 nm) to the MIR ranges (up to 24 μm), providing the important missing

information especially in the IR range, which is inaccessible to traditional spectroscope ellipsometry method. The conductivity of GO and rGO has been deduced and fitted with the Lorentz model, indicating the bandgap tuning of GO after the reduction process.

3. Rich and giant nonlinear responses of the GO film during its entire reduction process are unveiled by using the Z-scan measurement. The nonlinear absorption is observed to transit from SA to OL, whereas the nonlinear refractive index is found to transit from self-focusing to self-defocusing. Four distinguished stages with unique nonlinear activities have been demonstrated within the entire laser-induced reduction process of the GO thin film.

4. The hybrid GO-AuNP films have been synthesised by a universal and simple way, the vacuum filtration method. The effective functionalisation of GO with AuNPs has been revealed by both the UV-Vis and FTIR spectra. Enhanced nonlinear absorption and refraction of the hybrid composite have been demonstrated by the Z-scan measurement and found to be monotonically dependent on the AuNP concentration. The enhanced nonlinear light-matter interactions of the hybrid GO-AuNP films can be attributed to the efficient energy and/or charge (electron) transfer upon photoexcitation, and the synergistic coupling effects between AuNPs and GO.

5. A GO ultrathin flat lens has been demonstrated based on the unique and giant refractive index and absorption modulations of the GO thin film during its laser reduction process. The performance of the GO lens has been optimised both theoretically and experimentally, and the far-field 3D subwavelength focusing ($\lambda^3/5$) with an absolute focusing efficiency >32% for a broad wavelength range from 400 nm to 1500 nm has been achieved. In addition, our flexible GO lenses are mechanically robust and maintain excellent focusing properties under high stress. Finally, different diffractive optical elements have been realised on the GO thin film, indicating the novel wavefront shaping capability.

6. An ultrathin GO micro-polariser based on the 2D PC slab guided resonances has been proposed theoretically. The extinction ratio of the polariser as high as

3600 has been achieved by largely reducing the rotational symmetry of the 2D structures. The working wavelength can be tuned over a broadband range from the visible to the IR ranges due to the dispersionless nature of GO. The extinction ratio as a function of the incident angle has been investigated and the excellent polariser performance can be maintained for a wide range of oblique incident angle as large as 30°.

In summary, this thesis presents innovative research on the optics and applications of the GO and laser-induced rGO films. The GO film shows unique properties that are unavailable to conventional materials such as the tunable linear and nonlinear optical properties, a versatile patterning capability by DLW, the surface functionalisation possibility, the wavefront shaping ability, and the mechanical robustness and stress, which are highly demanded for the next generation ultralight weight, highly efficient, highly integratable, and flexible and bendable optical systems, opening up new avenues for various multidisciplinary applications including non-invasive 3D biomedical imaging and sensing, laser tweezing, all-optical broadband photonic chips, light harvesting, aerospace photonics, optical microelectromechanical systems and lab-on-chip devices.

7.2 Outlooks

Although much progress has been made in understanding the optical properties of GO and rGO, there is significantly more to be further explored and exploited.

1. The theoretical modeling of the conductivity of GO and rGO remains challenging due to not only the limited characterisation strategies, but also the complexity of the chemical and atomic structures. Unlike the monolayer graphene, whose conductivity is controlled by electron-hole pair excitations and has been divided into intraband and interband contributions, the conductivity of monolayer GO is strongly dependent on oxygen functional groups including the type, the fraction and their distributions on the basal plane. And it is even challenging for

multilayer GO results from the interlayer water trapping and the coupling and interactions between different GO layers.

2. The interactions between laser and GO needs to be further investigated. Numerous optical and photonic applications have been realised by manipulating the laser parameters including the wavelength, the repetition rate, the polarisation state, the beam distribution, the pulse width, etc. As a result, it is of great interest to link the reduction of GO with the specific laser parameters. Given the fact that the tunable optical properties of rGO is dependent on the reduction extent of GO, the optical properties of rGO can be eventually controlled at will by manipulating the used laser parameters, which offers not only great flexibility in designing various optical components, but also more understandings of the light-material interactions.

3. The transition of GO from insulator to semiconductor or semimetal has not been observed due to the limited reduction extent by using femtosecond pulsed laser beam. It has already been reported that rGO with considerable conductivity can be achieved by using thermal and chemical reduction. As a result, the optimisation of laser parameters needs further efforts for lager reduction extent of GO and the Drude-like conductivity of rGO in the longer wavelength range has not been demonstrated.

4. It is still challenging to realise nonlinear GO or rGO devices due to the significant absorptions especially in the visible range. The possible solution is to explore the out-of-plane (perpendicular to the GO film) applications other than the in-plane devices to reduce the interaction lengths between the incident light and the materials. Also, chemical functionalisation of GO may provide another solution for achieving ultrahigh nonlinearity with less absorption by taking the advantages of both the GO and the decoration materials.

5. More optical components utilising the novel wavefront shaping capabilities are yet to be demonstrated. In addition, the metamaterials and metasurface on GO thin film could also be realised by using the possible plasmonic resonances of rGO in the longer wavelength range.

In conclusion, GO provides an exciting material platform for various scientific disciplines including physics, chemistry, engineering, and materials sciences, providing a unique route towards the next generation flexible and bendable, all-carbon-based thin-film technology. The potentials of GO and rGO in electronic as well as photonic systems need continued involvement of researchers from all fields.

Bibliography

[1] A. Clauss, G. O. Fischer, and U. Hofmann. Dünnste kohlenstoff-folien. *Zeitschrift Für Naturforschung B*, 17(3):150–153, 1962.

[2] J. C. Shelton, H. R. Patil, and J. M. Blakely. Equilibrium segregation of carbon to a nickel (111) surface: A surface phase transition. *Surface Science*, 43(2):493–520, 1974.

[3] J. W. May. Platinum surface leed rings. *Surface Science*, 17(1):267–270, 1969.

[4] H. P. Boehm, R. Setton, and E. Stumpp. Nomenclature and terminology of graphite intercalation compounds. *Carbon*, 24(2):241–245, 1986.

[5] K. S. Novoselov, A. K. Geim, S. V. Morozov, D. Jiang, Y. Zhang, S. V. Dubonos, I. V. Grigorieva, and A. A. Firsov. Electric field effect in atomically thin carbon films. *Science*, 306(5696):666–669, 2004.

[6] K. S. A. Novoselov, A. K. Geim, S. V. b Morozov, D. Jiang, M. Katsnelson, I. V. Grigorieva, S. V. Dubonos, and A. A. Firsov. Two-dimensional gas of massless dirac fermions in graphene. *Nature*, 438(7065):197–200, 2005.

[7] A. K. Geim and K. S. Novoselov. The rise of graphene. *Nature Materials*, 6 (3):183–191, 2007.

[8] S. V. Morozov, K. S. Novoselov, M. I. Katsnelson, F. Schedin, D. C. Elias, J. A. Jaszczak, and A. K. Geim. Giant intrinsic carrier mobilities in graphene and its bilayer. *Physical Review Letters*, 100(1):016602, 2008.

[9] X. Du, I. Skachko, A. Barker, and E. Y. Andrei. Approaching ballistic transport in suspended graphene. *Nature Nanotechnology*, 3(8):491–495, 2008.

[10] K. I. Bolotin, K. J. Sikes, Z. Jiang, M. Klima, G. Fudenberg, J. Hone, P. Kim, and H. L. Stormer. Ultrahigh electron mobility in suspended graphene. *Solid State Communications*, 146(9):351–355, 2008.

[11] Y. Zhang, Y. Tan, H. L. Stormer, and P. Kim. Experimental observation of the quantum hall effect and berry's phase in graphene. *Nature*, 438(7065): 201–204, 2005.

[12] F. Miao, S. Wijeratne, Y. Zhang, U. C. Coskun, W. Bao, and C. N. Lau. Phase-coherent transport in graphene quantum billiards. *Science*, 317(5844): 1530–1533, 2007.

[13] K. S. Novoselov, Z. Jiang, Y. Zhang, S. V. Morozov, H. L. Stormer, U. Zeitler, J. C. Maan, G. S. Boebinger, P. Kim, and A. K. Geim. Room-temperature quantum hall effect in graphene. *Science*, 315(5817):1379–1379, 2007.

[14] S. Pisana, M. Lazzeri, C. Casiraghi, K. S. Novoselov, A. K. Geim, A. C. Ferrari, and F. Mauri. Breakdown of the adiabatic born–oppenheimer approximation in graphene. *Nature Materials*, 6(3):198–201, 2007.

[15] D. L. Miller, K. D. Kubista, G. M. Rutter, M. Ruan, W. A. de Heer, P. N. First, and J. A. Stroscio. Observing the quantization of zero mass carriers in graphene. *Science*, 324(5929):924–927, 2009.

[16] M. I. Katsnelson, K. S. Novoselov, and A. K. Geim. Chiral tunnelling and the klein paradox in graphene. *Nature Physics*, 2(9):620–625, 2006.

[17] A. F. Young and P. Kim. Quantum interference and klein tunnelling in graphene heterojunctions. *Nature Physics*, 5(3):222–226, 2009.

[18] C. Lee, X. Wei, J. W. Kysar, and J. Hone. Measurement of the elastic properties and intrinsic strength of monolayer graphene. *Science*, 321(5887): 385–388, 2008.

[19] A. A. Balandin, S. Ghosh, W. Bao, I. Calizo, D. Teweldebrhan, F. Miao, and C. N. Lau. Superior thermal conductivity of single-layer graphene. *Nano Letters*, 8(3):902–907, 2008.

[20] F. Schedin, A. K. Geim, S. V. Morozov, E. W. Hill, P. Blake, M. I. Katsnelson, and K. S. Novoselov. Detection of individual gas molecules adsorbed on graphene. *Nature Materials*, 6(9):652–655, 2007.

[21] R. R. Nair, P. Blake, A. N. Grigorenko, K. S. Novoselov, T. J. Booth, T. Stauber, N. M. R. Peres, and A. K. Geim. Fine structure constant defines visual transparency of graphene. *Science*, 320(5881):1308–1308, 2008.

[22] P. Matyba, H. Yamaguchi, G. Eda, M. Chhowalla, L. Edman, and N. D. Robinson. Graphene and mobile ions: the key to all-plastic, solution-processed light-emitting devices. *ACS Nano*, 4(2):637–642, 2010.

[23] X. Wang, L. Zhi, and K. Müllen. Transparent, conductive graphene electrodes for dye-sensitized solar cells. *Nano Letters*, 8(1):323–327, 2008.

[24] S. Bae, H. Kim, Y. Lee, X. Xu, J. Park, Y. Zheng, J. Balakrishnan, T. Lei, H. R. Kim, and Y. I. Song. Roll-to-roll production of 30-inch graphene films for transparent electrodes. *Nature Nanotechnology*, 5(8):574–578, 2010.

[25] F. Xia, T. Mueller, Y. Lin, A. Valdes-Garcia, and P. Avouris. Ultrafast graphene photodetector. *Nature Nanotechnology*, 4(12):839–843, 2009.

[26] T. Mueller, F. Xia, and P. Avouris. Graphene photodetectors for high-speed optical communications. *Nature Photonics*, 4(5):297–301, 2010.

[27] Z. Sun, T. Hasan, F. Torrisi, D. Popa, G. Privitera, F. Wang, F. Bonaccorso, D. M. Basko, and A. C. Ferrari. Graphene mode-locked ultrafast laser. *ACS Nano*, 4(2):803–810, 2010.

[28] K. S. Kim, Y. Zhao, H. Jang, S. Y. Lee, J. M. Kim, K. S. Kim, J. Ahn, P. Kim, J. Choi, and B. H. Hong. Large-scale pattern growth of graphene films for stretchable transparent electrodes. *Nature*, 457(7230):706–710, 2009.

[29] X. Li, W. Cai, J. An, S. Kim, J. Nah, D. Yang, R. Piner, A. Velamakanni, I. Jung, and E. Tutuc. Large-area synthesis of high-quality and uniform graphene films on copper foils. *Science*, 324(5932):1312–1314, 2009.

[30] A. Reina, X. Jia, J. Ho, D. Nezich, H. Son, V. Bulovic, M. S. Dresselhaus, and J. Kong. Large area, few-layer graphene films on arbitrary substrates by chemical vapor deposition. *Nano Letters*, 9(1):30–35, 2008.

[31] Z. Sun, Z. Yan, J. Yao, E. Beitler, Y. Zhu, and J. M. Tour. Growth of graphene from solid carbon sources. *Nature*, 468(7323):549–552, 2010.

[32] G. Ruan, Z. Sun, Z. Peng, and J. M. Tour. Growth of graphene from food, insects, and waste. *ACS Nano*, 5(9):7601–7607, 2011.

[33] Z. Peng, Z. Yan, Z. Sun, and J. M. Tour. Direct growth of bilayer graphene on sio2 substrates by carbon diffusion through nickel. *ACS Nano*, 5(10): 8241–8247, 2011.

[34] Z. Yan, Z. Peng, Z. Sun, J. Yao, Y. Zhu, Z. Liu, P. M. Ajayan, and J. M. Tour. Growth of bilayer graphene on insulating substrates. *ACS Nano*, 5 (10):8187–8192, 2011.

[35] N. Behabtu, J. R. Lomeda, M. J. Green, A. L. Higginbotham, A. Sinitskii, D. V. Kosynkin, D. Tsentalovich, A. N. G. Parra-Vasquez, J. Schmidt, and E. Kesselman. Spontaneous high-concentration dispersions and liquid crystals of graphene. *Nature Nanotechnology*, 5(6):406–411, 2010.

[36] D. V. Kosynkin, A. L. Higginbotham, A. Sinitskii, J. R. Lomeda, A. Dimiev, B. K. Price, and J. M. Tour. Longitudinal unzipping of carbon nanotubes to form graphene nanoribbons. *Nature*, 458(7240):872–876, 2009.

[37] D. V. Kosynkin, W. Lu, A. Sinitskii, G. Pera, Z. Sun, and J. M. Tour. Highly conductive graphene nanoribbons by longitudinal splitting of carbon nanotubes using potassium vapor. *ACS Nano*, 5(2):968–974, 2011.

[38] A. Lerf, H. He, M. Forster, and J. Klinowski. Structure of graphite oxide revisited——. *The Journal of Physical Chemistry B*, 102(23):4477–4482, 1998.

[39] V. Strong, S. Dubin, M. F. El-Kady, A. Lech, Y. Wang, B. H. Weiller, and R. B. Kaner. Patterning and electronic tuning of laser scribed graphene for flexible all-carbon devices. *ACS Nano*, 6(2):1395–1403, 2012.

[40] H. He, J. Klinowski, M. Forster, and A. Lerf. A new structural model for graphite oxide. *Chemical Physics Letters*, 287(1):53–56, 1998.

[41] H. C. Schniepp, J. Li, M. J. McAllister, H. Sai, M. Herrera-Alonso, D. H. Adamson, R. K. Prud'homme, R. Car, D. A. Saville, and I. A. Aksay. Functionalized single graphene sheets derived from splitting graphite oxide. *The Journal of Physical Chemistry B*, 110(17):8535–8539, 2006.

[42] D. R. Dreyer, S. Park, C. W. Bielawski, and R. S. Ruoff. The chemistry of graphene oxide. *Chemical Society Reviews*, 39(1):228–240, 2010.

[43] B. Partoens and F. M. Peeters. From graphene to graphite: Electronic structure around the k point. *Physical Review B*, 74(7):075404, 2006.

[44] J. Robertson. Diamond-like amorphous carbon. *Materials Science and Engineering: R: Reports*, 37(4):129–281, 2002.

[45] J. I. Paredes, S. Villar-Rodil, P. Solis-Fernandez, A. Martinez-Alonso, and J. M. D. Tascon. Atomic force and scanning tunneling microscopy imaging of graphene nanosheets derived from graphite oxide. *Langmuir*, 25(10):5957–5968, 2009.

[46] M. F. Islam, E. Rojas, D. M. Bergey, A. T. Johnson, and A. G. Yodh. High weight fraction surfactant solubilization of single-wall carbon nanotubes in water. *Nano Letters*, 3(2):269–273, 2003.

[47] D. Li, M. B. Mueller, S. Gilje, R. B. Kaner, and G. G. Wallace. Processable aqueous dispersions of graphene nanosheets. *Nature Nanotechnology*, 3(2): 101–105, 2008.

[48] C. Mattevi, G. Eda, S. Agnoli, S. Miller, K. A. Mkhoyan, O. Celik, D. Mastrogiovanni, G. Granozzi, E. Garfunkel, and M. Chhowalla. Evolution of electrical, chemical, and structural properties of transparent and conducting chemically derived graphene thin films. *Advanced Functional Materials*, 19(16):2577, 2009.

[49] H. A. Becerril, J. Mao, Z. Liu, R. M. Stoltenberg, Z. Bao, and Y. Chen. Evaluation of solution-processed reduced graphene oxide films as transparent conductors. *ACS Nano*, 2(3):463–470, 2008.

[50] I. Jung, D. A. Dikin, R. D Piner, and R. S. Ruoff. Tunable electrical conductivity of individual graphene oxide sheets reduced at low temperatures. *Nano Letters*, 8(12):4283–4287, 2008.

[51] M. Jin, H. Jeong, W. J. Yu, D. J. Bae, B. R. Kang, and Y. H. Lee. Graphene oxide thin film field effect transistors without reduction. *Journal of Physics D: Applied Physics*, 42(13):135109, 2009.

[52] S. Wang, P. K. Ang, Z. Wang, A. L. L. Tang, J. T. L. Thong, and K. P. Loh. High mobility, printable, and solution-processed graphene electronics. *Nano Letters*, 10(1):92–98, 2009.

[53] G. E. Pike and C. H. Seager. Percolation and conductivity: A computer study. i. *Physical Review B*, 10(4):1421, 1974.

[54] K. P. Loh, Q. Bao, G. Eda, and M. Chhowalla. Graphene oxide as a chemically tunable platform for optical applications. *Nature Chemistry*, 2 (12):1015–1024, 2010.

[55] J. Li, L. Hu, L. Wang, Y. Zhou, G. Grüner, and T. J. Marks. Organic light-emitting diodes having carbon nanotube anodes. *Nano Letters*, 6(11): 2472–2477, 2006.

[56] J. Lee, S. T. Connor, Y. Cui, and P. Peumans. Solution-processed metal nanowire mesh transparent electrodes. *Nano Letters*, 8(2):689–692, 2008.

[57] V. C. Tung, L. Chen, M. J. Allen, J. K. Wassei, K. Nelson, R. B. Kaner, and Y. Yang. Low-temperature solution processing of graphene- carbon nanotube hybrid materials for high-performance transparent conductors. *Nano Letters*, 9(5):1949–1955, 2009.

[58] H. Shin, K. K. Kim, A. Benayad, S. Yoon, H. K. Park, I. Jung, M. H. Jin, H. Jeong, J. M. Kim, and J. Choi. Efficient reduction of graphite oxide by sodium borohydride and its effect on electrical conductance. *Advanced Functional Materials*, 19(12):1987–1992, 2009.

[59] W. Gao, L. B. Alemany, L. Ci, and P. M. Ajayan. New insights into the structure and reduction of graphite oxide. *Nature Chemistry*, 1(5):403–408, 2009.

[60] G. Eda, Y. Lin, S. Miller, C. Chen, W. Su, and M. Chhowalla. Transparent and conducting electrodes for organic electronics from reduced graphene oxide. *Applied Physics Letters*, 92(23):233305, 2008.

[61] G. Zhou, F. Li, and H. Cheng. Progress in flexible lithium batteries and future prospects. *Energy & Environmental Science*, 7(4):1307–1338, 2014.

[62] G. Eda, G. Fanchini, and M. Chhowalla. Large-area ultrathin films of reduced graphene oxide as a transparent and flexible electronic material. *Nature Nanotechnology*, 3(5):270–274, 2008.

[63] S. H. Lee, H. W. Kim, J. O. Hwang, W. J. Lee, J. Kwon, C. W. Bielawski, R. S. Ruoff, and S. O. Kim. Three-dimensional self-assembly of graphene oxide platelets into mechanically flexible macroporous carbon films. *Angewandte Chemie International Edition*, 49(52):10084–10088, 2010.

[64] Q. He, S. Wu, S. Gao, X. Cao, Z. Yin, H. Li, P. Chen, and H. Zhang. Transparent, flexible, all-reduced graphene oxide thin film transistors. *ACS Nano*, 5(6):5038–5044, 2011.

[65] J. Liu, Z. Yin, X. Cao, F. Zhao, L. Wang, W. Huang, and H. Zhang. Fabrication of flexible, all-reduced graphene oxide non-volatile memory devices. *Advanced Materials*, 25(2):233–238, 2013.

[66] X. Sun, Z. Liu, K. Welsher, J. T. Robinson, A. Goodwin, S. Zaric, and H. Dai. Nano-graphene oxide for cellular imaging and drug delivery. *Nano Research*, 1(3):203–212, 2008.

[67] Z. Liu, J. T. Robinson, X. Sun, and H. Dai. Pegylated nanographene oxide for delivery of water-insoluble cancer drugs. *Journal of the American Chemical Society*, 130(33):10876–10877, 2008.

[68] Z. Luo, P. M. Vora, E. J. Mele, A. T. C. Johnson, and J. M. Kikkawa. Photoluminescence and band gap modulation in graphene oxide. *Applied Physics Letters*, 94(11):111909, 2009.

[69] G. Eda, Y. Lin, C. Mattevi, H. Yamaguchi, H. Chen, I. Chen, C. Chen, and M. Chhowalla. Blue photoluminescence from chemically derived graphene oxide. *Advanced Materials*, 22(4):505, 2010.

[70] T. V. Cuong, V. H. Pham, Q. T. Tran, S. H. Hahn, J. S. Chung, E. W. Shin, and E. J. Kim. Photoluminescence and raman studies of graphene thin films prepared by reduction of graphene oxide. *Materials Letters*, 64(3):399–401, 2010.

[71] K. S. Subrahmanyam, P. Kumar, A. Nag, and C. N. R. Rao. Blue light emitting graphene-based materials and their use in generating white light. *Solid State Communications*, 150(37):1774–1777, 2010.

[72] J. Chen and X. Yan. A dehydration and stabilizer-free approach to production of stable water dispersions of graphene nanosheets. *Journal of Materials Chemistry*, 20(21):4328–4332, 2010.

[73] K. Yang, S. Zhang, G. Zhang, X. Sun, S. Lee, and Z. Liu. Graphene in mice: ultrahigh in vivo tumor uptake and efficient photothermal therapy. *Nano Letters*, 10(9):3318–3323, 2010.

[74] J. Kim, L. J. Cote, F. Kim, and J. Huang. Visualizing graphene based sheets by fluorescence quenching microscopy. *Journal of the American Chemical Society*, 132(1):260–267, 2009.

[75] J. Kim, F. Kim, and J. Huang. Seeing graphene-based sheets. *Materials Today*, 13(3):28–38, 2010.

[76] H. Dong, W. Gao, F. Yan, H. Ji, and H. Ju. Fluorescence resonance energy transfer between quantum dots and graphene oxide for sensing biomolecules. *Analytical Chemistry*, 82(13):5511–5517, 2010.

[77] C. Lu, H. Yang, C. Zhu, X. Chen, and G. Chen. A graphene platform for sensing biomolecules. *Angewandte Chemie*, 121(26):4879–4881, 2009.

[78] S. He, B. Song, D. Li, C. Zhu, W. Qi, Y. Wen, L. Wang, S. Song, H. Fang, and C. Fan. A graphene nanoprobe for rapid, sensitive, and multicolor fluorescent dna analysis. *Advanced Functional Materials*, 20(3):453–459, 2010.

[79] A. H. Castro Neto, F. Guinea, N. M. R. Peres, K. S. Novoselov, and A. K. Geim. The electronic properties of graphene. *Reviews of Modern Physics*, 81(1):109, 2009.

[80] I. Jung, M. Pelton, R. Piner, D. A. Dikin, S. Stankovich, S. Watcharotone, M. Hausner, and R. S. Ruoff. Simple approach for high-contrast optical imaging and characterization of graphene-based sheets. *Nano Letters*, 7(12): 3569–3575, 2007.

[81] H. Yang, H. Hu, Y. Wang, and T. Yu. Rapid and non-destructive identification of graphene oxide thickness using white light contrast spectroscopy. *Carbon*, 52:528–534, 2013.

[82] J. T. Hong, K. M. Lee, B. H. Son, S. J. Park, D. J. Park, J. Park, S. Lee, and Y. H. Ahn. Terahertz conductivity of reduced graphene oxide films. *Optics Express*, 21(6):7633–7640, 2013.

[83] I. Jung, M. Vaupel, M. Pelton, R. Piner, D. A. Dikin, S. Stankovich, J. An, and R. S. Ruoff. Characterization of thermally reduced graphene oxide by

imaging ellipsometry. *The Journal of Physical Chemistry C*, 112(23):8499–8506, 2008.

[84] Y. Shen, P. Zhou, Q. Q. Sun, L. Wan, J. Li, L. Y. Chen, D. W. Zhang, and X. B. Wang. Optical investigation of reduced graphene oxide by spectroscopic ellipsometry and the band-gap tuning. *Applied Physics Letters*, 99(14):141911, 2011.

[85] Y. Shen, S. Yang, P. Zhou, Q. Sun, P. Wang, L. Wan, J. Li, L. Chen, X. Wang, and S. Ding. Evolution of the band-gap and optical properties of graphene oxide with controllable reduction level. *Carbon*, 62:157–164, 2013.

[86] Z. H. Ni, H. M. Wang, J. Kasim, H. M. Fan, T. Yu, Y. H. Wu, Y. P. Feng, and Z. X. Shen. Graphene thickness determination using reflection and contrast spectroscopy. *Nano Letters*, 7(9):2758–2763, 2007.

[87] P. Blake, E. W. Hill, A. H. Castro Neto, K. S. Novoselov, D. Jiang, R. Yang, T. J. Booth, and A. K. Geim. Making graphene visible. *Applied Physics Letters*, 91(6):063124, 2007.

[88] X. Wang, Y. P. Chen, and D. D. Nolte. Strong anomalous optical dispersion of graphene: complex refractive index measured by picometrology. *Optics Express*, 16(26):22105–22112, 2008.

[89] A. Gray, M. Balooch, S. Allegret, S. De Gendt, and W. Wang. Optical detection and characterization of graphene by broadband spectrophotometry. *Journal of Applied Physics*, 104(5):053109, 2008.

[90] F. J. Nelson, V. K. Kamineni, T. Zhang, E. S. Comfort, J. U. Lee, and A. C. Diebold. Optical properties of large-area polycrystalline chemical vapor deposited graphene by spectroscopic ellipsometry. *Applied Physics Letters*, 97(25):253110, 2010.

[91] J. W. Weber, V. E. Calado, and M. C. M. Van de Sanden. Optical constants of graphene measured by spectroscopic ellipsometry. *Applied Physics Letters*, 97(9):091904, 2010.

[92] U. Wurstbauer, C. Röling, U. Wurstbauer, W. Wegscheider, M. Vaupel, P. H. Thiesen, and D. Weiss. Imaging ellipsometry of graphene. *arXiv preprint arXiv:1008.3206*, 2010.

[93] V. G. Kravets, A. N. Grigorenko, R. R. Nair, P. Blake, S. Anissimova, K. S. Novoselov, and A. K. Geim. Spectroscopic ellipsometry of graphene and an exciton-shifted van hove peak in absorption. *Physical Review B*, 81(15): 155413, 2010.

[94] M. Dressel and G. Grüner. *Electrodynamics of solids: optical properties of electrons in matter.* Cambridge University Press, 2002.

[95] C. Liu, Y. Chang, T. B. Norris, and Z. Zhong. Graphene photodetectors with ultra-broadband and high responsivity at room temperature. *Nature Nanotechnology*, 9(4):273–278, 2014.

[96] Z. Fei, A. S. Rodin, G. Andreev, W. Bao, A. S. McLeod, M. Wagner, L. M. Zhang, Z. Zhao, M. Thiemens, and G. Dominguez. Gate-tuning of graphene plasmons revealed by infrared nano-imaging. *Nature*, 487(7405):82–85, 2012.

[97] R. L. Sutherland. *Handbook of nonlinear optics.* CRC press, 2003.

[98] Z. Liu, Y. Wang, X. Zhang, Y. Xu, Y. Chen, and J. Tian. Nonlinear optical properties of graphene oxide in nanosecond and picosecond regimes. *Applied Physics Letters*, 94(2):021902, 2009.

[99] X. Jiang, L. Polavarapu, Shu T. Neo, T. Venkatesan, and Q. Xu. Graphene oxides as tunable broadband nonlinear optical materials for femtosecond laser pulses. *The Journal of Physical Chemistry Letters*, 3(6):785–790, 2012.

[100] N. Liaros, P. Aloukos, A. Kolokithas-Ntoukas, A. Bakandritsos, T. Szabo, R. Zboril, and S. Couris. Nonlinear optical properties and broadband optical power limiting action of graphene oxide colloids. *The Journal of Physical Chemistry C*, 117(13):6842–6850, 2013.

[101] X. Zhang, Z. Liu, X. Li, Q. Ma, X. Chen, J. Tian, Y. Xu, and Y. Chen. Transient thermal effect, nonlinear refraction and nonlinear absorption

properties of graphene oxide sheets in dispersion. *Optics Express*, 21(6): 7511–7520, 2013.

[102] V. Nalla, L. Polavarapu, K. K. Manga, B. M. Goh, K. P. Loh, Q. Xu, and W. Ji. Transient photoconductivity and femtosecond nonlinear optical properties of a conjugated polymer–graphene oxide composite. *Nanotechnology*, 21(41):415203, 2010.

[103] P. Chantharasupawong, R. Philip, N. T. Narayanan, P. M. Sudeep, A. Mathkar, P. M. Ajayan, and J. Thomas. Optical power limiting in fluorinated graphene oxide: an insight into the nonlinear optical properties. *The Journal of Physical Chemistry C*, 116(49):25955–25961, 2012.

[104] N. Liaros, K. Iliopoulos, M. M. Stylianakis, E. Koudoumas, and S. Couris. Optical limiting action of few layered graphene oxide dispersed in different solvents. *Optical Materials*, 36(1):112–117, 2013.

[105] M. Feng, H. Zhan, and Y. Chen. Nonlinear optical and optical limiting properties of graphene families. *Applied Physics Letters*, 96(3):033107, 2010.

[106] M. Ren, B. Jia, J. Ou, E. Plum, J. Zhang, K. F. MacDonald, A. E. Nikolaenko, J. Xu, M. Gu, and N. I. Zheludev. Nanostructured plasmonic medium for terahertz bandwidth all-optical switching. *Advanced Materials*, 23(46):5540–5544, 2011.

[107] B. Jia, D. Buso, J. Van Embden, J. Li, and M. Gu. Highly nonlinear quantum dot doped nanocomposites for functional three-dimensional structures generated by two-photon polymerization. *Advanced Materials*, 22 (22):2463–2467, 2010.

[108] R. L. Sutherland and F. K. Hopkins. Handbook of nonlinear optics. *Optical Engineering*, 36(3):964–964, 1997.

[109] Z. Wang, W. Guo, L. Li, B. Luk'yanchuk, A. Khan, Z. Liu, Z. Chen, and M. Hong. Optical virtual imaging at 50 nm lateral resolution with a white-light nanoscope. *Nature Communications*, 2:218, 2011.

[110] D. Lu and Z. Liu. Hyperlenses and metalenses for far-field super-resolution imaging. *Nature Communications*, 3, 2012.

[111] S. W. Hell. Toward fluorescence nanoscopy. *Nature Biotechnology*, 21(11): 1347–1355, 2003.

[112] J. B. Pendry. Negative refraction makes a perfect lens. *Physical Review Letters*, 85(18):3966, 2000.

[113] Z. Liu, J. M. Steele, W. Srituravanich, Y. Pikus, C. Sun, and X. Zhang. Focusing surface plasmons with a plasmonic lens. *Nano Letters*, 5(9):1726–1729, 2005.

[114] N. Fang, H. Lee, C. Sun, and X. Zhang. Sub–diffraction-limited optical imaging with a silver superlens. *Science*, 308(5721):534–537, 2005.

[115] J. Y. Lee, B. H. Hong, W. Y. Kim, S. K. Min, Y. Kim, M. V. Jouravlev, R. Bose, K. S. Kim, I. Hwang, and L. J. Kaufman. Near-field focusing and magnification through self-assembled nanoscale spherical lenses. *Nature*, 460 (7254):498–501, 2009.

[116] S. Ishii, V. M. Shalaev, and A. V. Kildishev. Holey-metal lenses: sieving single modes with proper phases. *Nano Letters*, 13(1):159–163, 2012.

[117] F. Aieta, P. Genevet, M. A. Kats, N. Yu, R. Blanchard, Z. Gaburro, and F. Capasso. Aberration-free ultrathin flat lenses and axicons at telecom wavelengths based on plasmonic metasurfaces. *Nano Letters*, 12(9):4932–4936, 2012.

[118] X. Ni, S. Ishii, A. V. Kildishev, and V. M. Shalaev. Ultra-thin, planar, babinet-inverted plasmonic metalenses. *Light: Science & Applications*, 2(4): e72, 2013.

[119] K. Lee, W. Wagermaier, A. Masic, K. P. Kommareddy, M. Bennet, I. Manjubala, S. Lee, S. B. Park, H. Cölfen, and P. Fratzl. Self-assembly of amorphous calcium carbonate microlens arrays. *Nature Communications*, 3: 725, 2012.

[120] R. Rajasekharan, H. Butt, Q. Dai, T. D. Wilkinson, and G. A. J. Amaratunga. Can nanotubes make a lens array? *Advanced Materials*, 24 (23):OP170–OP173, 2012.

[121] R. Yang, W. Tang, and Y. Hao. A broadband zone plate lens from transformation optics. *Optics Express*, 19(13):12348–12355, 2011.

[122] E. Hecht. *Optics*. Addison-Wesley, 2002. ISBN 9780805385663. URL `https://books.google.com.au/books?id=7aG6QgAACAAJ`.

[123] L. Verslegers, P. B. Catrysse, Z. Yu, J. S. White, E. S. Barnard, M. L. Brongersma, and S. Fan. Planar lenses based on nanoscale slit arrays in a metallic film. *Nano Letters*, 9(1):235–238, 2008.

[124] L. Lin, X. M. Goh, L. P. McGuinness, and A. Roberts. Plasmonic lenses formed by two-dimensional nanometric cross-shaped aperture arrays for fresnel-region focusing. *Nano Letters*, 10(5):1936–1940, 2010.

[125] A. Pors, M. G. Nielsen, R. L. Eriksen, and S. I. Bozhevolnyi. Broadband focusing flat mirrors based on plasmonic gradient metasurfaces. *Nano Letters*, 13(2):829–834, 2013.

[126] X. Chen, L. Huang, H. Mühlenbernd, G. Li, B. Bai, Q. Tan, G. Jin, C. Qiu, S. Zhang, and T. Zentgraf. Dual-polarity plasmonic metalens for visible light. *Nature Communications*, 3:1198, 2012.

[127] D. Hu, X. Wang, S. Feng, J. Ye, W. Sun, Q. Kan, P. J. Klar, and Y. Zhang. Ultrathin terahertz planar elements. *Advanced Optical Materials*, 1(2):186–191, 2013.

[128] F. M. Huang, T. S. Kao, V. A. Fedotov, Y. Chen, and N. I. Zheludev. Nanohole array as a lens. *Nano Letters*, 8(8):2469–2472, 2008.

[129] E. T. F. Rogers, J. Lindberg, T. Roy, S. Savo, J. E. Chad, M. R. Dennis, and N. I Zheludev. A super-oscillatory lens optical microscope for subwavelength imaging. *Nature Materials*, 11(5):432–435, 2012.

[130] F. He, Y. Cheng, L. Qiao, C. Wang, Z. Xu, K. Sugioka, K. Midorikawa, and J. Wu. Two-photon fluorescence excitation with a microlens fabricated on the fused silica chip by femtosecond laser micromachining. *Applied Physics Letters*, 96(4):041108, 2010.

[131] H. Ren, Y. Fan, and S. Wu. Tunable fresnel lens using nanoscale polymer-dispersed liquid crystals. *Applied Physics Letters*, 83(8):1515–1517, 2003.

[132] P. Srisungsitthisunti, O. K. Ersoy, and X. Xu. Volume fresnel zone plates fabricated by femtosecond laser direct writing. *Applied Physics Letters*, 90 (1):011104, 2007.

[133] R. M. Vázquez, S. M. Eaton, R. Ramponi, G. Cerullo, and R. Osellame. Fabrication of binary fresnel lenses in pmma by femtosecond laser surface ablation. *Optics Express*, 19(12):11597–11604, 2011.

[134] K. Yamada, W. Watanabe, Y. Li, K. Itoh, and J. Nishii. Multilevel phase-type diffractive lenses in silica glass induced by filamentation of femtosecond laser pulses. *Optics Letters*, 29(16):1846–1848, 2004.

[135] W. Watanabe, D. Kuroda, K. Itoh, and J. Nishii. Fabrication of fresnel zone plate embedded in silica glass by femtosecond laser pulses. *Optics Express*, 10(19):978–983, 2002.

[136] E. Bricchi, J. D. Mills, P. G. Kazansky, B. G. Klappauf, and J. J. Baumberg. Birefringent fresnel zone plates in silica fabricated by femtosecond laser machining. *Optics Letters*, 27(24):2200–2202, 2002.

[137] R. G. Mote, S. F. Yu, A. Kumar, W. Zhou, and X. F. Li. Experimental demonstration of near-field focusing of a phase micro-fresnel zone plate (fzp) under linearly polarized illumination. *Applied Physics B*, 102(1):95–100, 2011.

[138] H. Gao, J. K. Hyun, M. H. Lee, J. Yang, L. J. Lauhon, and T. W. Odom. Broadband plasmonic microlenses based on patches of nanoholes. *Nano Letters*, 10(10):4111–4116, 2010.

[139] X. Zhang, Z. Tian, W. Yue, J. Gu, S. Zhang, J. Han, and W. Zhang. Broadband terahertz wave deflection based on c-shape complex metamaterials with phase discontinuities. *Advanced Materials*, 25(33):4567–4572, 2013.

[140] X. Chen, L. Huang, H. Mühlenbernd, G. Li, B. Bai, Q. Tan, G. Jin, C. Qiu, T. Zentgraf, and S. Zhang. Reversible three-dimensional focusing of visible light with ultrathin plasmonic flat lens. *Advanced Optical Materials*, 1(7): 517–521, 2013.

[141] L. Huang, X. Chen, H. Muhlenbernd, G. Li, B. Bai, Q. Tan, G. Jin, T. Zentgraf, and S. Zhang. Dispersionless phase discontinuities for controlling light propagation. *Nano Letters*, 12(11):5750–5755, 2012.

[142] A. V. Rogacheva, V. A. Fedotov, A. S. Schwanecke, and N. I. Zheludev. Giant gyrotropy due to electromagnetic-field coupling in a bilayered chiral structure. *Physical Review Letters*, 97(17):177401, 2006.

[143] N. K. Grady, J. E. Heyes, D. R. Chowdhury, Y. Zeng, M. T. Reiten, A. K. Azad, A. J. Taylor, D. A. R. Dalvit, and H. Chen. Terahertz metamaterials for linear polarization conversion and anomalous refraction. *Science*, 340 (6138):1304–1307, 2013.

[144] N. Yu, F. Aieta, P. Genevet, M. A. Kats, Z. Gaburro, and F. Capasso. A broadband, background-free quarter-wave plate based on plasmonic metasurfaces. *Nano Letters*, 12(12):6328–6333, 2012.

[145] S. Ahn, K. Lee, J. Kim, S. Kim, J. Park, S. Lee, and P. Yoon. Fabrication of a 50 nm half-pitch wire grid polarizer using nanoimprint lithography. *Nanotechnology*, 16(9):1874, 2005.

[146] S. Fan and J. D. Joannopoulos. Analysis of guided resonances in photonic crystal slabs. *Physical Review B*, 65(23):235112, 2002.

[147] M. Deubel, G. Von Freymann, M. Wegener, S. Pereira, K. Busch, and C. M. Soukoulis. Direct laser writing of three-dimensional photonic-crystal templates for telecommunications. *Nature Materials*, 3(7):444–447, 2004.

[148] H. Altug and J. Vuckovic. Polarization control and sensing with two-dimensional coupled photonic crystal microcavity arrays. *Optics Letters*, 30(9):982–984, 2005.

[149] D. Xiao, K. W. Kim, and J. M. Zavada. Imaging properties of a metallic photonic crystal. *Journal of Applied Physics*, 101(11):113105, 2007.

[150] X. Hu, P. Jiang, C. Ding, H. Yang, and Q. Gong. Picosecond and low-power all-optical switching based on an organic photonic-bandgap microcavity. *Nature Photonics*, 2(3):185–189, 2008.

[151] M. Boroditsky, R. Vrijen, T. F. Krauss, R. Coccioli, R. Bhat, and E. Yablonovitch. Spontaneous emission extraction and purcell enhancement from thin-film 2-d photonic crystals. *Journal of Lightwave Technology*, 17 (11):2096–2112, 1999.

[152] A. A. Erchak, D. J. Ripin, S. Fan, P. Rakich, J. D. Joannopoulos, E. P. Ippen, G. S. Petrich, and L. A. Kolodziejski. Enhanced coupling to vertical radiation using a two-dimensional photonic crystal in a semiconductor light-emitting diode. *Applied Physics Letters*, 78(5):563–565, 2001.

[153] M. Meier, A. Mekis, A. Dodabalapur, A. Timko, R. E. Slusher, J. D. Joannopoulos, and O. Nalamasu. Laser action from two-dimensional distributed feedback in photonic crystals. *Applied Physics Letters*, 74(1): 7–9, 1999.

[154] M. Yokoyama and S. Noda. Finite-difference time-domain simulation of two-dimensional photonic crystal surface-emitting laser. *Optics Express*, 13(8): 2869–2880, 2005.

[155] A. Mekis, A. Dodabalapur, R. E. Slusher, and J. D. Joannopoulos. Two-dimensional photonic crystal couplers for unidirectional light output. *Optics Letters*, 25(13):942–944, 2000.

[156] K. J. Lee, R. LaComb, B. Britton, M. Shokooh-Saremi, H. Silva, E. Donkor, Y. Ding, and R. Magnusson. Silicon-layer guided-mode resonance polarizer with 40-nm bandwidth. *Photonics Technology Letters, IEEE*, 20(22):1857–1859, 2008.

[157] V. Lousse, W. Suh, O. Kilic, S. Kim, O. Solgaard, and S. Fan. Angular and polarization properties of a photonic crystal slab mirror. *Optics Express*, 12 (8):1575–1582, 2004.

[158] S. Boutami, B. B. Bakir, H. Hattori, X. Letartre, J. Leclercq, P. Rojo-Romeo, M. Garrigues, C. Seassal, and P. Viktorovitch. Broadband and compact 2-d photonic crystal reflectors with controllable polarization dependence. *Photonics Technology Letters, IEEE*, 18(7):835–837, 2006.

[159] A. S. Chadha, D. Zhao, S. Chuwongin, Z. Ma, and W. Zhou. Polarization- and angle-dependent characteristics in two dimensional photonic crystal membrane reflectors. *Applied Physics Letters*, 103(21):211107, 2013.

[160] R. C. Jones and P. S. Eng. The wire grid as a near-infrared polarizer. *Journal of the Optical Society of America*, 50, 1960.

[161] J. P. Auton. Infrared transmission polarizers by photolithography. *Applied Optics*, 6(6):1023–1027, 1967.

[162] Thorlabs holographic wire grid polarizers.

[163] I. Yamada, N. Yamashita, T. Einishi, M. Saito, K. Fukumi, and J. Nishii. Modeling and imprint fabrication of an infrared wire-grid polarizer with an antireflection grating structure. *Infrared Physics & Technology*, 64:13–17, 2014.

[164] K. Shiraishi and H. Yoda. Infrared polarizer employing multiple metal-film subwavelength gratings. *Optics Express*, 21(12):13998–14007, 2013.

[165] I. Yamada, K. Fukumi, J. Nishii, and M. Saito. Near-infrared polarizer with tungsten silicide wire grids. *Japanese Journal of Applied Physics*, 50(1R): 012502, 2011.

[166] K. Shiraishi, S. Oyama, and C. S. Tsai. A polarizer using thin metallic-film subwavelength grating for infrared to terahertz region. *Journal of Lightwave Technology*, 29(5):670–676, 2011.

[167] K. J. Lee, J. Giese, L. Ajayi, R. Magnusson, and E. Johnson. Resonant grating polarizers made with silicon nitride, titanium dioxide, and silicon: Design, fabrication, and characterization. *Optics Express*, 22(8):9271–9281, 2014.

[168] J. Ma, F. Zhu, and C. Zhou. Wideband polarizer in the middle ir wavelength region based on guided mode resonance effect. *Photonics Technology Letters, IEEE*, 26(13):1364–1367, 2014.

[169] W. H. Lim, Y. K. Yap, W. Y. Chong, C. H. Pua, N. M. Huang, R. M. De La Rue, and H. Ahmad. Graphene oxide-based waveguide polariser: From thin film to quasi-bulk. *Optics Express*, 22(9):11090–11098, 2014.

[170] B. Shen, P. Wang, R. Polson, and R. Menon. Ultra-high-efficiency metamaterial polarizer. *Optica*, 1(5):356–360, 2014.

[171] X. Guan, P. Chen, S. Chen, P. Xu, Y. Shi, and D. Dai. Low-loss ultracompact transverse-magnetic-pass polarizer with a silicon subwavelength grating waveguide. *Optics Letters*, 39(15):4514–4517, 2014.

[172] B. Lin, H.and Jia and M. Gu. Dynamic generation of debye diffraction-limited multifocal arrays for direct laser printing nanofabrication. *Optics Letters*, 36(3):406–408, 2011.

[173] V. P. Gusynin, S. G. Sharapov, and J. P. Carbotte. Magneto-optical conductivity in graphene. *Journal of Physics: Condensed Matter*, 19(2): 026222, 2007.

[174] R. Kronig. On the theory of dispersion of x-rays. *Journal Optical Society America*, 12(6):547–556, 1926.

[175] Y. Zhang, L. Guo, H. Xia, Q. Chen, J. Feng, and H. Sun. Photoreduction of graphene oxides: methods, properties, and applications. *Advanced Optical Materials*, 2(1):10–28, 2014.

[176] J. Tauc, R. Grigorovici, and A. Vancu. Optical properties and electronic structure of amorphous germanium. *Physica Status Solidi (b)*, 15(2):627–637, 1966.

[177] S. Maeda, G. Thyagarajan, and P. N. Schatz. Absolute infrared intensity measurements in thin films. ii. solids deposited on halide plates. *The Journal of Chemical Physics*, 39(12):3474–3481, 1963.

[178] O. S. Heavens. *Optical properties of thin solid films*. Courier Corporation, 1991.

[179] F. Bonaccorso, Z. Sun, T. Hasan, and A. C. Ferrari. Graphene photonics and optoelectronics. *Nature Photonics*, 4(9):611–622, 2010.

[180] M. Hirata, T. Gotou, S. Horiuchi, M. Fujiwara, and M. Ohba. Thin-film particles of graphite oxide 1:: High-yield synthesis and flexibility of the particles. *Carbon*, 42(14):2929–2937, 2004.

[181] T. Gu, N. Petrone, J. F. McMillan, A. van der Zande, M. Yu, G. Lo, D. Kwong, J. Hone, and C. W. Wong. Regenerative oscillation and four-wave mixing in graphene optoelectronics. *Nature Photonics*, 6(8):554–559, 2012.

[182] R Dror, Z Burshtein, M Pokrass, and R Gvishi. Transition from saturable to reverse saturable absorption in multi-walled carbon nanotube-doped sol-gel hybrid glasses. *JOSA B*, 32(10):2198–2206, 2015.

[183] R. Trusovas, K. Ratautas, G. Račiukaitis, J. Barkauskas, I. Stankevičienė, G. Niaura, and R. Mažeikienė. Reduction of graphite oxide to graphene with laser irradiation. *Carbon*, 52:574–582, 2013.

[184] G. X. Chen, M. H. Hong, T. C. Chong, H. I. Elim, G. H. Ma, and W. Ji. Preparation of carbon nanoparticles with strong optical limiting properties by laser ablation in water. *Journal of Applied Physics*, 95(3):1455–1459, 2004.

[185] H. Zhang, S. Virally, Q. Bao, L. Kian Ping, S. Massar, N. Godbout, and P. Kockaert. Z-scan measurement of the nonlinear refractive index of graphene. *Optics Letters*, 37(11):1856–1858, 2012.

[186] E. Hendry, P. J. Hale, J. Moger, A. K. Savchenko, and S. A. Mikhailov. Coherent nonlinear optical response of graphene. *Physical Review Letters*, 105(9):097401, 2010.

[187] J. Matres, G. C. Ballesteros, P. Gautier, J. M. Fédéli, J. Martí, and C. J. Oton. High nonlinear figure-of-merit amorphous silicon waveguides. *Optics Express*, 21(4):3932–3940, 2013.

[188] J. Paredes, S. Villar-Rodil, A. Martinez-Alonso, and J. M. D. Tascon. Graphene oxide dispersions in organic solvents. *Langmuir*, 24(19):10560–10564, 2008.

[189] C. Zhu, S. Guo, Y. Fang, and S. Dong. Reducing sugar: new functional molecules for the green synthesis of graphene nanosheets. *ACS Nano*, 4(4): 2429–2437, 2010.

[190] V. Abdelsayed, S. Moussa, H. M. Hassan, H. S. Aluri, M. M. Collinson, and M. S. El-Shall. Photothermal deoxygenation of graphite oxide with laser excitation in solution and graphene-aided increase in water temperature. *The Journal of Physical Chemistry Letters*, 1(19):2804–2809, 2010.

[191] M. Acik, G. Lee, C. Mattevi, M. Chhowalla, K. Cho, and Y. J. Chabal. Unusual infrared-absorption mechanism in thermally reduced graphene oxide. *Nature Materials*, 9(10):840–845, 2010.

[192] L. Huang, Y. Liu, L. Ji, Y. Xie, T. Wang, and W. Shi. Pulsed laser assisted reduction of graphene oxide. *Carbon*, 49(7):2431–2436, 2011.

[193] A. R. Sadrolhosseini, A. S. M. Noor, N. Faraji, A. Kharazmi, and M. A. Mahdi. Optical nonlinear refractive index of laser-ablated gold nanoparticles graphene oxide composite. *Journal of Nanomaterials*, 962917, 2014.

[194] Y. Xu, Z. Liu, X. Zhang, Y. Wang, J. Tian, Y. Huang, Y. Ma, X. Zhang, and Y. Chen. A graphene hybrid material covalently functionalized with porphyrin: synthesis and optical limiting property. *Advanced Materials*, 21 (12):1275–1279, 2009.

[195] J. Balapanuru, J. Yang, S. Xiao, Q. Bao, M. Jahan, L. Polavarapu, J. Wei, Q. Xu, and K. P. Loh. A graphene oxide–organic dye ionic complex with dna-sensing and optical-limiting properties. *Angewandte Chemie*, 122(37): 6699–6703, 2010.

[196] M. Liu, R. Zhang, and W. Chen. Graphene-supported nanoelectrocatalysts for fuel cells: synthesis, properties, and applications. *Chemical Reviews*, 114 (10):5117–5160, 2014.

[197] A. Cao, Z. Liu, S. Chu, M. Wu, Z. Ye, Z. Cai, Y. Chang, S. Wang, Q. Gong, and Y. Liu. A facile one-step method to produce graphene–cds quantum dot nanocomposites as promising optoelectronic materials. *Advanced Materials*, 22(1):103–106, 2010.

[198] T. Chen, I. Chang, M. Yang, H. Chiu, and C. Lee. The exceptional photocatalytic activity of zno/rgo composite via metal and oxygen vacancies. *Applied Catalysis B: Environmental*, 142:442–449, 2013.

[199] Y. Liang, Y. Li, H. Wang, J. Zhou, J. Wang, T. Regier, and H. Dai. Co3o4 nanocrystals on graphene as a synergistic catalyst for oxygen reduction reaction. *Nature Materials*, 10(10):780–786, 2011.

[200] X. Zheng, B. Jia, X. Chen, and M. Gu. In situ third-order non-linear responses during laser reduction of graphene oxide thin films towards on-chip non-linear photonic devices. *Advanced Materials*, 26(17):2699–2703, 2014.

[201] L. Qiu, J. Z. Liu, S. L. Y. Chang, Y. Wu, and D. Li. Biomimetic superelastic graphene-based cellular monoliths. *Nature Communications*, 3:1241, 2012.

[202] J. Kirz. Phase zone plates for x rays and the extreme uv. *Journal Optical Society America*, 64(3):301–309, 1974.

[203] M. Gu. *Advanced optical imaging theory*, volume 75. Springer Science & Business Media, 2000.

[204] J. W. Goodman. *Introduction to Fourier optics*. Roberts and Company Publishers, 2005.

[205] Y. Tao, B. Varghese, M. Jaiswal, S. Wang, Z. Zhang, B. Oezyilmaz, K. P. Loh, E. S. Tok, and C. H. Sow. Localized insulator-conductor transformation of graphene oxide thin films via focused laser beam irradiation. *Applied Physics A*, 106(3):523–531, 2012.

[206] X. Li, Q. Zhang, X. Chen, and M. Gu. Giant refractive-index modulation by two-photon reduction of fluorescent graphene oxides for multimode optical recording. *Scientific Reports*, 3, 2013.

[207] X. Li, H. Ren, X. Chen, J. Liu, Q. Li, C. Li, G. Xue, J. Jia, L. Cao, A. Sahu, and M. Gu. Athermally photoreduced graphene oxides for three-dimensional holographic images. *Nature Communications*, 6, 2015.

[208] N. Yu and F. Capasso. Flat optics with designer metasurfaces. *Nature Materials*, 13(2):139–150, 2014.

[209] M. Fernández-Suárez and A. Y. Ting. Fluorescent probes for super-resolution imaging in living cells. *Nature Reviews Molecular Cell Biology*, 9 (12):929–943, 2008.

[210] W. Zhou, Z. Ma, H. Yang, Z. Qiang, G. Qin, H. Pang, L. Chen, W. Yang, S. Chuwongin, and D. Zhao. Flexible photonic-crystal fano filters based on transferred semiconductor nanomembranes. *Journal of Physics D: Applied Physics*, 42(23):234007, 2009.

[211] Qiaoliang Bao, Han Zhang, Bing Wang, Zhenhua Ni, Candy Haley Yi Xuan Lim, Yu Wang, Ding Yuan Tang, and Kian Ping Loh. Broadband graphene polarizer. *Nature Photonics*, 5(7):411–415, 2011.

Publications

Journal articles:

Published:

1. **X. Zheng**, H. Lin, T. Yang and B. Jia, “Laser trimming of graphene oxide for functional photonic applications”, ***Journal of Physics D: Applied Physics***, in press (2016).

2. **X. Zheng**, H. Lin and B. Jia, “Graphene oxide films, an emerging platform for ultrathin, light-weight, flexible photonic devices”, ***Australian Optical Society News***, **30**, 29 (2016).

3. **X. Zheng**$^{\#}$, B. Jia$^{\#}$, H. Lin, L. Qiu, D. Li and M. Gu, “Highly efficient and ultrabroadband graphene oxide ultrathin lenses with three-dimensional subwavelength focusing”, ***Nature Communications***, **6**, 8433 (2015). $^{\#}$Equal contribution

4. **X. Zheng**, B. Jia, X. Chen and M. Gu, “In Situ Third-Order Non-linear Responses During Laser Reduction of Graphene Oxide Thin Film Towards On-chip Non-linear Photonic Devices”, ***Advanced Materials***, **26**, 2699 (2014).

5. J. Ren$^{\#}$, **X. Zheng**$^{\#}$, Z. Tian, D. Li, P. Wang and B. Jia, “Giant third-order nonlinearity from low-loss electrochemical graphene oxide film with a high power stability”, ***Applied Physics Letters***, **109**, 221105 (2016). $^{\#}$Equal first author

6. S. Fraser#, **X. Zheng**#, L. Qiu, D. Li and B. Jia, "Enhanced optical nonlinearities of hybrid graphene oxide films embedded with gold nanoparticles", ***Applied Physics Letters***, **107**, 031112 (2015). #Equal first author

7. L. Chen, **X. Zheng**, Z. Du, B. Jia, M. Gu and M. Hong, "Frozen Matrix Hybrid Optical Nonlinear System Enhanced by Light Focusing Effect", ***Nanoscale***, **7**, 14982 (2015).

In submission:

1. **X. Zheng**, B. Xu and B. Jia, "Graphene oxide mid-infrared optics for high performance linear polarizers", **in submission**, (2016).

Conferences:

Post deadline papers:

1. **X. Zheng**, B. Jia, H. Lin, L. Qiu, D. Li and M. Gu, "Femtosecond laser fabricated ultra-flat lens in a graphene oxide thin film", *Frontiers in Optics*, Tucson, United States, Oct. 2014.

2. **X. Zheng**, B. Jia and M. Gu, "Giant optical nonlinear response of graphene oxide films", *Frontiers in Optics*, Florida, United States, Oct. 2013.

Oral presentations:

1. **X. Zheng**, B. Jia, H. Lin, L. Qiu, D. Li and M. Gu, "Graphene oxide thin film for photonic applications", *KOALA*, Auckland, New Zealand, Nov. 2015.

2. **X. Zheng**, B. Jia, H. Lin, L. Qiu, D. Li and M. Gu, "Flexible ultrathin flat lens in a graphene oxide thin film", *RPGR*, Lorne, Australia, Oct. 2015.

3. **X. Zheng**, B. Jia, H. Lin, L. Qiu, D. Li and M. Gu, "Three-dimensional light concentration with graphene oxide thin film", *AIP*, Canberra, Australia, Dec. 2014.

4. **X. Zheng**, B. Jia and M. Gu, "Photoreduction of graphene oxide towards photonic applications", *KOALA*, Adelaide, Australia, Nov. 2014.

5. **X. Zheng**, B. Jia, X. Chen and M. Gu, "Ellipsometry characterization of graphene oxide thin films through the laser-induced reduction process", *ANZCOP*, Perth, Australia, Dec. 2013.

6. **X. Zheng**, B. Jia and M. Gu, "Broadband optical nonlinear activities of graphene oxide films", *KOALA*, Sydney, Nov. 2013.

7. **X. Zheng**, B. Jia, X. Chen and M. Gu, "Giant optical nonlinear response of graphene oxide films", *7th VACPS*, Melbourne, Nov. 2013.

8. B. Jia, Y. Zhang, **X. Zheng** and M. Gu, "Graphene Oxide as Antireflection Coating for Silicon Solar Cells", *Light, Energy and the Environment*, Canberra, Australia, Dec. 2014.

9. B. Jia, B. Mashford, **X. Zheng** and M. Gu, "Nonlinear photonic crystal in quantum dot films", *ANZCOP*, Perth, Australia, Dec. 2013.

Posters:

1. **X. Zheng**, B. Jia and M. Gu, "Direct laser fabrication on graphene oxide thin films", *CUDOS Workshop*, Melbourne, Australia, Feb. 2014.

2. **X. Zheng**, B. Jia and M. Gu, "Graphene oxide: a platform towards tunable on-chip nonlinear phtonic devices", *CUDOS Board Meeting*, Sydney, Oct. 2013.

3. **X. Zheng**, B. Jia and M. Gu, "Third-order nonlinearity measurements of the graphene-doped polymer", *CUDOS Workshop*, Melbourne, Feb. 2012.